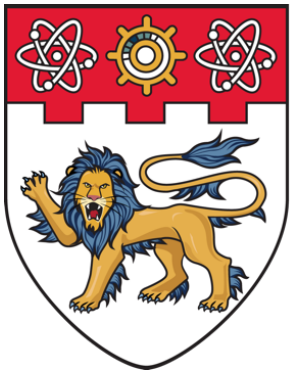

NANYANG TECHNOLOGICAL UNIVERSITY
SINGAPORE

LASER INSCRIBED OPTICAL WAVEGUIDES IN EMERGING PHOTONIC MATERIAL PLATFORMS

MARÍA RAMOS VÁZQUEZ

Interdisciplinary Graduate School

2019

LASER INSCRIBED OPTICAL WAVEGUIDES IN EMERGING PHOTONIC MATERIAL PLATFORMS

MARÍA RAMOS VÁZQUEZ

INTERDISCIPLINARY GRADUATE SCHOOL

A thesis submitted to the Nanyang Technological University
in partial fulfilment of the requirement for the degree of
Doctor of Philosophy

2019

Statement of Originality

I hereby certify that the work embodied in this thesis is the result of original research and has not been submitted for a higher degree to any other University or Institution.

23/01/2019 

Date María Ramos Vázquez

Supervisor Declaration Statement

I have reviewed the content and presentation style of this thesis and declare it is free of plagiarism and of sufficient grammatical clarity to be examined. To the best of my knowledge, the research and writing are those of the candidate except as acknowledged in the Author Attribution Statement. I confirm that the investigations were conducted in accord with the ethics policies and integrity standards of Nanyang Technological University and that the research data are presented honestly and without prejudice.

24/01/2019

Date

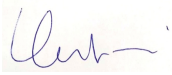

Cesare Soci

Authorship Attribution Statement

This thesis contains material from 2 papers published in the following peer-reviewed journals where I was the first and/or corresponding author.

Section 4.4, from chapter 4, is published as M. R. Vázquez, V. Bharadwaj, B. Sotillo, S. Z. A. Lo, R. Ramponi, N. I. Zheludev, G. Lanzani, S. M. Eaton, and C. Soci, "Optical NP problem solver on laser-written waveguide platform," *Optics Express*, **26** (2), p. 702, 2018. DOI: 10.1364/OE.26.000702.

The contributions of the co-authors are as follows:

- Prof. Soci provided the initial projection direction.
- I prepared the manuscript drafts. The manuscript was revised by Prof. Soci and Dr. Eaton.
- Dr. Eaton and I worked on the design of the oracle chip.
- V. Bharadwaj carried out the fabrication of the oracle chip in the FemtoFab lab, at Istituto Italiano di Tecnologia, Milano.
- Dr. Sotillo was in charge of characterizing the oracle chip.
- I performed all the laboratory work to solve the oracle chip in the School of Physical and Mathematical Sciences, Nanyang Technological University, Singapore. I also analyzed the data.
- Dr. Lo helped with the LabVIEW software used to collect the data.
- Prof. Ramponi supported the project, together with Prof. N. I. Zheludev and Prof. Lanzani.

The first part of chapter 5 is published as M. R. Vázquez, B. Sotillo, S. Rampini, V. Bharadwaj, B.Gholipour, P. Fernández, R. Ramponi, C. Soci, and S. M. Eaton, "Femtosecond laser inscription

of nonlinear photonic circuits in Gallium Lanthanum Sulphide glass," *Journal of Physics Photonics*, **1**, p. 015006, 2018. DOI: 10.1088/2515-7647/aade60.

The contributions of the co-authors are as follows:

- Dr. Eaton and Prof. Soci suggested the work.
- I wrote the drafts of the manuscript together with V. Bharadwaj, Dr. Rampini, Dr. Sotillo and Dr. Gholipour. The manuscript was revised by Dr. Eaton and Prof. Soci.
- Dr. Gholipour performed the material synthesis at the Optoelectronics Research Centre, Southampton.
- Dr. Rampini, V. Bharadwaj, Dr. Sotillo and I performed some of the waveguide fabrications in different samples.
- Dr. Rampini, V. Bharadwaj, Dr. Sotillo and I carried out different characterizations of the chips.
- I performed the nonlinear characterization of the laser-inscribed waveguides in gallium lanthanum sulfide as ultrafast nonlinear optical switches and conducted the data analysis for the estimation of the nonlinear refractive index of the photonic structures.
- Dr. Sotillo conducted the μ-Raman and energy-dispersive X-ray characterization of the laser inscribed waveguides and analyzed the pertinent data.

23/01/2019

Date María Ramos Vázquez

Abstract

Indisputably, software run in conventional Von-Neumann architectures has provided solutions to most of the needs met until now. However, an efficient solving method for the solution of hard computational problems remains still a challenge due to the large amount of power and execution times required. In this context, alternative solutions to brute force electronic computing are incessantly searched. The integration of photonic hardware as a replacement of some small blocks of the main software could speed up execution times, providing faster solutions to non-polynomial complete problems, cognitive systems or quantum computations.

The thesis titled "laser inscribed optical waveguides in emerging photonic material platforms" portrays the potential of the ultrafast laser writing technique employed on three different materials for the fabrication of optical waveguides as the main building block of advanced optical circuits. The optical waveguides have been explored as a photonic element for future applications in cognitive and quantum computing systems.

An alumino-borosilicate glass (Corning EAGLE2000) has enabled low-loss optical waveguides at the convenient wavelength of 800 nm, offering solutions to optical circuits compatible with current Ti:Sapphire technologies and spontaneous-parametric down conversion sources. The well-known travelling salesman problem has been laser inscribed into one of the glass substrates and its solution has been optically found. This has been the first realization of a photonic "oracle" fabricated via femtosecond laser machining of waveguides, providing an enhanced integration by reduction of the physical problem size and, thus, allowing faster execution times compared to other optical approaches developed in fibers.

The second material of interest is gallium lanthanum sulfide glass, a chalcogenide which is useful for its non-volatile phase change transitions and highly nonlinear characteristics. An optimum processing window for low-loss single mode waveguides, operating at 800 nm wavelength has been reported for the first time by using a multiscan writing approach, opening the path towards integration of nonlinear optical circuits compatible with Ti:Sapphire technologies. The high Kerr nonlinearity displayed in the glass has been exploited to characterize laser inscribed optical direc-

tional couplers acting as ultrafast all-optical switches and an estimation of the nonlinear refractive index of the laser inscribed waveguides has been reported. As a feasible application, gallium lanthanum sulfide waveguides have been explored as an integrated neuromorphic photonic platform, which includes a series of neural biological features.

Diamond has been the third material used due to its capability of hosting nitrogen-vacancy (NV) color centers, whose long spin coherence times at room temperature are promising for applications in quantum information and magnetic sensing. Here, femtosecond laser writing has provided integration of optical waveguides aligned with the NV color centers within the bulk of diamond with a submicrometer resolution, allowing efficient optical excitation and collection of the luminescence signal of these defects. In future, such a platform could be applied to quantum sensing devices with record high sensitivity of electric fields, and quantum information systems.

Overall, this work shows the potential of ultrafast laser writing as a flexible fabrication tool for the implementation of cognitive and quantum computational problems into compact and scalable chips which are desirable for the study of new optical computing schemes and algorithm optimization.

Acknowledgements

In first place, I would like to thank my supervisors Prof. Cesare Soci and Dr. Shane M. Eaton for giving me the opportunity to be part of their research groups. Working in Shane's group would not have been possible without the help of Prof. Lazani, who made this research collaboration possible. I also want to thank Prof. Roberta Ramponi for her warm welcome when I first arrived to Politecnico di Milano.

My formation as a researcher has been strongly influenced by my collaborators at the Politecnico di Milano, Dr. Shane M. Eaton, Dr. Belén Sotillo and Dr. Vibhav Bharadwaj, who have always been very supportive with me. I am very grateful to have worked with such enthusiastic people and I must thank them for teaching me all about fabrication and characterization of waveguides. Thank you not only for being a great research team, but for being a role model for me. I also need to thank Shane and Vibhav for coming to work to Singapore as a collaboration of the oracle project.

My thanks to Dr. Su-Zee A. Lo, who believed in my skills as a researcher when I was struggling with some experiments and who introduced me to the amazing world of LabVIEW, making my life so much easier.

Thank you to Dr. Franco Valduga and Prof. Giulio Cerullo for letting me work in the ultrafast lab, where I carried out the experiments related to optical switching in chalcogenide waveguides.

I want to express my gratitude to Edoardo Vicentini for assisting me in the lab whenever I needed to use a new device. He has also given an unconditional support during my thesis writing time.

My appreciation to Andrea and Ellen from the IGS team for their excellent guidance and helfpul assistance during the last four years.

Out of the lab, many people had still the power to encourage me in my research by having a positive attitude in life. I must thank Seetanshu Junnarkar for accompanying me since the first week of our PhDs and being a supportive friend. Thanks to the new people that came to the lab during the last months of my PhD, Pietro, Manu, Qi Ying and Davide for making of my PhD thesis writing an enjoyable journey.

Finally, this thesis is dedicated to my parents, María Ángeles and Robert, and my sisters, Virginia and Carmen, for encouraging me every day during these four years.

Contents

List of Figures

List of Tables

Abbreviations

- AR: Antireflection coating
- BBO: Beat Barium Borate
- CCD: Charge-coupled device
- CMOS: Complementary metal-oxyde semiconductor
- CW: Continuous wave
- DFB: Distributed feedback
- DI: De-ionized
- EDX: Energy-dispersive X-Ray
- EPSP: Excitatoy post-synaptic potential
- FOM: Figure of merit
- FWHM: Full width at half maximum
- GLS: Gallium lanthanum sulfide
- HPHT: High pressure high temperature
- IPSP: Inhibitory post-synaptic potential
- NA: Numerical aperture
- NV: Nitrogen-vacancy

- ND: Neutral density
- NP: Non-polinomial
- PL: Photoluminescence
- SHG: Second harmonic generation
- SNR: Signal-to-noise ratio
- SPDC: Spontaneous parametric down-conversion
- SPM: Self-phase modulation
- STDP: Spike-timing-dependent plasticity
- TE: Transverse electric
- TM: Transverse magnetic
- THG: Third harmonic generation
- TPA: Two-photon absorption
- ZPL: Zero phonon line

Chapter 1

Introduction and motivations

This chapter addresses the main objectives of the research carried out in this thesis with a justification for the choice of the fabrication methods. A state of the art in femtosecond laser writing including some of the main achievements provided by this technique is also given.

New emerging photonic platforms are in the spotlight of a main scientific research which is in pursuit of fabrication techniques that allow rapid prototyping and compatibility with a diversity of materials. Femtosecond laser micromachining is a good candidate, as it is a direct method for the integration of optical circuits in a wide range of transparent materials. Beyond this requirement, there exists the need to develop optical circuits capable of generating solutions to factorial problems with more optimal speeds than those offered by conventional electronic computers, as well as the need to design nonlinear optical circuits providing ultrafast all-optical switching or to develop photonic quantum systems operating at ambient temperatures. The main objective of the thesis is to explore solutions towards all the open questions mentioned here by using ultrafast laser writing technique.

Direct laser inscription of optical circuits contained in substrates with suitable properties could offer solutions to the needs mentioned here. The implementation of laser inscribed photonic hardware in combination with conventional software could speed up computation times by exploit-

ing the benefits of laser parallel processing and the speed of light in linear and nonlinear optical regimes [7]. Regarding the quantum regime, laser inscription of optical circuits presenting controllable quantum properties at room temperatures would provide solutions to the problems faced by conventional ultra-cold atoms and trapped-ion systems [8, 9].

This thesis focuses on the basis of all these needs, which is the fabrication of optical waveguides as the main building block of more advanced optical circuits for applications in linear, nonlinear and quantum photonics. Depending on the purpose, a suitable selection of substrates for being processed under laser writing becomes essential. The development of low-loss photonic circuits working within the linear regime, supporting single mode guiding at wavelengths compatible with usual ultrafast Ti:Sapphire technologies and spontaneous parametric down conversion (SPDC) light sources would be beneficial. The search for an optimum processing window would enable the integration of compact laser-inscribed cascaded networks in common linear glasses for the solution of factorial problems, such as the so-called travelling salesman problem, which are computationally hard to solve.

Also, ultrafast laser inscription of waveguides in exotic nonlinear glasses, such as chalcogenides, would provide ultrafast all-optical switching circuits with time responses within the femtosecond range and photonic circuits with optically induced phase-change transitions, fiding application in non-volatile optical memories [10, 11]. The fabrication of single mode waveguides at near infrared wavelengths would be beneficial due to their compatibility with usual Ti:Sapphire lasers and SPDC sources.

On the other hand, it has been demonstrated that nitrogen-vacany (NV) defects hosted in diamond crystals are single photon emitters with optically manipulable spin properties and long coherence times at room temperature, with values similar to that of trapped ions [12]. Laser writing of optical waveguides in diamond substrates containing intrinsic NVs could offer solutions to conventional techniques where temperatures close to 0K and ultra high vacuum environments are needed. The combination of optical waveguides and NV centers in diamond substrates could also provide efficient manners to optically excite and collect the luminescence coming from these NV centers.

The selection of the substrates in the thesis is intended for different purposes. As a common linear glass for creating cascaded networks, Corning EAGLE2000 aluminum-borosilicate glass has been selected. For the inscription of nonlinear optical circuits, gallium lanthanum sulfide glass has been chosen. The type of diamond substrate selected for laser writing of waveguides has been grown through a process of high pressure high temperature (HPHT) which leads to the formation of a crystal with a large density of intrinsic nitrogen impurities (100 parts per million).

The use of femtosecond laser writing is mainly intended for ablation of material surfaces and to induce permanent modifications within the bulk of transparent materials. The first proof of femtosecond laser writing was reported in 1994 by Du *et al.* [13], where surface ablation of fused silica was demonstrated by using a femtosecond laser. Later in 1996, Davis *et al.* [14] proved permanent refractive index modifications by tightly focusing femtosecond laser pulses within the bulk of a transparent glass.

Femtosecond laser micromachining is based on laser-induced optical breakdown, entailing nonlinear absorption of the laser energy via electron ionizations confined within the focal volume and a posterior energy transfer to the lattice. For optical breakdown to occur, the peak intensities of the femtosecond laser pulses within the focal volume must reach values on the order of tens of TW/cm^2 in transparent materials [6]. The footprint left in the laser-irradiated volume undergoes a structural modification that results in a localized permanent change of the material, such as removal of the material at its surface, a change of the material's refractive index, or even the formation of a void, depending on the laser processing parameters. This confined modification, together with the translation of the substrate, makes possible laser machining with three spatial degrees of freedom which enables complex layering of structural modifications in three dimensions [15].

The advantages of employing femtosecond laser writing for the fabrication of photonic devices compared to other manufacturing methods are many. Some of the main benefits of using this technique are listed below:

- Simple and direct prototyping, avoiding the use of any fabrication mask or post-fabrication processing unlike lithographic methods. The technique offers a rapid and practical way of manufacturing devices by modifying the algorithm that controls the movement of the

computer-controlled translational stages where the substrates are placed.

- Three-dimensional layering of laser writing structures due to the possibility of combining the traslation of the substrate in the three spatial dimensions and the confinement of the laser beam within the focal volume. In a different approach, it is also possible to keep the substrate fixed and proceed with a laser-beam scanning by translating the laser focal volume with galvo scanners.

- The technique offers versatility with applications in a broad range of materials. Femtosecond laser writing can be employed in a variety of materials such as glasses, crystals, ceramics and polymers.

- A broad range of fabrication modalities is available depending on the laser processing parameters employed. Femtosecond laser inscription provides surface ablation of materials by translating the focal volume along the sample surface enabling the fabrication of ablated microfluidic channels [16]. The technique also allows bulk optical waveguiding when the scanning of the laser focal volume is performed below the sample surface [14]. The application of chemical etching after the bulk modification leads also to the formation of buried microfluidic channels [17]. Two-photon polymerization is also employed for the formation of three-dimensional microstructures in photoresists [18].

The advantages mentioned above have been exploited to laser write a variety of different active and passive devices for the last twenty years, offering photonic solutions with major scientific rigor.

The transparent materials used in laser processing for the formation of optical waveguides can be glasses, crystals, ceramics and polymers. Glasses and crystals present a large transparent window and a high purity, while polymer processing presents peak intensity thresholds for optical breakdown of at least one order of magnitude lower than in glass. Despite having lower peak intensity thresholds, polymers present larger transmission losses compared with glasses and crystals, being this the main reason why not many fabrications have been performed in this type of substrates [1].

Passive waveguides have been laser-written in a wide variety of common linear glasses, con-

stituting the main building block of optical circuits enabling signal transmission lines and optical power splitting [14, 19, 20]. The change in the geometry of the waveguides has led to many different waveguide configurations such as Y-junctions and 1-to-N power splitters [21–25], 2×2 directional couplers [26–31], 3×3 directional couplers [32], Bragg grating waveguides [33], wavelength multiplexers [30], ring resonators [34] and Mach-Zehnder interferometers [35] in a variety of transparent materials. Propagation losses below 1 dB/cm are typically achieved for waveguides formed in common linear glasses [19, 36–41]. Bending waveguide radii with minimum values of 10 mm have been also reported [41].

Femtosecond laser inscribed emerging platforms in linear glasses have been employed for the solution of complex computational problems, such as factoring, in both classical [42] and quantum regimes [43–45]. Photonic boson sampling in laser-inscribed photonic circuits allows to infer the evolution of bosons across the photonic network undergoing linear unitary transformations, allowing a precise control of multiphoton interference. Though still far from feasible physical implementations, photonic boson sampling in these lab-on-chip devices provides a very important and intermediate experimental milestone in the development of large-scale quantum computers and interferometers [43–45]. Also, fs laser-written directional couplers are a potential technology for the realization of quantum optical gates due to their ability of acting as polarization-encoded qubits [46].

Of particular interest during the last decade has been the development of optical circuits hosted in nonlinear optical glasses, such as chalcogenides, due to their interesting characteristics for opto-electronic purposes [47–51]. For instance, chalcogenides have a high linear and nonlinear refractive indices, a transparency window from visible to infrared wavelengths in the spectrum, a relatively low maximum phonon energy and an ultrafast nonlinear response in time on the order of the femtosecond range [52].

Direct laser inscription in chalcogenides has enabled ultrafast all-optical switches due to an easily-induced nonlinear Kerr effect coming from a high third order nonlinear susceptibility in these substrates [53]. Also, super continuum generation and spectral broadening have been demonstrated in direct laser-written waveguides in chalcogenide glasses [54–56]. Because of the thermally induced phase transition between amorphous to crystalline states, and vice versa, in chalco-

genide thin films [10, 11, 57, 58], the integration of direct laser-written photonic circuits into these substrates entails potential emerging platforms as optical non-volatile phase-change memories for rewritable data storage [11].

In addition to glass substrates, crystalline materials have been selected for the development of laser-buried-micromachined waveguides. Crystalline substrates offer unique characteristics which are not exhibited in glasses, such as even order optical nonlinearities and birefringence. Up to date, a wide range of crystals has been used for the fabrication of direct laser-written waveguides, such as quartz [59], silicon [60], β barium borate (BBO) [61], lithium niobate [62–67] , or diamond [68, 69], among many others [70–72].

Direct laser inscription of pure crystalline waveguides has enabled a series of electrooptic modulators and frequency converters for the case of type II waveguide laser writing modality, consisting of two parallel laser-induced modification lines separated by a certain distance, since this configuration preserves the nonlinear optical properties of the pristine material [6]. Moreover, the frequency conversion displayed in fs laser-written waveguides coming from second and higher-order nonlinearities provides enhanced efficiencies compared to the bulk material [73]. On the other hand, type I waveguides in crystals present thermal instabilities [63], not being compatible for high power applications, and even deterioration over time at ambient temperatures [64].

Femtosecond laser micromachining has enabled the fabrication of waveguides displaying second harmonic generation (SHG) of light for a wavelength range between $\sim$400 nm - 790 nm [74–79]. One of the most well-studied crystaline substrates in direct laser writing of waveguides has been lithium niobate, which has provided SHG of a pump wavelength at 1064 nm in pulsed regime resulting in generation of green light with a conversion efficiency of 49% and a SHG peak power of 235 W [74]. Direct laser inscription of buried waveguides in nonlinear $KTiOPO_4$ crystal has enabled second harmonic generation (SHG) by birefringent phase-matching for a pump wavelength of 1064 nm with a conversion efficiency of 45.6% and SHG peak powers as high as 427 W [75].

Quasi-phase matched SHG of near-infrared light has been obtained in laser-written waveguides in periodically poled lithium niobate crystals for pump wavelengths of 1548 nm and 1549

nm resulting in SH conversion efficiencies of 34.8% and 18.2% in [76] and [77], respectively. A type III BBO laser-micromachined waveguide, known as depressed cladding waveguide and consisting of a core surrounded by several low-index tracks, has enabled SHG of a 1064-nm optical pump with a 25% conversion efficiency and 373 W of SH peak power [78]. Under continuous-wave pump at 980 nm, laser-written waveguides in periodically poled potassium titanyl phosphate (PPKTP) offered SHG down to 400 nm wavelength [79]. The high conversion efficiencies obtained from laser-inscribed waveguides in nonlinear crystals evince direct laser-written waveguides as potential integrated frequency converters.

Electrooptic modulators have also been inscribed in lithium niobate crystals, being capable of modulating the phase, amplitude or polarization of light [80–83]. The electrooptic modulators have been directly laser written in a type II waveguide-based platform with a Mach Zehnder interforemeter configuration.

Fabrication of active waveguides via femtosecond laser micromachining has also played an important role in the development of optical amplifiers [84–87], enabling low-noise and low-cost amplifiers, and waveguide lasers [72, 85, 86, 88, 89]. Interesting active ions, such as erbium, ytterbium, neodimium and bismuth, have been extensively studied and incorporated in dielectric glasses and crystals, since they offer ultra-broad gain bandwidth along the infrared spectrum [6]. Waveguide amplifiers operating in the whole C telecom band (1530 nm - 1565 nm) [85–87], tunable waveguide lasers in the C-band [86], multi-mode operation [85, 86, 88], single-mode operation, and passive mode-locking [90] in waveguide lasers have been demonstrated via the ultrafast laser inscription technique. Depending on the active ions and the mechanisms for lasing, femtosecond laser inscription of waveguides has provided miniaturized waveguide lasers with lasing wavelengths ranging from 530 nm to 2 μm [91–93].

Many fabrications have been done in laser-written waveguide amplifiers in Er:Yb-doped phosphate glasses [85, 86]. One of the first laser-written waveguide amplifiers was inscribed in Er:Yb-doped phosphate glass, showing a waveguide amplifier displaying a net gain over all the telecom C-band with a peak net gain of 7.3 dB located at 1535 nm [87]. Femtosecond laser writing has also enabled distributed feedback (DFB) lasers by directly laser writing a Bragg grating in the active medium and superimposing the Bragg grating to the laser-inscribed waveguide in a single-step

writing process [94]. Up to now, notable improvements in laser-micromachined waveguide lasers have been achieved, obtaining lasing slope efficiencies about 60% for the case of some active materials [95–97] and single-mode waveguide lasers after an optimization of the laser cavity [98].

Femtosecond laser-written waveguides in Er:Yb-doped phosphate glass present laser operation by means of butt-coupling two fiber Bragg gratings at the two ports of the waveguide exhibiting a high reflectivity at one side and a lower reflectivity at the other side, being used as the output of the laser cavity [85, 86, 88, 99]. Direct inscription of waveguides in Er:Yb-doped phosphate glass resulted in waveguide lasers with slope efficiencies between 38% and 42% and a net gain higher than 1 dB for wavelengths between 1525 nm and 1575 nm [99]. The maximum laser power emission was 112 mW for a total pump power of 470 mW at 976 nm and the laser bandwidth obtained was $\sim$0.5 nm. The incident pump power was 21.6 mW [99].

Green lasing wavelengths have been obtained in self-frequency-doubled laser-written waveguides in Nd:YAB [91] and Nd:YCOB [92] doped crystals. Laser emission at visible wavelengths has been obtained from femtosecond laser-written waveguides in praseodymium (Pr) doped materials with a maximum emitted power at red wavelengths of 28 mW with a slope efficiency of 8%. Laser written active waveguides in Ti:Sapphire have offered laser tunability ranging between 700 nm - 870 nm resulting in a maximum emitted power of 143 mW at 800 nm wavelength for a slope efficiency of 23.5% [100].

Actively doped yttrium aluminum garnet (YAG) ceramics and crystals have also attracted a lot of attention in the fabrication of laser-micromachined active waveguides [95, 101–104]. Under optical pump of 808 nm, direct type II laser-inscribed waveguides in Nd:YAG crystals show efficient laser generation at 1064 nm with a maximum output power of 1.29 W and a slope efficiency of 59% [96]. A 70% slope efficiency has been achieved in type II laser-inscribed waveguides in Nd:$GdVO_4$ [105]. Waveguides written in Yb:YAG crystals have shown a slope efficiency of 75% offering working wavelength at 1030 nm and showing its potential as efficient integrated laser sources [97].

Laser writing of waveguides in Pr^{3+}:Y_2SiO_5, a rare-earth doped crystal, implies an important feature in the development of spin-wave quantum memory devices through the storage of light

pulses in the ground and excited states of the praseodymium ions [106].

Moreover, magneto-optic switching through a laser inscribed waveguide in a doped Faraday glass has been demonstrated by measuring the phase shift in the polarization of light along the waveguide when an external magnetic field is applied [107].

Some photonic devices have been directly laser written in transparent polymers, for instance, polymethylmethacrylate has served as a hosting polymer for the laser inscription of passive waveguides offering single mode operation and power splitting [108].

Recently, femtosecond laser micromachining enabled the inscription of low-loss type II waveguides in diamond crystals [109], implying future emerging platforms for quantum information processing and magnetic and electric field sensing by exploiting the properties exhibited by nitrogen-vacancy (NV) color centers intrinsically hosted in the substrates [110, 111]. Moreover, femtosecond laser writing technique has demonstrated deterministic placing of NVs in the bulk of diamond substrates, which combined with direct laser writing of waveguides by means of a single-step writing process leads to integrated photonic platforms with efficient optical excitation and collection of NVs. Also, NVs formed by fs laser inscription technique have demonstrated their role as single photon emitters [112].

As a last example, systems of straight and curved femtosecond laser-written waveguide arrays represent a particular case of the so-called discrete optical systems [113]. Miniaturization of optical waveguide arrays offers crosstalk between the adjacent waveguiding structures, where the evolution of light propagation can be explained by coupled-mode theory [114]. Based on this theory, waveguide arrays become discrete systems where the electromagnetic field can be separated into different transverse modes for each waveguide and a longitudinal dependent amplitude. A periodic modulation of the refractive index at one, two or three transverse directions of the waveguides enables one-dimensional, two-dimensional or three-dimensional arrays, respectively, which produces symmetry breaking compared to homogeneous systems where all the dimensions are equal. Examples of discrete waveguide arrays have been used for the development of linear and nonlinear switchable topological photonic systems [113, 115].

Integrated circuits of laser-inscribed optical waveguides into compact chips may offer photonic solutions to different research fields. Parallel laser processing and speed of light can be exploited to efficiently solve the so-called factorial problems, which result computationally hard to solve. Also, nonlinear circuits offering optical switching within the femtosecond regime are very advantageous in this matter. Exploiting the photorefractivity offered by optical waveguides may be beneficial for the development of new photonic neuromorphic schemes that could be implemented as part of complete cognitive systems. In addition, laser-inscribed optical waveguides in crystals hosting point defects presenting controllable quantum properties at room temperatures could be convenient for the development of quantum and magnetic sensing devices, in comparison with other techniques.

In this thesis, the selection of the substrates is intended for different purposes in linear, nonlinear and quantum optics, in order to offer photonic solutions to the problems mentioned above. The main objective of the thesis is to investigate the optimum laser processing conditions for the inscription of low-loss optical waveguides in the suitable substrates. The selected materials are a linear Corning EAGLE2000 glass, nonlinear gallium lanthanum sulfide glass and diamond hosting a high density of nitrogen impurities (100 parts per million).

Application examples of the low-loss waveguides have been investigated in all the substrates. The linear waveguides written in Corning EAGLE2000 glass have been used for the optical solution of an encrypted network. The fabrication of waveguides in gallium lanthanum sulfide (GLS) glass, having a wide range of glass formation centered at 70:30 mol% Ga_2S_3 : mol% La_2S_3, aims to provide a processing window for optical circuits supporting single mode guiding at 800 nm, a convenient wavelength not reported until now in this material for their use with Ti:Sapphire lasers and spontaneous parametric down-conversion (SPDC) quantum sources. The nonlinear characterization of the photonic circuits inscribed in GLS glass as ultrafast all-optical switches has been performed. The photorefractivity in GLS waveguides has been also exploited in order to investigate the waveguides as a neuromorphic photonic system which mimicks the transmission of information across biological neurons. Optical waveguiding within the bulk of diamond has been also performed in order to offer solutions for an efficient optical excitation and collection of the photoluminescence displayed by NV centers embedded in the waveguides. Deterministic positioning of NV color centers by direct laser writing in diamond substrates has been also investigated.

A summary of the content of each chapter and the main findings of the thesis work are provided below.

In chapter 1, a rationale for the research goals is discussed. An overview of the femtosecond laser micromachining technique and the advantages offered over other fabrication methods is also included, followed by the state of the art in femtosecond laser writing of waveguides.

Chapter 2 includes the theoretical background related to ultrafast laser inscription in transparent materials. The laser-material interactions for the case of sub-picosecond laser pulses are reviewed, including the absorption processes and material relaxation and modifications. After the theory of fs pulse interaction in bulk transparent media, the theory of light propagation in waveguides, with solutions to Maxwell's equations for the case of hybrid modes in cylindrical step-index waveguides, is provided. After the theory of isolated guided modes, coupled mode theory is included, providing solutions for the case of two optical propagated modes that experience evanescent coupling along two parallel waveguides in proximity to one another.

Chapter 3 covers the experimental details employed in this thesis, including the laser machining system used for waveguide fabrications, the material properties of the selected substrates and the waveguide characterization methods. The end of the chapter also provides a detailed description of the autocorrelator used for the characterization of ultrashort pulses generated from a Ti:Sapphire oscillator.

In chapter 4, an elaboration of the first major set of results, obtained in Corning EAGLE2000 glass is given. An optimum processing window for the fabrication of low-loss waveguides, double S-bends and directional couplers is given. The application of these waveguides in a cascaded optical network modality is used for the solution of the well-known travelling salesman problem by interrogatin the network with ultrashort laser pulses. This demonstration might have implications in the study of new photonic architectures and algorithm optimization, being laser writing technique a flexible tool for the inscription of scalable mathematical problems into compact chips.

In chapter 5, an elaboration of the second major set of results, obtained in gallium lanthanum sulfide glass, is provided. An optimum laser processing window resulting in low-loss single-mode

waveguides at 800 nm wavelength is reported for the first time. The waveguides are characterized as ultrafast all-optical switches. In addition, the photorefractivity displayed in GLS glass is exploited in order to mimick a series of neural biological features in the laser-written waveguides. This last work has implications in the development of new neuromorphic devices.

In chapter 6, an elaboration of the third major set of results, obtained in diamond substrates, is provided. An optimum processing window for the fabrication of type II single-mode waveguides is discussed, followed by an investigation of the laser writing technique as a tool for a deterministic control of NV formation in the bulk diamond. The study of the photoluminescence signal generated along the laser-written diamond waveguides for their use in quantum and magnetic sensing is also provided.

Finally, the conclusion goes through a discussion of the key results obtained in the thesis and provides an outlook on future work and possible application directions.

Chapter 2

Theoretical background

The content of this chapter includes the theoretical background related to ultrafast laser inscribed waveguides. The beginning of the chapter deals with the theory of laser-material interactions for the case of sub-picosecond pulses, covering the main absorption processes of ultrashort pulses in transparent materials, followed by the relaxation and the type of laser-induced modification formed within the focal volume of the material. A brief explanation about the most common light propagation effects manifested when focusing light within the bulk of transparent materials carrying optical intensities above the threshold for optical breakdown is also provided. After the femtosecond pulse interaction within the bulk of a transparent media, the chapter provides the theory of light propagation in waveguides, solving the Maxwell's equations for the case of guided hybrid modes in cylindrical waveguides with symmetric transverse sections and presenting step-index profiles, as an approximation to the laser-inscribed waveguides shown in this thesis. The chapter ends with the coupled mode theory, applied to provide the solutions of two optical guided modes along two parallel waveguides being close enough to one another so that they exchange their optical energy through evanescent coupling.

2.1 Femtosecond laser pulse interaction within the bulk of transparent materials

In this section, a brief summary of the main physical mechanisms present during laser-material interactions of sub-picosecond pulses is given, including the different absorption processes that lead to the formation of an electron plasma within the focal volume of the material, followed by the material relaxation and the resulting type of permanent modification. After that, some of the light propagation effects manifested in both linear and nonlinear regimes when using intensities beyond the optical breakdown threshold of the materials are included.

2.1.1 Absorption mechanisms

Dielectrics and semiconductors cannot undergo linear absorption when focusing ultrashort optical pulses at visible or near-infrared wavelengths due to an energy gap (E_g) higher than the energy carried by a single photon ($h\nu < E_g$). However, when the focused optical peak intensities are on the order of 10 TW/cm^2, in the case of common glass [6], optical breakdown occurs and the simultaneous promotion of electrons from the valence band to the conduction band in periodic media takes place through nonlinear absorption processes in the material. Nonlinear absorption of sub-picosecond pulses in transparent materials is led by either multiphoton absorption, tunnelling ionization or a combination of these two processes.

Multiphoton absorption takes place when multiple photons carrying sufficient energy ($mh\nu > E_g$, where m is the number of photons) bridge the gap energy of the material and are simultaneously absorbed to the conduction band (as depicted in Fig. 2.1(a)). The multiphoton absorption rate is strongly dependent on the laser intensity by $\sigma_m I^m$, where σ_m is the cross section of the m-photon absorption process of a valence electron needed to be excited to the conduction band, I is the laser intensity and m is the minimum number of photons required to satisfy $mh\nu > E_g$ [116, 117]. Generally, multiphoton absorption is the leading nonlinear absorption process for low

laser intensities and high optical frequencies [6]. At higher laser intensities and lower optical frequencies, the strong electric field distorts the bands resulting in a reduction of the potential barrier between the valence and the conduction bands [116,117]. This distortion allows the valence electrons to directly undergo tunneling to the conduction band (as shown in Fig. 2.1(b)).

The Keldysh parameter provides information about the mechanism dominating the process of nonlinear absorption, depending on the material properties and the optical intensity and frequency [116, 117]:

$$\gamma = \frac{\omega}{e}\sqrt{\frac{m_e c n \varepsilon_0 E_g}{I}}, \tag{2.1}$$

where ω is the optical frequency, e is the fundamental electron charge, m_e is the effective electron mass, c is the speed of light, n is the linear refractive index of the material under laser irradiation, ε_0 is the permittivity in free space, E_g is the optical gap energy of the material and I is the laser intensity. For the case of $\gamma < 1.5$, tunneling ionization is the process dominating the nonlinear absorption. If $\gamma > 1.5$, multiphoton absorption leads the nonlinear promotion of valence electrons to the conduction band. If $\gamma \sim 1.5$, a combination of multiphoton absorption and tunneling ionization is responsible for the nonlinear absorption in the material.

Apart from multiphoton absorption and tunneling ionization, nonlinear absorptions are usually accompanied by avalanche ionizations. When a promoted electron through either multiphoton absorption or tunneling ionization occupies a place at the minimum energy level of the conduction band, this can linearly absorb several laser photons and being promoted to higher energy levels in the conduction band (this process is known as free carrier absorption) [118]. After sequential linear photon absorptions from an electron in the conduction band, this one will occupy an energy state in the conduction band that will exceed the conduction band minimum by more than the optical gap energy of the material. The hot electrons, with energies exceeding that of the optical gap, will cause an impact ionization, leading to the promotion of a valence electron to the minimum energy level of the conduction band and, thus, resulting in two electrons occupying the conduction band minimum (see Fig. 2.1(c)). These two excited electrons can further experience free carrier absorption and impact ionization over again, causing multiple avalanche ionizations that can last as long as the laser irradiation is present. The absorption rate of carriers through avalanche ionization is led by aIN, where a is the avalanche ionization coefficient, I is the optical intensity and N is the number of electrons absorbed via avalanche ionizations [116].

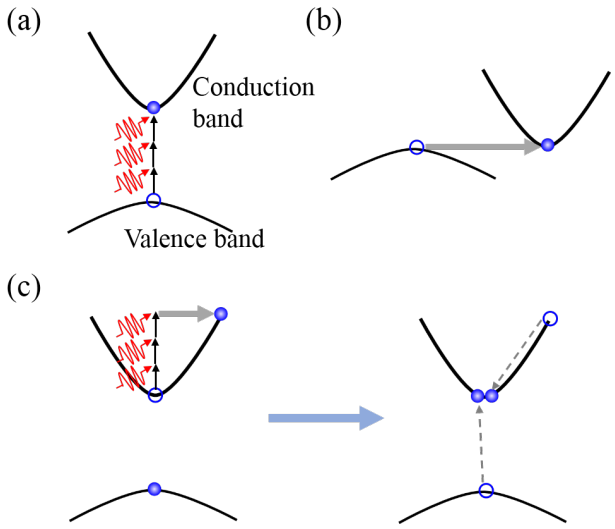

Fig. 2.1: Schematic representation of the different sub-picosecond laser pulse absorption mechanisms within transparent materials. (a) Multiphoton absorption. (b) Tunneling ionization. (c) Free carrier absorption followed by avalanche ionization. This figure has been modified from [6].

For the case of sub-picosecond pulses, the absorption of laser pulses is faster than the energy transfer to the lattice, so the absorption and the heating lattice processes are decoupled [117]. The excited electrons in the conduction band get heated by the laser pulses much faster than they can transfer their energy to the lattice via phonon emission. In this manner, the density of electrons in the conduction band keeps growing until the plasma frequency at the focal volume equals the frequency of the incident laser beam. The plasma frequency is equal to [116]:

$$\omega_p = \sqrt{\frac{e^2 N}{\varepsilon_0 m_e}}\,. \tag{2.2}$$

When the plasma frequency reaches the laser frequency, the plasma is strongly absorptive and the laser energy is absorbed by the plasma via free carrier absorption. Once the laser radiation is not present, the electrons transfer their energy to the lattice. This deposition of energy on a much faster time scale than the thermal diffusion time results in permanent structural modifications within the bulk of the transparent material.

While nonlinear absorptions through multiphoton or tunneling ionizations provide seed electrons for avalanche ionization to occur, the fact that avalanche ionization is present results in a low dependence of the optical breakdown threshold on the optical gap energy, since it only depends

linearly on the laser intensity. Due to this low dependence on the optical gap energy, ultrafast laser writing is a versatile technique that can be employed in a wide range of transparent materials. If only nonlinear photoionizations would take place, the application of the ultrafast laser inscription technique would be highly dependent on the absorption probability with material energy gap and a very limited range of materials could be laser processed under this technique.

Sub-picosecond laser writing, in contrast to nanosecond laser pulse micromachining, provides deterministic breakdown and optical damage for a controllable bulk material modifications due to laser pulse absorptions led by photoionizations which provide seed conduction band electrons for subsequent avalanche ionizations during the rest of the pulse. The self-seeded avalanche process makes short-pulse breakdown less dependent on material defects, resulting in a deterministic material optical damage threshold, in contrast to long-pulse breakdown that relies more on the concentration of impurities in the material [116]. In addition, short-pulse machining uses less energy to achieve the optical intensity needed for breakdown and a more precise laser machining is possible compared to longer pulses. For all these reasons, femtosecond optical pulses are an ideal tool for laser micromachining.

2.1.2 Material relaxation and permanent modification

After the absorption of ultrashort laser pulses in transparent materials through carrier excitations to the conduction band, the electrons transfer their energy to the lattice located within and around the focal volume, resulting in permanent material modifications. The physical mechanisms responsible for a permanent material modification are not yet understood but the morphology of the modifications can be generally classified into three different types of effects: an isotropic refractive index change, a birefringent refractive index change and the formation of voids within the focal volume of the material.

Although the type of permanent modification achieved in transparent materials is dependent on many laser processing parameters (such as pulse energy, wavelength, repetition rate, pulse duration, scan speed or polarization, among others) and on the material properties (such as optical gap

energy or thermal diffusivity, between others), the simplest illustration of a well studied dielectric material is the case of fused silica, which allows to obtain the three different effects mentioned by only changing the incident laser energy.

At low pulse energies (on the order of $\sim$100 nJ, using a focusing objective of 0.6 NA, for 800 nm wavelength and 100 fs pulse duration) but beyond the optical modification threshold, an isotropic refractive index change is achieved within the focal volume of fused silica due to a densification from a rapid cooling of the melted glass [119]. While fused silica experiences a densification of the laser irradiated volume through a rapid quenching from higher temperatures, a rapid quenching in borosilicate glasses results in a reduction of the glass density which leads to a reduced refractive index in the irradiated volume [120]. Other contributions to the formation of an isotropic refractive index in other materials are due to the formation of color centers [20], chemical bond modifications in the material matrix resulting in densification [119], ion migration for the case of multicomponent glasses [121, 122], or a combination of all the mechanisms mentioned. An isotropic distribution of the refractive index is ideal for the fabrication of optical waveguiding structures allowing optical mode confinement via total internal reflection.

At intermediate pulse energies (between 150 - 500 nJ, for a focusing objective with 0.6 NA, at 800 nm wavelength and a pulse duration of 100 fs), a birefringent refractive index change has been obtained within the focal volume of fused silica due to the creation of nanogratings resulting from an interference between the laser electric field and the laser induced electron plasma wave [123, 124]. The laser-written nanogratings have been useful for the creation of buried microfluidic channels with biological lab-on-a-chip applications [125, 126].

Higher pulse energies (beyond $\sim$500 nJ, with a focusing objective of 0.6 NA, 800 nm wavelength and 100 fs pulse duration) lead to pressures within the focal volume of fused silica that are greater than the Young's modulus, leading to the formation of a shockwave that propagates radially outwards and results in the formation of a less dense material or a void, depending on the properties of the material. The surrounding volume of the void cointains a higher refractive index than the pristine material. These laser induced voids have been used as devices for applications in memory storage [127, 128].

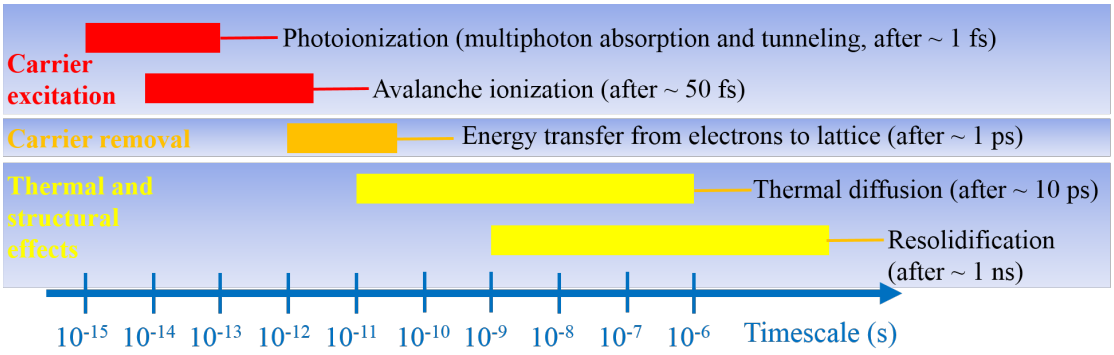

Fig. 2.2: Time scale representation of various physical phenomena involving laser-material interactions. Figure modified from [1].

The interpretation given for the three types of structural modifications considers the interaction of single femtosecond laser pulses within the bulk of fused silica, but these modification regimes can be extended to the contribution of a train of pulses within the laser focal volume assuming that the repetition rate between optical pulses is relatively low in order to allow thermal diffusion between consecutive pulse arrivals [129].

This thesis focuses on femtosecond laser micromachining at the low pulse energy regime in order to achieve isotropic refractive index modifications within the focal volume of dielectrics and semiconductors, leading to structures that permit optical waveguiding.

For the case of femtosecond laser pulses operating at high repetition rates, heat accumulation plays an important role in the material modification since the time between consecutive laser pulses is less than the time needed for the heat to diffuse out of the focal volume [129, 130]. The contribution of femtosecond pulses at high repetition rates results in an increase of the size of the melted volume, which depends on the effective number of pulses in the laser spot that are absorbed at a static exposure, $N = 2\omega_0 R/v$, where $2\omega_0$ is the laser spot diameter at the focal volume, R is the repetition rate between laser pulses and v is the translation speed of the substrate with respect to a fixed incident laser beam [129, 130]. At the cumulative heating regime, the morphology of the structural modifications will be driven by the melting and cooling dynamics of the particular material at the focal volume [129, 130].

2.1.3 Light propagation effects

When using laser machining of sub-picosecond pulses, the first physical phenomenon to occur due to the interaction of sub-picosecond pulses with the material is the nonlinear absorption led by high optical intensities reaching the breakdown threshold of the material. Optical intensities accomplishing the breakdown threshold of common glass have values of about 10^{13} W/cm^2 and can be reached using focusing microscope objectives with high numerical apertures (NA), allowing tighly focused optical beams with a micrometer spot size at the focal volume. However, working at such high optical intensities, linear propagation effects such as dispersion, diffraction or aberration, and nonlinear propagation effects, such as self-focusing and self-phase modulation, need to be accounted since they affect the energy distribution of the optical beam at the laser focus and thus the resulting refractive index modification at the focal volume of the material.

Linear propagation

Assuming the propagation of a Gaussian beam in the absence of any spherical aberration or nonlinear effect and for a small beam divergence, the paraxial approximation can be applied and the transverse intensity distribution of the beam can be written as [131]:

$$I(r,z) = \left(\frac{\omega_0}{\omega(z)}\right)^2 exp\left(-\frac{2r^2}{\omega^2(z)}\right), \tag{2.3}$$

where r is the radial distance and is equal to $\sqrt{x^2+y^2}$, z is the axial distance from the beam waist, $\omega(z)$ is the distance from the beam axis where the intensity drops to $1/e^2$ of the maximum value and ω_0 is the diffraction-limited minimum beam waist radius at the laser focus.

The variation of the laser beam spot size along the axial direction is given by:

$$\omega(z) = \omega_0\sqrt{1+\left(\frac{z}{z_0}\right)^2}. \tag{2.4}$$

The diffraction-limited minimum beam waist radius is:

$$\omega_0 = \frac{M^2\lambda}{\pi NA}, \tag{2.5}$$

being M^2 the Gaussian beam quality factor which is equal to the unit for the case of an ideal Gaussian beam, λ is the optical wavelength and NA is the numerical aperture of the focusing objective.

The Rayleigh range of the focus within a transparent material having a refractive index n is given by:

$$z_0 = \frac{M^2 n\lambda}{\pi NA^2}\,. \tag{2.6}$$

The size of the laser beam at the focal spot when focusing within a transparent material is simply given by ω_0 and z_0 in the transverse and axial directions of the incident laser beam, when neglecting optical aberrations and nonlinear effects. Thus, the peak intensities reached at the focal volume of the material are:

$$I_p = \frac{E_p}{\pi\omega_0^2\tau_p}\,, \tag{2.7}$$

being E_p the optical pulse energy and τ_p the pulse duration.

When accounting for chromatic and spherical aberrations, this causes deviations in the energy distribution of the optical beam at the focal volume and Eq. 2.3, 2.5 and 2.6 are no longer valid. The chromatic aberration can be corrected with focusing objectives which contain chromatic aberration correction for a specific optical wavelength. The spherical aberration is due to a mismatch between the refractive index of air and the refractive index of the substrate under laser processing. Also, the spherical aberration grows with the NA of the focusing objective used and with the writing depth within the substrate, resulting in an axial distorsion of the intensity distribution at the focal volume. Correction of spherical aberration can be achieved with oil-immersed focusing microscope objectives, which correct the refractive index mismatch of the air-substrate interface by using index-matching oil along the optical path between the focusing objective and the top surface of the substrate [132]. However, oil-immersed objectives only provide correction of the spherical aberration for substrates with a refractive index near the refractive index of the oil ($n \sim$1.5). Laser machining of materials containing larger refractive indices requires the use of adaptive optics such spatial light modulators which induce a negative phase distortion of the beam providing focal volumes with spherical shapes within the substrates [133, 134].

Nonlinear propagation

Considering a medium free of charges ($\rho = 0$), free of currents ($\mathbf{J} = \mathbf{0}$) and nonmagnetic ($\mathbf{M} = \mathbf{0}$) the derivation of the Maxwell's equations 2.15 leads to the wave equation:

$$\nabla^2\mathbf{E} - \frac{1}{c^2}\frac{\partial^2}{\partial t^2}\mathbf{E} = \frac{1}{\varepsilon_0 c^2}\frac{\partial^2\mathbf{P}}{\partial t^2}\,, \tag{2.8}$$

where c is the speed of light and is equal to $1/\sqrt{\mu_0\varepsilon_0}$.

When high optical intensities traverse a nonlinear medium, the optical response of the medium is described as a polarization written as a power series of the electric field $\mathbf{E}(t)$ as:

$$\mathbf{P}(t) = \varepsilon_0\left(\chi^{(1)}\mathbf{E}(t) + \chi^{(2)}\mathbf{E}^2(t) + \chi^{(3)}\mathbf{E}^3(t) + \ldots\right), \tag{2.9}$$

where $\chi^{(1)}$ is the linear susceptibility of the material and $\chi^{(2)}$ and $\chi^{(3)}$ are the second and third order nonlinear optical susceptibilities, respectively.

For the simplified case of a centrosymmetric material, such crystals that do not display inversion symmetry, gases, liquids or amorphous solids like glass, the second order nonlinear susceptibility vanishes ($\chi^{(2)} = 0$) and second-order nonlinear interactions do not take place. If fourth and higher order nonlinear effects are neglected, the polarization of a centrosymmetric medium can be written as:

$$\mathbf{P}(t) = \varepsilon_0\left(\chi^{(1)} + \frac{3}{4}\chi^{(3)}|\mathbf{E}|^2\right)\mathbf{E}(t)\,. \tag{2.10}$$

The refractive index of the material is composed of a linear refractive index n_0 and a nonlinear refractive index n_2 variable with the optical intensity (optical Kerr effect) [135]:

$$n = \sqrt{1 + \chi^{(1)} + \frac{3}{4}\chi^{(3)}|\mathbf{E}|^2} = n_0 + n_2 I\,, \tag{2.11}$$

where $n_0 = \sqrt{1+\chi^{(1)}}$, $n_2 = \dfrac{3}{4}\dfrac{\chi^{(3)}}{\varepsilon_0 c n_0^2}$ and $I = \dfrac{1}{2}\varepsilon_0 n_0 c|\mathbf{E}|^2$.

As a response of the material exposed to an intense electromagnetic radiation, a spatial variation of the laser intensity traversing the medium can spatially modifiy the refractive index of the material. For a common medium with a positive n_2, the refractive index of the irradiated area

will experience an increase proportional to the optical intensity traversing the medium, resulting in a self-focusing of the light created along the center of the propagated optical beam, as if the medium were a positive lens (as shown in Fig. 2.3(a)). The self-focusing in the medium is self-sustained until defocusing effects or optical damage interrupt the process. The critical power for self-focusing is given by [135]:

$$P_c = \frac{3.77\lambda^2}{8\pi n_0 n_2}, \tag{2.12}$$

where λ is the optical wavelength and n_0 and n_2 are the linear and nonlinear refractive indices of the medium, respectively. Generally, peak intensities beyond the threshold for optical breakdown ($\sim 10^{13}$ W/cm^2 for common glass) but below the critical power for self-focusing are employed during laser machining in order to avoid waveguides with elongated cross sections. However, exotic nonlinear materials present a challenge for the formation of symmetric laser-inscribed waveguides [47] since they have large values of n_0 and n_2 and the critical power for self-focusing is inversely proportional to the linear and nonlinear refractive indices (see Eq 2.12).

Assuming that the optical Kerr effect is instantaneous, the refractive index will change with the intensity profile of the propagated pulse, being maximum in the central part of the beam. The shift in the optical path due to the variation of the refractive index, $\Delta n(t)z$, results in a phase shift:

$$\Delta\phi = \frac{2\pi z n_2 I(t)}{\lambda}, \tag{2.13}$$

which in turn gives rise to a spectral broadening of the pulse with the leading edge shifted to lower frequencies (red-shifted) and the trailing edge shifted to higher frequencies (blue-shifted), as can be seen in Fig. 2.3(b). This effect is known as self-phase modulation and the increase in the instantaneous frequency that results from it can be written as:

$$\Delta\omega(t) = -\frac{2\pi z n_2}{\lambda}\left(\frac{dI(t)}{dt}\right). \tag{2.14}$$

2.2 Waveguide theory

Optical waveguides are made of dielectric materials and are composed of an inner medium with a high refractive index, known as core, and an outer medium presenting a lower refractive index, the

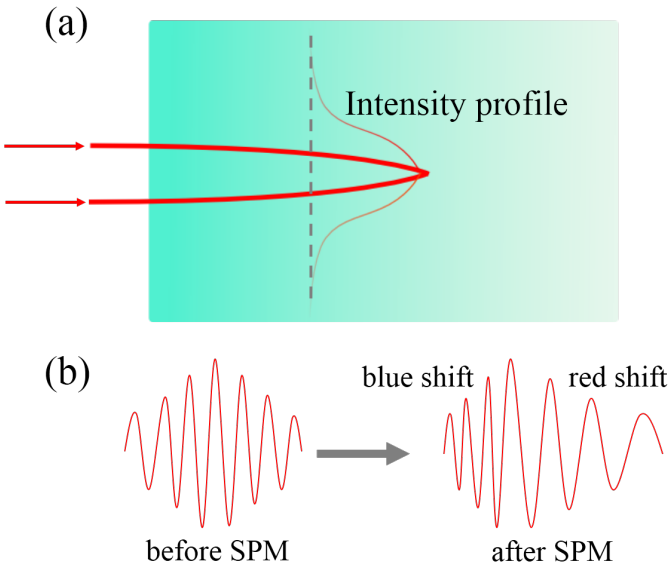

Fig. 2.3: (a) Self-focusing of an optical beam when travelling within a nonlinear medium. (b) Spectral broadening of a pulse when undergoes self-phase modulation (SPM).

cladding. Because of the higher inner refractive index, light can experience total internal reflection and propagate along the waveguide. The optical guided wavelength is comparable to the transverse dimension of the core.

In this section, the guided-wave modes, wich are the solution to Maxwell's equations, are given for the case of transversally symmetric waveguides presenting a step-index profile as an approximation to the shape of the laser-written waveguides fabricated in this thesis. Moreover, the mutual light-wave interaction between two co-propagating modes is given by the coupled mode equations based on perturbation theory, which explain the evanescent coupling experienced by light when is guided along an optical waveguide in enough proximity to another waveguide. This evanescent light coupling can be observed in laser inscribed optical directional couplers fabricated in this thesis for Corning EAGLE2000 (chapter 4, section 4.3) and gallium lanthanum sulfide glasses (chapter 5, section 5.2).

2.2.1 Hybrid guided modes in cylindrical waveguides with step-index profile

Light propagation is governed by Maxwell's equations:

$$\begin{aligned} \nabla \cdot \mathbf{D} &= \rho\,, \\ \nabla \cdot \mathbf{B} &= 0\,, \\ \nabla \times \mathbf{E} &= -\frac{\partial \mathbf{B}}{\partial t}\,, \\ \nabla \times \mathbf{H} &= \frac{\partial \mathbf{D}}{\partial t} + \mathbf{J}\,, \end{aligned} \tag{2.15}$$

where ρ is the free charge density, $\mathbf{J}$ is the current density vector, $\mathbf{E}$ and $\mathbf{H}$ are the electric and magnetic fields, respectively, and $\mathbf{D}$ and $\mathbf{B}$ indicate the displacements related to the electric and magnetic field vectors as:

$$\begin{aligned} \mathbf{D} &= \varepsilon_0 \mathbf{E} + \mathbf{P}\,, \\ \mathbf{B} &= \mu_0 \mathbf{H} + \mathbf{M}\,, \end{aligned} \tag{2.16}$$

where ε_0 and μ_0 are the permittivity and permeability in vacuum, respectively, and $\mathbf{P}$ and $\mathbf{M}$ are the electric and magnetic polarizations, respectively.

Assuming that a laser-written waveguide has a cylindrical shape and is tranversally symmetric with a step-index profile in a homogeneous and lossless dielectric medium, it is convenient to write the Maxwell's equations in cylindrical coordinates (radius r, azimuthal angle θ and axial position z) as follows [136, 137]:

$$\begin{aligned} \frac{1}{r}\frac{\partial E_z}{\partial \theta} + j\beta E_\theta &= -j\omega\mu_0 H_r\,, \\ -j\beta E_r - \frac{\partial E_z}{\partial r} &= -j\omega\mu_0 H_\theta\,, \\ \frac{1}{r}\frac{\partial}{\partial r}(rE_\theta) - \frac{1}{r}\frac{\partial E_r}{\partial \theta} &= -j\omega\mu_0 H_z\,, \\ \frac{1}{r}\frac{\partial H_z}{\partial \theta} + j\beta H_\theta &= j\omega\varepsilon_0 n^2 E_r\,, \\ -j\beta H_r - \frac{\partial H_z}{\partial r} &= j\omega\varepsilon_0 n^2 E_\theta\,, \\ \frac{1}{r}\frac{\partial}{\partial r}(rH_\theta) - \frac{1}{r}\frac{\partial H_r}{\partial \theta} &= j\omega\varepsilon_0 n^2 E_z\,, \end{aligned} \tag{2.17}$$

where n is the refractive index which can be equal to n_1 in the core ($r \leq a$) or equal to n_0 in the cladding ($r > a$), β is the propagation constant and ω is the angular frequency.

If $\overrightarrow{\mathbf{E}} = \mathbf{E}(r,\theta)e^{j(\omega t-\beta z)}$ and $\overrightarrow{\mathbf{H}} = \mathbf{H}(r,\theta)e^{j(\omega t-\beta z)}$ are the electric and magnetic fields in the optical waveguide expressed in cylindrical coordinates, by substituting them into the set of Maxwell's equations 2.17, the wave equations for the z-component of the electromagnetic field are obtained:

$$\begin{aligned} \partial^2 E_z \partial r^2 + \frac{1}{r}\frac{\partial E_z}{\partial r} + \frac{1}{r^2}\frac{\partial^2 E_z}{\partial \theta^2} + \left(k^2 n(r,\theta)^2 - \beta^2\right) E_z &= 0, \\ \frac{\partial^2 H_z}{\partial r^2} + \frac{1}{r}\frac{\partial H_z}{\partial r} + \frac{1}{r^2}\frac{\partial^2 H_z}{\partial \theta^2} + \left(k^2 n(r,\theta)^2 - \beta^2\right) H_z &= 0, \end{aligned} \tag{2.18}$$

where k is the wave number in vacuum and is equal to $k = \omega\sqrt{\varepsilon_0\mu_0}$.

The transverse components of the electromagnetic field (E_r, E_θ, H_r, H_θ) are related to E_z and H_z and can be also calculated:

$$\begin{aligned} E_r &= -\frac{j}{(k^2 n(r)^2 - \beta^2)}\left(\beta\frac{\partial E_z}{\partial r} + \frac{\omega\mu_0}{r}\frac{\partial H_z}{\partial \theta}\right), \\ E_\theta &= -\frac{j}{(k^2 n(r)^2 - \beta^2)}\left(\frac{\beta}{r}\frac{\partial E_z}{\partial \theta} - \omega\mu_0\frac{\partial H_z}{\partial r}\right), \\ H_r &= -\frac{j}{(k^2 n(r)^2 - \beta^2)}\left(\beta\frac{\partial H_z}{\partial r} - \frac{\omega\varepsilon_0 n(r)^2}{r}\frac{\partial E_z}{\partial \theta}\right), \\ H_\theta &= -\frac{j}{(k^2 n(r)^2 - \beta^2)}\left(\frac{\beta}{r}\frac{\partial H_z}{\partial \theta} + \omega\varepsilon_0 n(r)^2\frac{\partial E_z}{\partial r}\right), \end{aligned} \tag{2.19}$$

where the refractive index distribution does not depend on the azimuthal angle θ.

Two out of six electromagnetic components are independent which, usually, are chosen to be E_z and H_z. Assuming hybrid modes ($E_z \neq 0$, $H_z \neq 0$) and applying the boundary condition that E_z and H_z are continuous at $r = a$, being a the core radius of the waveguide, the solutions to the set of wave equations 2.18 are given by the product of the m-th order Bessel function and the $cos(m\theta + \psi)$ or $sin(m\theta + \psi)$, where m is an integer and ψ denotes the phase [136]:

$$E_z = \begin{cases} AJ_m\left(\frac{u}{a}r\right)cos\left(m\theta + \psi\right), & \text{if } 0 \leq r \leq a \\ A\frac{J_m(u)}{K_m(w)}K_m\left(\frac{w}{a}r\right)cos\left(m\theta + \psi\right), & \text{if } r > a \end{cases} \tag{2.20}$$

$$H_z = \begin{cases} CJ_m\left(\frac{u}{a}r\right)sin\left(m\theta + \psi\right), & \text{if } 0 \leq r \leq a \\ C\frac{J_m(u)}{K_m(w)}K_m\left(\frac{w}{a}r\right)sin\left(m\theta + \psi\right), & \text{if } r > a \end{cases} \tag{2.21}$$

where u and w are the normalized wave numbers in the core and cladding, respectively, and are equal to $u = a\sqrt{k^2 n_1^2 - \beta^2}$ and $w = a\sqrt{\beta^2 - k^2 n_0^2}$. The expressions of the tranverse components of the electromagnetic field can be obtained by substituting equations 2.20 and 2.21 into 2.19 and

by applying boundary conditions for the continuity of E_θ and H_θ at $r = a$, more relations for the unknown coefficients A and C can be built, leading to the dispersion relation that defines the solution of the hybrid modes in step-index waveguides:

$$\left[\frac{J'_m(u)}{uJ_m(u)} + \frac{K'_m(w)}{wK_m(w)}\right]\left[\frac{J'_m(u)}{uJ_m(u)} + \left(\frac{n_0}{n_1}\right)^2 \frac{K'_m(w)}{wK_m(w)}\right] = n^2\left(\frac{1}{u^2} + \frac{1}{w^2}\right)\left[\frac{1}{u^2} + \left(\frac{n_0}{n_1}\right)^2 \frac{1}{w^2}\right], \tag{2.22}$$

which determines the discrete values of the propagation constant β of a mode for specific parameters k, n_1 and n_0. A mode is described by the indices m and l of a discrete propagation constant β_{ml}, where m and l represent its azimuthal and radial distributions, respectively. The effective index of the waveguide is given by β/k and the mode is guided when $n_0 < n_{eff} < n_1$, while there will be a radiation mode when $n_{eff} \leq n_1$.

For the case of weakly guiding waveguides, the longitudinal electromagnetic components E_z and H_z are near zero (TEM mode), being z the propagation direction, and their notation is represented by LP_{ml} (linearly polarized) where the two linear polarizations of a mode are orthogonal in the x and y directions and are degenerate, having the same propagation constant and spatial distribution. The waveguides fabricated in this thesis are weakly guiding structures with a refractive index difference $\Delta = n_1 - n_0$ of less than 1% and the approximation $n_1 \cong n_0$ can be made. In this case, the eigenvalue equation 2.22 can be simplified and after applying recurrence relations for the Bessel functions it can be written as [136]:

$$u\frac{J_{m\pm1}(u)}{J_m(u)} = \pm\sqrt{V^2 - u^2}\frac{K_{m\pm1}\left(\sqrt{V^2 - u^2}\right)}{K_m\left(\sqrt{V^2 - u^2}\right)}, \tag{2.23}$$

where $V = ka\sqrt{n_1^2 - n_0^2}$ is the cut-off. Equation 2.23 can be solved for an azimuthal index m, where the components of the equation on the left side intersect with the components on the right, leading to values of u_{ml} and for which the propagation constants β_{ml} can be calculated. There is a cut-off condition for each mode. For a higher order mode, a larger value of the cut-off is needed. For waveguides with a $V < 2.405$, only the fundamental mode LP_{01} is supported and in this case the waveguide is a single mode waveguide.

2.2.2 Coupled mode theory

The optical guided mode in a waveguide is confined within the core of the waveguide and it extends to part of the cladding. If two parallel waveguides are close enough to each other, the part of the propagating optical modes extending out of the core of each waveguide can overlap spatially if the two waveguides are close enough to each other, leading to a periodic light transfer between the two waveguides. The propagation characteristics of the coupled modes can be derived from the solution to Maxwell's equations in the two waveguides, which are different from the characteristic waveguide modes in isolation. However, this analysis becomes too complicated and usually an approximation is provided under the assumption of a weak coupling between the two waveguides, using perturbation theory for the derivation of the coupled mode equations [136].

Assuming a weak coupling, the electric field can be written as a sum of the eigen modes in each isolated waveguide composed of amplitude coefficients that vary along the propagation direction of the waveguides, accounting for the energy exchange between them. For the case of two waveguides, the electromagnetic fields can be written as:

$$\begin{aligned} \mathbf{E} &= A(z)E_1(x,y)exp(j(\omega t-\beta_1 z))+B(z)E_2(x,y)exp(j(\omega t-\beta_2 z))\,, \\ \mathbf{H} &= A(z)H_1(x,y)exp(j(\omega t-\beta_1 z))+B(z)H_2(x,y)exp(j(\omega t-\beta_2 z))\,, \end{aligned} \tag{2.24}$$

where β_1 and β_2 are the propagation constants of the two waveguides.

By substituting the electric field of Eq. 2.24 into the wave equation $\nabla^2\mathbf{E}+n^2(\omega)k^2\mathbf{E}=\mathbf{0}$ and under the assumption of a slowly varying amplitude ($d^2A/dz^2=0$, $d^2B/dz^2=0$) due to weak coupling, the coupled mode equations for two codirectional ($\beta_1,\beta_2>0$) nearby waveguides are [136]:

$$\begin{aligned} \frac{dA}{dz} &= -j\kappa_{12}Bexp\left[-j\left(\beta_2-\beta_1\right)z\right]\,, \\ \frac{dB}{dz} &= -j\kappa_{21}Aexp\left[+j\left(\beta_2-\beta_1\right)z\right]\,, \end{aligned} \tag{2.25}$$

where κ_{12} and κ_{21} are the mode coupling coefficients of the waveguides and have a reciprocity relation of $\kappa_{12}=\kappa_{21}=\kappa$.

The general solutions to the coupled mode equations 2.25 are given in the form:

$$\begin{aligned} A(z) &= \left[a_1 e^{jqz} + a_2 e^{-jqz}\right] exp\left(-j\delta z\right), \\ B(z) &= \left[b_1 e^{jqz} + b_2 e^{-jqz}\right] exp\left(j\delta z\right), \end{aligned} \tag{2.26}$$

where q is an unknown parameter, δ is equal to $\delta = \dfrac{\beta_2 - \beta_1}{2}$ and a_1, a_2, b_1 and b_2 are constants that must satisfy the intial conditions:

$$\begin{aligned} a_1 + a_2 &= A(0), \\ b_1 + b_2 &= B(0). \end{aligned} \tag{2.27}$$

By substitution of the set of solutions 2.26 into the coupled mode equations 2.25 and applying the conditions in 2.27, the expressions obtained are:

$$\begin{aligned} A(z) &= \left\{\left[cos\left(qz\right) + j\frac{\delta}{q}sin\left(qz\right)\right]A(0) - j\frac{\kappa}{q}sin\left(qz\right)B(0)\right\} exp\left(-j\delta z\right), \\ B(z) &= \left\{-j\frac{\kappa}{q}sin\left(qz\right)A(0) + \left[cos\left(qz\right) - j\frac{\delta}{q}sin\left(qz\right)\right]B(0)\right\} exp\left(j\delta z\right), \end{aligned} \tag{2.28}$$

where q is equal to $q = \sqrt{\kappa^2 + \delta^2}$.

Assuming that light is only launched into waveguide 1 at $z = 0$ ($B(0) = 0$, $A(0) = A_0$), the output optical power after evanescent coupling in waveguide 1, known as the through output power P_1, and the output optical power after evanescent coupling in waveguide 2 , known as the cross output power P_2, are equal to:

$$\begin{aligned} P_1(z) &= \frac{|A(z)|^2}{|A_0|^2} = 1 - Fsin^2(qz), \\ P_2(z) &= \frac{|B(z)|^2}{|A_0|^2} = Fsin^2(qz), \end{aligned} \tag{2.29}$$

where F is the maximum power-coupling efficiency and is equal to $F = \left(\dfrac{\kappa}{q}\right)^2 = \dfrac{1}{1 + \left(\delta/\kappa\right)^2}$.

The power coupling ratio (CR) evanescently transferred to the cross waveguide is calculated as the optical power at the cross waveguide port divided by the sum of the total optical power at the through and cross output waveguide ports:

$$CR = \frac{P_2}{P_1 + P_2} = Fsin^2\left(qz\right) = \frac{sin^2\left(qz\right)}{1 + \left(\dfrac{\delta}{\kappa}\right)^2}. \tag{2.30}$$

Thus, the power coupling ratio (CR) is a sine square function which traduces into an optical power oscillation between the two waveguides which reaches its maximum when

$$z = \frac{\pi}{2q}(2n+1) \quad (n = 0, 1, 2, \ldots). \tag{2.31}$$

For the ideal case in which both waveguides have equal propagation constants ($\beta_2 = \beta_1$), the parameter δ becomes zero and the power-coupling efficiency F is equal to the unit, leading to the maximum amplitude possible of the sinusoidal function that describes the power coupling ratio (CR = 1) between the two waveguides, meaning a complete optical energy transfer from the through waveguide (waveguide 1) to the cross waveguide (waveguide 2).

The waveguide length necessary for a full optical power oscillation is given by $z = l_B$, where l_B is known as the beat length of a directional coupler and is equal to $l_B = \pi/q$, which is equal to π/κ when both waveguides have equivalent propagation constants.

2.3 Summary

This chapter has provided relevant information about the physical mechanisms taking place at the focal volume of transparent materials when sub-picosecond laser pulses are focused within the micrometer volume, being responsible for different types of material modifications which can be useful in various applications due to the formation of optical waveguides, nanogratings and voids. Also, a list of possible light propagation effects when focusing laser beams carrying intensities above the optical breakdown threshold of the material has been given and different solutions in order to avoid certain unwanted effects during laser formation of waveguides has been given. The wave-guided theory of light propagation in dielectric waveguides presenting cylindrical shapes with circular cross sections and step-index profiles has been detailed as well, since the waveguides processed under ultrafast laser inscription present similar morphologies.

Chapter 3

Experimental details

This chapter presents a complete description of the general methods employed to fabricate and characterize the optical waveguides included in this thesis. First, the laser machining system employed for waveguide fabrications is explained in detail, followed by a brief description of the mechanical, thermal and optical properties of the materials used as substrates for ultrafast inscription of waveguides. After presenting the relevant material properties, a detailed explanation of the general methods employed during the characterization of the laser-written waveguides is given. Finally, the chapter includes the theoretical and experimental information of an autocorrelator, which has been used to estimate the pulsewidth of the ultrashort laser pulses generated from a Ti:Sapphire oscillator (Ti-Light).

3.1 Micromachining workstation

The femtosecond laser machining system used for all the waveguide fabrications is located at the Istituto Italiano di Tecnologia - Center for Nano Science and Technology, Milano. The working station counts with a fully equipped integrated system necessary for ultrafast laser writing within the bulk of transparent materials. The femtosecond laser source is a Yb:KGW Pharos oscillator

(Light Conversion) whose optical output is regeneratively amplified. The repetition rate can be tuned with a pulse picker from single pulse operation up to 1 MHz. The fundamental wavelength of the laser is centered at 1030 nm with a pulse duration of approximately 300 fs and a maximum output pulse energy of 20 μJ. The generation of second, third and fourth harmonics is available from a customized harmonic generator (Light Conversion). A schematic representation of the laser machining system is depicted in Fig. 3.1.

The power control of the different laser beams available in the system is provided by a series of motorized attenuators (Motorized Watt, Altechna) composed of a half wave plate and a thin film polarizer. Each half wave plate is mounted on a motorized rotating stage, allowing the selection of the power ratio between p-polarized and s-polarized beams for the selection of the optical power required for laser writing. With the selected optical power, the motorized rotation of one more half wave plate allows the selection of the desired laser beam polarization (see Fig. 3.1).

The optical paths of the different laser beams converge at mirror M6 in Fig. 3.1, where the beams are steered to a dichroic mirror that presents a high reflectivity for the optical wavelengths used to laser write and sends the laser beams to a rotating wheel containing different microscope objectives, providing a range of numerical apertures (NA) for focusing the laser beam onto different substrates for several applications. The sample stage (3-axis Fiberglide 3D series, Aerotech) offers displacement along three axis with a resolution of $\sim$1 nm reaching scan speeds up to 300 mm/s.

The transverse alignment of the incident laser beams (fundamental and respective harmonics) on the substrate is provided independently by the translation of a two mirror system. In Fig. 3.1, the translatation of mirrors *flip M1* and *M1* allow the alignment of the fundamental beam along the transverse axes, *x* and *y*, previous to waveguide fabrication. The system of two mirrors composed by *M2* and *flip M3* provides transverse alignment of the second harmonic optical beam. Mirrors *M3* and *flip M5* allow the movement of the third harmonic beam along the transverse axes and, lastly, the transverse alignment of the fourth harmonic beam is facilitated by the two mirror system composed by *M5* and *M6*.

The longitudinal alignment of the laser beam is provided by the various focusing objectives,

offering different focal lengths, and the longitudinal displacement provided by the sample stage. In order to ease the alignment of the laser focal spot onto the substrates, a charged-coupled device (CCD) is placed at the back of the dichroic mirror, collecting the optical back reflection of the focused laser beam at the top surface of the substrate (see Fig. 3.1). This vision system also provides a tracing of the laser induced plasma and waveguide writing in real time.

The integration of all the components in the workstation is interfaced by a computer-controlled software (SCA base) developed by the Workshop of Photonics which offers a simple coding scheme for an optimum laser writing, providing control of all the shutters, power attenuation, polarization, motorized stages and vision system. Additionally, the SCA based software provides feedback, previously to the laser waveguide fabrication, by overlapping the image offered by the vision system and simulating the motion of the substrate placed over the sample stage.

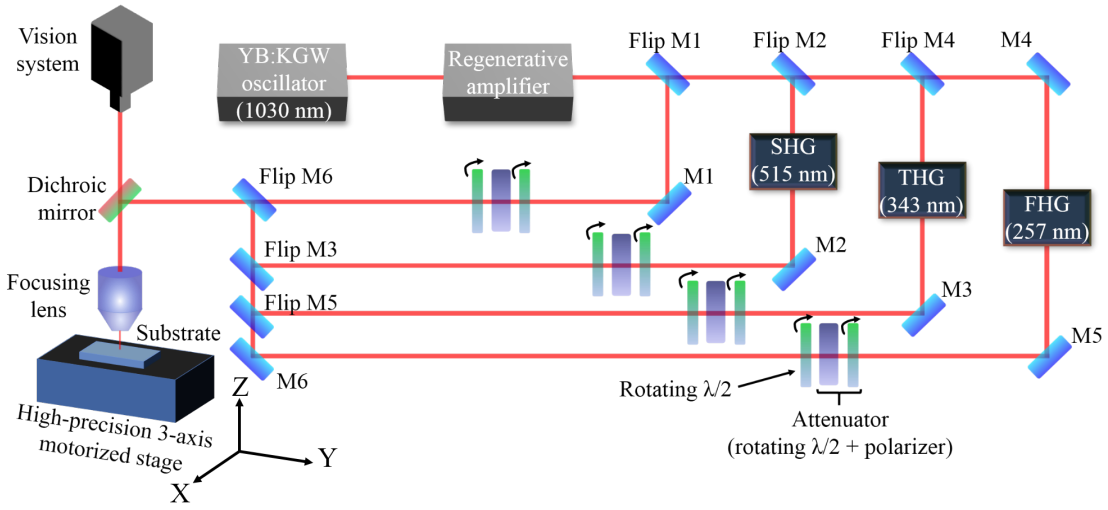

Fig. 3.1: Simplified scheme of the laser micromachining station used for waveguide fabrications. The various optical frequencies generated (fundamental and second, third and fourth harmonics) offer many possibilities for laser writing at different wavelengths (1030 nm, 515 nm, 343 nm and 257 nm). Each optical wavelength counts with an attenuation system given by a half wave plate and a polarizer. A final polarization selection is provided by the rotation of a second half wave plate.

3.2 Material properties

This section includes a description of the properties of the three materials used under laser processing for waveguide fabrications. First, the material properties of Corning EAGLE2000 glass are provided, followed by a detailed description of the synthesis process employed to form gallium lanthanum sulfide (GLS) glass. The experimentally measured transmission spectrum of the synthesized GLS glass is given and specific values of its optical nonlinear properties are provided. Lastly, a description of diamond's physical and optical properties is compared with typical fused silica glass. All the material's thermal properties provided correspond to values at ambient temperature.

3.2.1 Corning EAGLE2000 borosilicate glass

Corning EAGLE2000 glass is an alkaline earth alumino-borosilicate glass that has been extensively used in laser processing. This material was chosen for waveguide inscriptions due to its excellent transmission through visible to near-infrared wavelengths with an ultraviolet absorption edge at around 310 nm, corresponding to an optical gap of $\sim$4 eV, and being a good alternative to fused silica since it allows low-loss waveguides within the high repetition rate laser processing regime comparable to those ones achieved in fused silica [138]. This glass presents a density of 2.37 g/cm^3, a thermal conductivity of 0.89 W/m·K, a Young's modulus of 70.9 GPa and a refractive index of 1.5 at visible and near-infrared wavelengths. The substrates chosen for waveguide fabrications had dimensions of (50 $\times$ 50 $\times$ 1) mm^3.

3.2.2 Gallium lanthanum sulfide glass

Gallium lanthanum sulfide (GLS) glass was chosen as a chalcogenide material to be laser processed since it presents the highest figure of merit among all the chalcogenide glasses and its glass components are non-toxic, unlike other commercially-proven chalcogenide glasses based on

As [3]. The batch of GLS substrates used to laser write waveguides was prepared and supplied by the Optoelectronics Research Centre (ORC) at the University of Southampton. The glass synthesis process consisted on melting a large bulk of a Ga-La-S mixture by adding a small percentage (usually, 1 - 3% by weight) of oxides to the constituent mixture of Ga-La-S. This small percentage of oxide in the form of La_2O_3 decreases the chances of producing a crystallization [3].

The constituent elements (Ga_2S_3, La_2S_3 and La_2O_3) were batched and mixed all together in order to form a homogeneous mixture in a controlled nitrogen atmosphere with % molar of 65%, 32% and 3% for each of the compounds, respectively. The vitreous carbon crucibles used for melting were washed with deionized water and put into an ultrasonic deionized water bath during 1 hour. Immediately after the bath, the vitreous carbon crucibles were placed into a vacuum oven at 80°C for almost half a day. The melting was performed in an in-house built tube furnace adjacent to a water-cooled jacket, supplying a control for quenching rates in order to obtain a uniform glassy melt. The furnace temperature was increased to 1150°C with a ramp rate of 20°C/min and kept for 24 h. After this, the melt was placed in the previously mentioned water jacket for a rapid cooling from 1150°C to room temperature. Then, the glass was annealed at 530°C during 24 h for mitigation of any inherent stress induced during the quenching process [3, 139].

The resultant GLS glass substrates were rectangular slabs with dimensions of ($10 \times 10 \times 1$) mm^3. The linear refractive index of the substrates is 2.4 at near-infrared wavelengths while the nonlinear refractive index reported through a Z-scan is 2.16×10^{-14} cm^2/W [3, 140]. Due to the high linear and nonlinear refractive indices of GLS, this material entails a challenge to be laser processed since the critical power for self-focusing gets reduced by two orders of magnitude compared to fused silica glass (Eq. 2.12).

Fig. 3.2(a) shows the typical yellowish color that GLS gains during the formation of its glass phase, due to a visible absorption edge about 527 nm wavelength. The experimentally measured absorption spectrum of the GLS samples is shown in Fig. 3.2(b), not corrected for reflection losses.

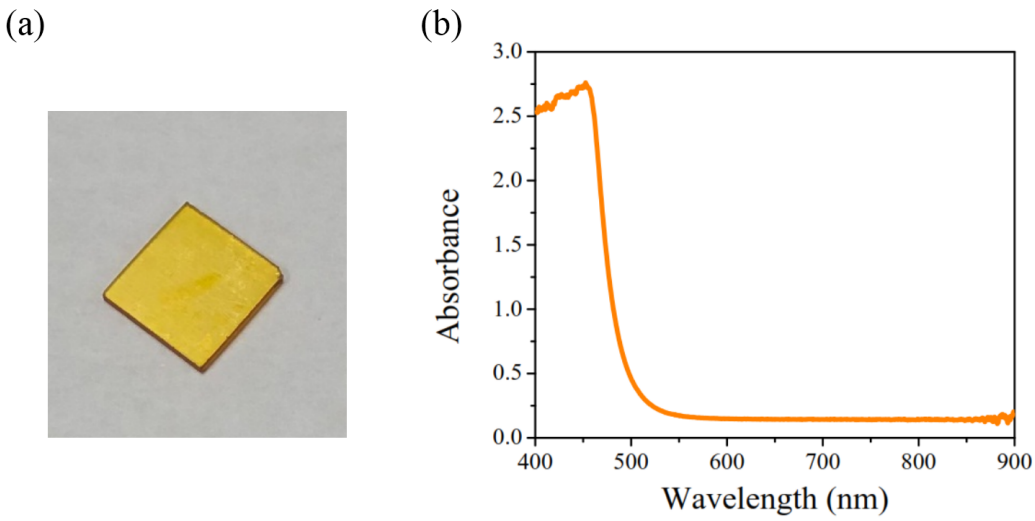

Fig. 3.2: (a) Synthesized gallium lanthanum sulfide glass. (b) Absorption spectrum of the pristine GLS glass substrate.

3.2.3 Diamond

Diamond is a wide-bandgap semiconductor (5.47 eV) whose physical and optical properties, such as high thermal conductivity, chemical stability, mechanical strength and charge mobility together with its wide transparency window make of it an attractive platform for electronic and optics devices. A summary of diamond's physical properties is collected in table 3.1, where a comparison with GLS's and fused silica's properties, being this the best studied dielectric under laser processing, can be made. Its high linear refractive index of 2.4 presents a challenge for being processed under laser writing, reducing the critical power for self-focusing in comparison with fused silica glass (Eq. 2.12).

The diamond substrates used for laser writing of waveguides were single crystal type Ib diamonds synthesized under a process at high pressure and high temperature (HPHT). Type Ib diamond contains single substitutional nitrogen impurities in contrast to other types of diamond

Table 3.1: Comparison between diamond's, GLS's and fused silica's properties [2–5].

Property	**Diamond**	**GLS**	**Fused silica**
Density (g/cm^3)	3.5	4.24	2.2
Thermal conductivity (W/m·K)	2200	0.55	1.3
Tensile strength (GPa)	<60	-	4.8×10^{-2}
Gap energy (eV)	5.47	3.4	9.1
Optical transmission window	225 nm - THz	$\sim$ 500 nm - 10 μm	140 nm - 2.5 μm
n_0 ($\lambda = 1030$ nm)	2.4	2.4	1.45
n_2 (cm^2/W)	1.3×10^{-15}	2.2×10^{-14}	3.5×10^{-16}
$P_c = \frac{3.77\lambda^2}{8\pi n_0 n_2}$ (MW)	0.5	0.03	4
Critical pulse energy (for 300 fs pulses) (μJ)	0.15	0.009	1.2

having nitrogen impurities in aggregated structures [141]. The technique of HPHT involves subjecting a carbon-based material to a high pressure ($>$ 500 GPa) and a high temperature ($>$ 1500°C) in order to induce a phase transition from graphite to diamond. The selected diamond substrates are rich in nitrogen impurity concentration with values of $\sim$100 parts per million. The substrates were provided by MB Optics and consisted of rectangular slabs with dimensions of (3 $\times$ 3 $\times$ 1) mm^3.

3.3 Waveguide characterization

In this section, the general characterization techniques used to check the performance of the laser written waveguiding structures hosted in the three different materials used in this thesis are explained in detail.

Right after waveguide fabrications and before proceeding with the characterization of the waveguides, the input and output sample facets were polished to ensure an optimum optical quality. This end surface treatment allows an improvement of the waveguide coupling loss of up to 2-3 dB, approximately. The polishing method was employed in all the waveguide substrates except in

the case of diamond, due to its high hardness.

3.3.1 White-light optical microscopy

After waveguide inscriptions via the ultrafast laser writing technique and polishing the sample end facets, the morphology of the guiding structures is checked under white-light optical microscopy (Eclipse ME600, Nikon) in transmission mode, in order to properly observe the waveguides formed within the bulk of the substrate, using a variety of magnification objectives between $10\times$ and $40\times$. The examination of the waveguides under microscope allows a primary waveguide characterization from the overhead and transverse views of a waveguide, allowing to estimate the size of the laser-induced modification and obtaining a qualitatively notion of the refractive index change.

For overhead waveguide examination, the samples are placed in such a way that the sample surface closer to the inscribed waveguide is facing the microscope objective used for a magnified waveguide observation. For an examination of the waveguide morphology from a transverse view, the input and output facets of the waveguide can be checked by rotating the substrate by 90°.

Usually, a uniform overhead shape with a better defined central area indicates a positive refractive index contrast with respect to the bulk material, being ideal for the case of type I waveguiding structures. Examples from an overhead type I waveguide are given in Fig. 4.3(a) (chapter 4, section 4.1) and 5.6(a) (chapter 5, section 5.1) from borosilicate and GLS glasses, respectively. For the case of type II waveguides [109], two uniform, parallel and equidistant laser-damaged lines in contrast with the bulk suggest a material phase transformation and a reduction of the refractive index, inferring an optimum type II waveguide formation. This type II of laser writing modality is shown in Fig. 6.5 (chapter 6, section 6.4) from a laser-formed waveguide in diamond.

On the other hand, cross sectional shapes presenting a brighter central core for the case of ultrafast laser writing of usual type I waveguiding in glasses reveal good optical mode confinement, like for the case of waveguides in borosilicate glass illustrated in Fig. 4.3(b) (chapter 4, section

4.1). For the alternative case of ultrafast laser inscription with use of a multiscan modality, promising waveguides present rectangular cross sections which reveal an optimum mode confinement. For instance, laser-induced waveguides in GLS glass fabricated through a multiscan approach present this characteristic rectangular shape of the waveguide trasverse section (see Fig. 5.6(b), chapter 5, section 5.1).

3.3.2 Fiber butt-coupled waveguide characterization

The fiber butt coupling method consists of characterizing a waveguide resorting to the use of an optical fiber to launch light into the waveguide. For the case of waveguides presenting a reasonable morphology under microscope, a fiber butt coupled method was employed for subsequent characterization of the confined optical guided mode and waveguide losses.

Near-field waveguide mode

In order to test the guiding properties of the laser-written waveguides, a laser diode operating at a visible wavelength is coupled to a single mode optical fiber placed on a 3-axis manual positioner with a sub-micrometer resolution (Nanomax MAX313D, Thorlabs). In this case, the visible laser source used to fiber butt couple light into the waveguides operates at 635 nm (LP635-SF8, Thorlabs). The 3-axis manual positioner is used to control the position of the end of the optical fiber needed to butt-couple the light into the waveguide. The substrates are placed on a 4-axis manual positioner (MicroBlock MBT401D, Thorlabs), allowing displacement along the three directions in space plus a tilt rotation for an optimum angle of incidence. The 4-axis positioner enables a long travel displacement of 13 mm along the transverse direction of the laser-written waveguides, in order to characterize substrates containing a large number of guiding structures.

Additionally, the use of a imaging system providing an overhead view of the fiber-waveguide interface for an easier fiber-butt coupling is convenient. In this case, the vision system utilized to ease the launching of light into the waveguides is formed by a magnification microscope objective

(Achrovid 5×, INFINITY) and a complementary metal-oxide-semiconductor (CMOS) camera (DCC1645C, Thorlabs), both of them joint by an adapter tube used to place the camera sensor at the optical image plane of the magnification system.

In this layout, light travelling along the fiber is butt-coupled into a waveguide by approaching the end of the fiber towards the input port of the waveguide under study and checking the light diffraction pattern formed over a white screen at the far field. Once the diffraction pattern showing a bright central circular spot accompanied by concentric interference rings is found, this is indicative of having coupled part of the light coming from the optical fiber into the desired waveguide. This layout can be seen in Fig. 3.3.

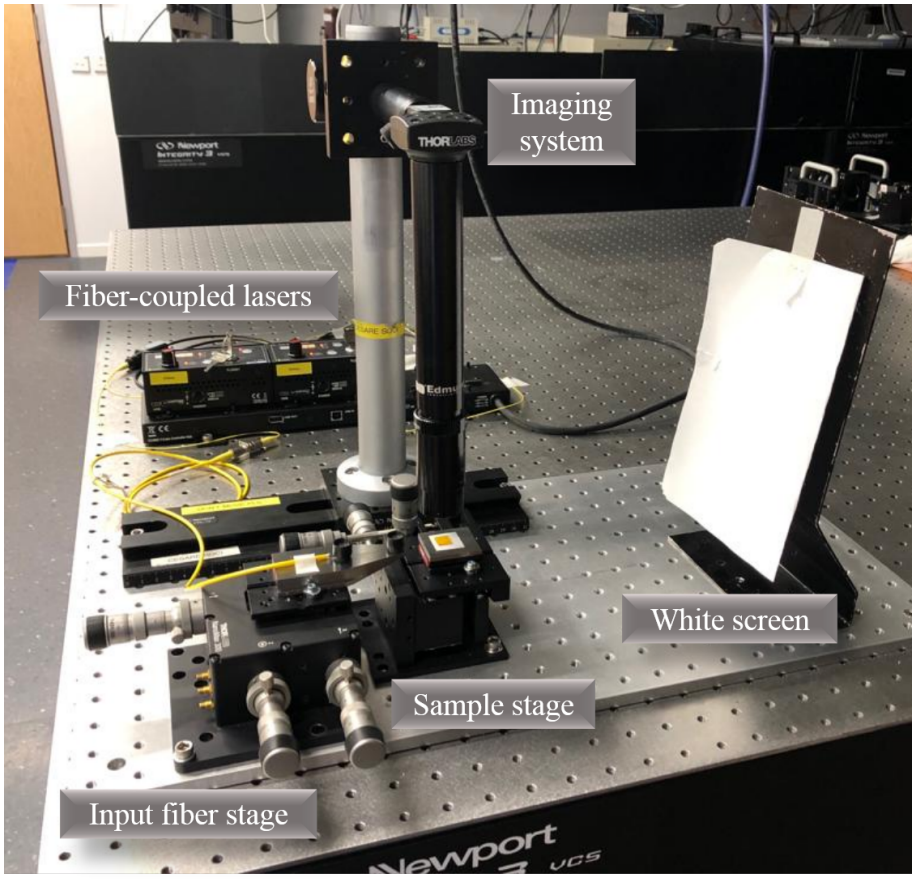

Fig. 3.3: Fiber butt coupling into a waveguide by looking at the far field over a white screen.

With part of the waveguide coupling achieved, a beam profiler (SP620U, Spiricon) attached to a lens tube with an antireflection coated aspheric lens providing a magnification of 60× (5721-

H-B, Newport) is used to image the near-field guided mode profile of the waveguide (see Fig. 3.4). The magnified image of the optical waveguide mode provided by the beam profiler enables an optimization of the fiber-waveguide coupling by carefully moving the manual positioners of the fiber stage within a micrometer resolution. With an optimum fiber-butt coupling achieved, the 635-nm laser diode attached to the input fiber connector is replaced by a laser diode offering the desired operating wavelength for testing the waveguides. The experimental setup used for testing the waveguide mode profiles is shown in Fig. 3.4.

Since laser-inscribed waveguides in Corning EAGLE2000 and GLS glasses were designed to operate in single mode at 800 nm wavelength, a fiber laser diode working at 800 nm (LP808-SF30, Thorlabs) attached to a suitable single mode optical fiber operating at this specific wavelength (780HP, Thorlabs) has been used for characterizing waveguides in the bulk of CorningEAGLE2000 and GLS glass. In the case of diamond substrates, the waveguides are designed to optically guide in single mode at visible wavelengths and a suitable laser source (TLS001-635, Thorlabs) offering a centered wavelength of 635 nm with attachment to single mode optical fiber (SM600, Thorlabs) has been used for waveguide characterizations in diamond.

A fiber-butt coupling into a waveguide with the adequate wavelength enables a quantitative characterization of the near-field mode profile of the waveguide at its output. Waveguides operating at single mode, higher order modes and also presenting various guiding locations due to an inhomogeneous refractive index distribution can be obtained. For the case of waveguides presenting single mode operation, it is convenient to measure the mode field diameter (MFD) of the waveguide mode. The MFD is the diameter at which the maximum optical irradiance (optical power per unit area) is reduced by $1/e^2$ times. The BeamMic software supplied with the beam profiler (SP620U, Spiricon) offers the possibility of performing a complete mode analysis, where the MFD of a waveguide can be measured through the D4-sigma method in which the beam widths in the horizontal and vertical directions are independently calculated by multiplying the standard deviations along the horizontal and vertical marginal distributions by 4.

Ideally, waveguides presenting circular mode profiles with near-Gaussian intensity distributions (Eq. 2.3) and symmetric MFD are searched. Fig. 4.3(c) (in chapter 4, section 4.1) shows an optical guided mode from a waveguide inscribed in borosilicate glass with a near-circular MFD.

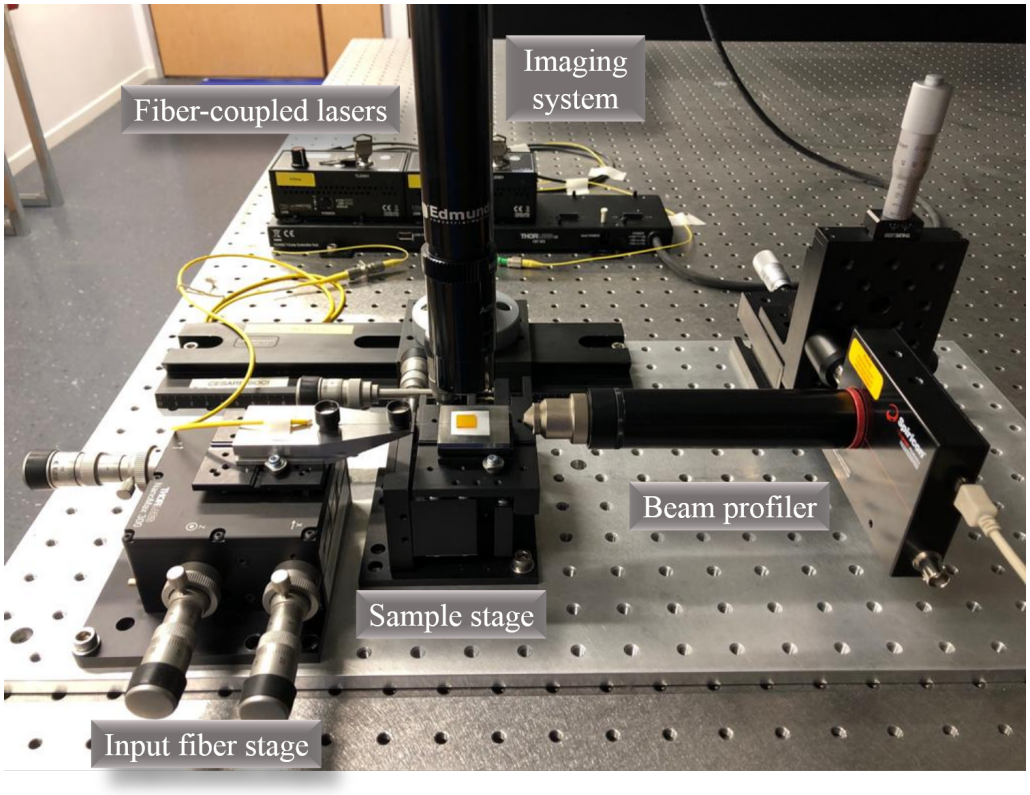

Fig. 3.4: Near-field waveguide mode characterization setup.

Waveguide insertion loss

The overall loss of optical signal power that results from introducing the laser-written waveguide into a fixed transmission line is given by the insertion loss of the waveguide. The insertion loss accounts for the coupling loss at both input and output ports of a waveguide and for the propagation loss along a waveguide.

The measurement of the waveguide insertion loss through a fiber butt coupled method is obtained by launching light into the waveguide from a single mode optical fiber at both input and output ports of the waveguide and measuring the transmitted power along the fiber-waveguide-fiber system, P_t. The transmitted power P_t is then normalized to a reference power, P_{ref} , that corresponds to the power transmitted along a direct butt coupling of the input to the output single mode optical fibers.

The insertion loss of the waveguide is then calculated as the subtraction of the reference power, which is the transmitted power along the fiber-fiber system, P_{ref}, to the transmitted power along the fiber-waveguide-fiber system, P_{t}, when measured in dBm:

$$\mathrm{IL(dB)} = P_{\mathrm{t(dBm)}} - P_{\mathrm{ref(dBm)}}\,. \tag{3.1}$$

For measurement of the transmitted and reference powers, P_t and P_{ref}, a fiber-coupled silicon photodetector (818-SL, Newport Corporation) is used for an optimum power measurement, offering minimum detectable powers of few microwatts. A power meter (843-R-USB, Newport Corporation) interfaced with the silicon photodetector enables the record of the optical transmitted powers. A drop of index matching oil with a refractive index of 1.46 is employed at all the fiber-air-fiber and fiber-air-waveguide interfaces in order to minimize the Fresnel reflection losses and to obtain an accurate power measurement. Fig. 3.5 illustrates the experimental setup used for characterization of the waveguide insertion loss.

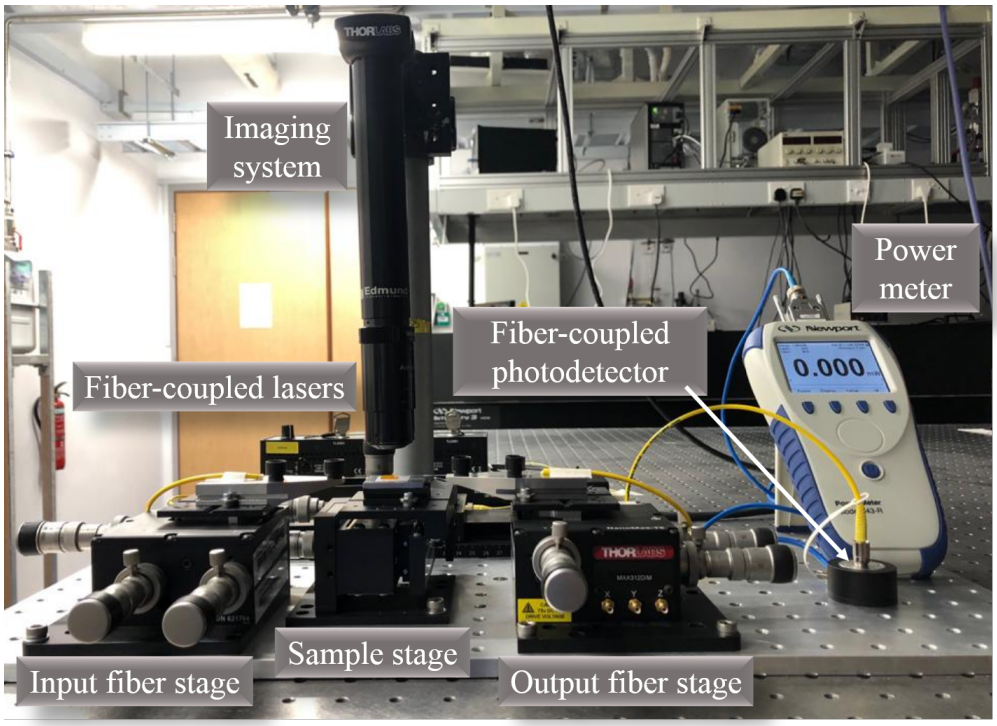

Fig. 3.5: Fiber butt coupling for waveguide insertion loss characterization.

Waveguide coupling loss

In a fiber butt coupled method, the coupling loss is the optical power loss experienced when light is coupled from an optical fiber to the laser-written waveguide, and vice versa. This loss is attributed to a mismatch between the fiber and the waveguide mode profiles. If index matching oil is applied at the interface between the fiber and the laser-written waveguides, losses due to Fresnel reflections are negligible and then the coupling efficiency between the fiber and the waveguide optical modes can be mathematically defined by the overlap integral of these two modes as [142]:

$$\eta = \frac{|\int_{-\infty}^{\infty} \Psi_1(x,y)\Psi_2(x,y)dxdy|^2}{\int_{-\infty}^{\infty}|\Psi_1(x,y)|^2dxdy\int_{-\infty}^{\infty}|\Psi_2(x,y)|^2dxdy}, \tag{3.2}$$

where $\Psi_1 = Aexp\left(-\frac{x^2+y^2}{a^2}\right)$ is the Gaussian electric field distribution along the single mode fiber with a MFD of 2a and $\Psi_2 = Bexp\left[-\left(\frac{x^2}{d_x^2}+\frac{y^2}{d_y^2}\right)\right]$ is the electric field distribution of the waveguide mode which is assumed to be elliptical and has a MFD of $2d_x \times 2d_y$ along x and y axes, respectively.

Taking into account that the coupling loss created from a single facet is mathematically defined as $CL(dB) = 10log_{10}(\eta)$ and substituting the electric field distribution of the fiber and waveguide optical modes, Ψ_1 and Ψ_2, into Eq. 3.2, the coupling loss coming from a single waveguide facet is equal to:

$$CL(dB) = 10log_{10}\frac{4a^2d_xd_y}{(d_x^2+a^2)+\left(d_y^2+a^2\right)}, \tag{3.3}$$

which only depends on the mode size values a, d_x and d_y of the fiber and waveguide, respectively.

Since the MFD of the optical fiber and the waveguides is measured experimentally with the BeamMic software provided by the beam profiler (SP620U, Spiricon), the calculation of the coupling loss, *CL*, can be directly made.

Waveguide propagation loss

The waveguide propagation loss is the loss attributed mainly to scattering and absorption along the length of a waveguide. Since the insertion loss, *IL*, and the coupling loss, *CL*, are experimentally measured, a theoretical estimate of the propagation loss of the waveguides can be made by resorting to the equation:

$$\alpha(dB/cm) = \frac{IL - 2CL}{L}, \tag{3.4}$$

being L the waveguide length in centimeters.

3.4 Time-resolved characterization of ultrashort optical pulses

The characterization of ultrashort optical pulses generated from a Ti:Sapphire femtosecond oscillator (Ti-Light, Quantronix) was carried out through an autocorrelation measurement in order to obtain an approximation of the pulse duration. This solid state laser was later used to interrogate an optical waveguide network designed for the solution of the travelling salesman problem (chapter 4, section 4.4). The laser provided a fundamental wavelength centered at 800 nm, a pulse energy of 1 nJ and a repetition rate of 80 MHz.

The autocorrelation is the most basic method for measuring the duration ultrashort optical pulses, however it does not give information about the phase or about a possible chirp of the pulses. Fig. 3.6 shows the autocorrelator mounted in the lab for the characterization of the optical pulses. In this technique, the pulse to be measured is splitted into two optical beams of equal optical power by using a (50:50, R:T) beam splitter and they are sent to a two-arms optical interferometer, where one of the arms has a retroreflector mounted over a translational motorized stage allowing to introduce a temporal delay (change in optical path length) with respect to the beam traversing the fixed arm in the interferometer. In this case, a hollow retroreflector is used in order to prevent chromatic aberrations, optical path deviations or pulse broadening effects present in prism-type

retroreflectors. Once both the identical pulses have traversed the two arms of the interferometer, they are focused by a plano-convex lens and recombined within a nonlinear medium. In this case, a beta barium borate (BBO) crystal was used as a nonlinear medium to recombine the two optical beams where an angle-tunning method was employed to accomplish the phase-matching conditions required for generation of second harmonic. The BBO crystal was designed to convert light at 800 nm into 400 nm, the crystal thickness was 2 mm and was cut at an angle of 30°. Second harmonic generation (SHG) is a nonlinear effect that only manifests in non-centrosymmetric media, where the second order nonlinear susceptibility, $\chi^{(2)}$, is non-zero (Eq. 2.9). After the BBO crystal, an iris and a SCHOTT BG39 color glass filter were used to remove the two fundamental beams propagated after the BBO crystal. The detection of the filtered second harmonic autocorrelation signal was then carried out using a silicon photodetector. The use of a lock-in amplifier provided a signal detection with an improved signal to noise ratio (SNR) and simultaneous control of the signal detection and the retroreflector position was provided by developing an integration code in LabVIEW software.

It is important to point out the need of satisfying the phase-matching condition which is crucial for achieving SHG within the nonlinear crystal and, thus, producing the desired autocorrelation signal. The phase matching condition for a N-wave mixing process states that [135]:

$$\omega_s = \omega_1 + \omega_2 + \omega_3 + \ldots + \omega_N\,, \tag{3.5}$$

$$\overrightarrow{k}_s = \pm\overrightarrow{k}_1 \pm \overrightarrow{k}_2 \pm \overrightarrow{k}_3 \pm \ldots \pm \overrightarrow{k}_N\,, \tag{3.6}$$

where ω_s and $\overrightarrow{k}_s$ are the frequency and the k-vector of the new signal generated from the nonlinear mixing of N-incident waves into a nonlinear medium. For the case of SHG induced by the mixing of two incident waves carrying the same frequency and polarizations, the phase-matching conditions become $\omega_s = 2\omega_1$ and $\overrightarrow{k}_s = \overrightarrow{k}_1 + \overrightarrow{k}_2$, where ω_1 is the frequency of the two incident beams. If the two incident beams into the nonlinear medium are noncollinear, the transverse components of the two incident k-vectors cancel out and the angle, θ, between the two incident beams must be considered for the case of the longitudinal component (see top right corner in Fig. 3.6). Thus, the phase-matching condition becomes:

$$k_s = k_1 cos\,(\theta/2) + k_2 cos\,(\theta/2)\,, \tag{3.7}$$

where the scalars k_1 and k_2 in Eq. 3.7 are equal since they carry the same frequency and having that $k_s = 2k_1 cos\,(\theta/2)$. Substituting the values of the k-vectors as $k_s = \omega_s n(\omega_s)/c$ and $k_1 = \omega_1 n(\omega_1)/c$,

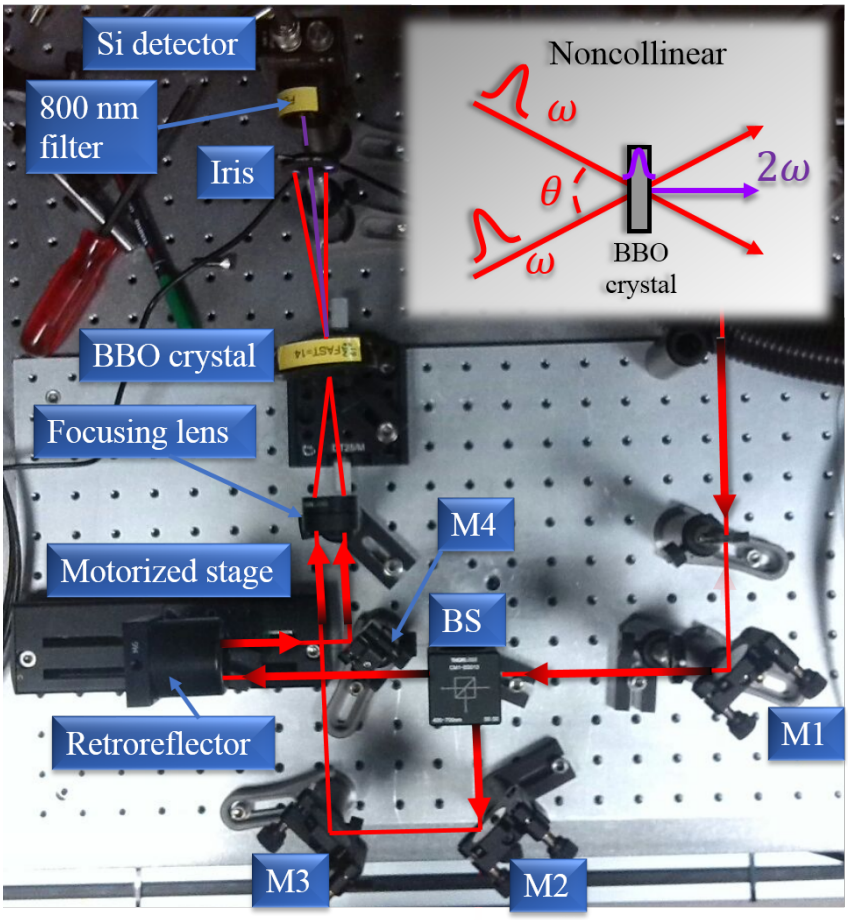

Fig. 3.6: Intensity autocorrelation setup used to characterize the pulsewidth of ultrashort laser pulses generated from a Ti:Sapphire oscillator. The top right corner shows the noncollinear beam modality for SHG in a BBO crystal with an angle of θ between the two incident beams.

and considering the phase-matching condition $\omega_s = 2\omega_1$, the final phase-matching condition is simplified to:

$$n(2\omega_1) = n(\omega_1)cos\,(\theta/2)\,. \tag{3.8}$$

Because the phase-matching condition for SHG in Eq. 3.8 requires the refractive indices of a medium to be equal for two different frequencies, ω_1 and $2\omega_1$, nonlinear processes cannot be generated in usual linear media due to dispersion, where the refractive index changes with the optical frequency. However, the phase-matching condition can be accomplished in birefringent

media, where two orthogonal polarizations follow different refractive index curves. The wave carrying the highest frequency, $\omega_s = 2\omega_1$, is polarized in the direction that gives the lower of the two possible refractive indices. For the particular case of a BBO crystal, which is a negative uniaxial crystal ($n_e < n_0$), the SHG carrying a frequency $\omega_s = 2\omega_1$ has the polarization of the extraordinary wave (see Fig. 3.7). The type of phase-matching achieved in this autocorrelation signal was a type I phase-matching, since both incident beams had the same polarization, which corresponds to the polarization of the ordinary wave.

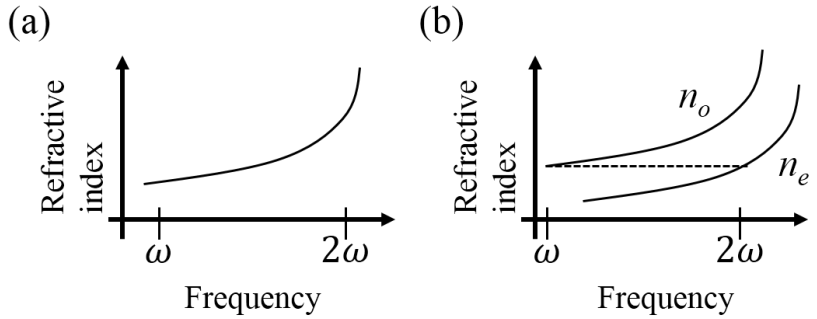

Fig. 3.7: (a) Typical dispersion curve of a linear medium where the refractive index varies with wavelength. (b) Dispersion curve of a birefringent negative uniaxial crystal ($n_o > n_e$) where two orthogonal polarizations experience different refractive index curves.

Mathematically, the generated second harmonic signal within the nonlinear crystal will have an intensity proportional to [143]:

$$I_{sig}^{SHG}(t,\tau) \propto I(t)I(t-\tau)\,, \tag{3.9}$$

where $I(t)$ is the intensity of the optical pulse coming from the fixed arm of the interferometer, $I(t-\tau)$ is the intensity of the delayed pulse in the interferometer and τ is the delay introduced. Since detectors are not fast enough to resolve the overlapping interference fringes in $I_{sig}^{SHG}(t,\tau)$, the obtained intensity autocorrelation signal is the time integral:

$$A^{(2)}(\tau) = \int_{-\infty}^{\infty} I(t)I(t-\tau)dt\,, \tag{3.10}$$

which contains a measure of the pulse length and has its maximum at $\tau = 0$, when both optical pulses match perfectly in time within the nonlinear crystal.

Since the retroreflector positions along the arm of the interferometer during the autocorrelation

measurements are known, its equivalence in time is given by $\Delta t = 2 \cdot \Delta L/c$, where ΔL is the displacement travelled by the retroreflector and c is the speed of light in vacuum. The second harmonic autocorrelation signal obtained in the lab is illustrated in Fig. 3.8.

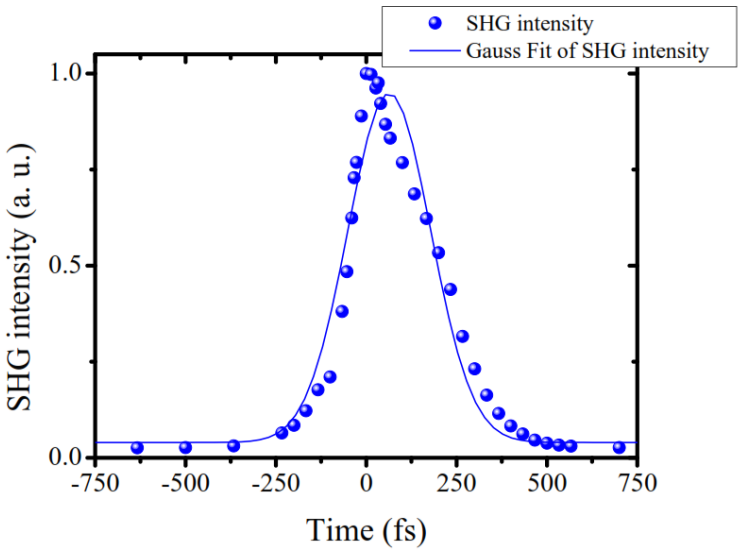

Fig. 3.8: Intensity autocorrelation of ultrashort pulses generated from a Ti:Sapphire ocillator fitted into a Gaussian temporal profile. The FWHM of the autocorrelation trace is 270 $\pm$ 3 fs.

The duration of the autocorrelation signal at its full width at half maximum (FWHM), which corresponds to the width measured at one half of the maximum signal amplitude, is 270 $\pm$ 3 fs. Depending on the temporal profile of the optical pulse, a specific type of deconvolution factor must be applied in order to obtain an approximated value of the original pulse duration. Table 3.2 provides various deconvolution factors depending on the type of temporal profile of the pulses. In this case, a Gaussian temporal profile was assumed and a deconvolution factor of $\sqrt{2}$ was applied, resulting in an autocorrelation of laser pulses with a pulsewidth of 190 $\pm$ 2 fs.

Table 3.2: Different deconvolution factors for the estimation of the pulse duration coming from an autocorrelation signal.

Temporal pulse profile	**Deconvolution factor**
Gaussian	$\sqrt{2}$
sech^2	1.543
Lorentzian	2.0

3.5 Summary

The practical considerations necessary for the fabrication of waveguides through the ultrafast laser writing technique have been covered, starting from the laser machining station employed for waveguide fabrications, followed by the properties of the materials selected to be laser processed and proceeding with the general characterization methods employed to check the performance of the waveguides. Additionally, the last part of the chapter has included a detailed description of the autocorrelator used to estimate the duration of femtosecond optical pulses coming from a Ti:Sapphire laser oscillator. With all this, the chapter provides all the practical tools needed for laser processing and characterization of optical waveguides in transparent materials.

Chapter 4

Direct laser inscription of optical waveguides in borosilicate glass

This chapter covers the fabrication and characterization of ultrafast laser inscribed wave guides, double S-bends and directional couplers in Corning EAGLE2000 glass. An optimum processing window ensuring single mode guiding at 800 nm wavelength has been determined. The convenient wavelength selected opens the possibility of building optical circuits compatible with Ti:Sapphire lasers and spontaneous parametric down-conversion (SPDC) sources for their use in the quantum regime. Also, waveguide simulations have been performed with Rsoft BeamPROP software for a comparison with the experimental waveguide results. A study of the pulse broadening effect of femtosecond pulses travelling along a 5-cm straight waveguide has been investigated. The effect of pulse broadening was found to be relatively low, thus laser-written waveguides are suitable for ultrafast photonics. Also, the reproducibility offered by the femtosecond laser inscription technique has been tested through the study of the power splitting ratio for a wide range of directional couplers and an optimum processing window for the fabrication of 3-dB directional couplers has been selected for future fabrications. The last part of the chapter focuses on the applicability of direct laser-written optical networks as a feasible approach for efficiently solving complex computational problems. The approach presented here has been inspired by the work done by Wu et al. [144], where an optical oracle built with optical fibers can solve the famous salesman problem

for a 5-nodes graph. Here, the use of a laser-written optical oracle demonstrates down-scaling of the optical network from meters to the centimeter length scale in device size, therefore allowing to move from the nanosecond to the femtosecond time domain and leading to faster execution times than the work developed in optical fiber. By interrogating the optical oracle with ultrashort laser pulses, it has been possible to distinguish all the different paths traveled by light within a single operation and thus inferring the existence or the absence of a Hamiltonian solution in the network. This work has been published in [42], proving that factorial problems may be directly laser inscribed in integrated photonic networks, optimizing computation times while obtaining smaller network size.

4.1 Ultrafast laser inscription of waveguides in borosilicate glass

The fabrication of waveguides via the femtosecond laser writing technique in commercial Corning EAGLE2000 borosilicate based glass substrates is described in this section. EAGLE2000 glass is a well-known material used as a hosting substrate for laser processing of different structures by many research groups [31, 130, 145]. Its linear refractive index of $\sim$1.5, its wide optical transparency window covering wavelengths from visible to far infrared values and its reported waveguide thermal stability up to 800°C [138] make it a straightforward platform for bulk waveguide inscription.

Waveguides were directly laser written in the glass substrates in order to obtain single mode waveguides at 800 nm wavelength for optical circuits adaptable to light sources such as Ti:Sapphire lasers for ultrafast light technologies and SPDC light sources for quantum information processing. The laser used for waveguide fabrications corresponds to the micromachining workstation detailed in chapter 3, section 3.1. The 3-axis motion stages included in the workstation were used to translate the glass samples relative to the laser beam, in order to form the photonic structures. The inscription parameters chosen from the machining system were the fundamental wavelength of the system, 1030 nm, ensuring nonlinear multiphoton absorption for waveguide fabrications, 300

fs pulse duration, a repetition rate of 1 MHz and a 0.42 NA focusing objective, resulting in a focal volume within the bulk of $\sim$2.2 μm. High repetition rates ($>$ 500 kHz) were used since it has been demonstrated that they lead to a superior guiding due to heat accumulation effects that affect the waveguide morphology [130]. Also, a focusing objective with a low NA has shown to notably reduce the spherical aberration in waveguide fabrications [138].

In order to find optimal processing parameters ensuring fabrication of low-loss single mode waveguides at 800 nm wavelength, a broad window of incident powers ranging from 100 mW to 500 mW, corresponding to pulse energies between 100 nJ to 500 nJ, was employed in steps of 50 mW. Translation speeds were chosen for a range of values between 10-70 mm/s in steps of 10 mm/s. The waveguides were inscribed within the bulk of ($5 \times 5 \times 1$) cm^3 EAGLE2000 glass substrates at 150 μm below the glass surface.

The morphology of the direct laser formed waveguides was characterized via white-light microscopy in transmission mode, as described in chapter 3, section 3.3. Waveguide transmission measurements were carried out via the fiber butt coupled method. The near-field modes guided along the waveguides were collected with a 60$\times$ aspheric lens (5721-H-B, Newport) to image the mode onto a beam profiler (SP620U, Spiricon).

A first waveguide characterization from the broad processing window of pulse energies and scan speeds employed is shown in Fig. 4.1. Applying pulse energies below 300 nJ did not reveal any structural modification from a rough characterization under white-light microscopy. At 300 nJ pulse energy, some modified traces revealing the formation of a waveguide were observed under miscrocope at applied scan speeds below 20 mm/s. Higher translation speeds at a pulse energy of 300 nJ did not create any visible modifications in the substrate. Fabrications at 350 nJ showed waveguide traces in the bulk of the substrates but presented very weak modifications leading to high insertion loss structures. A narrow processing window of pulse energies, 400-450 nJ, and a broad processing window of scan speeds, 10-70 mm/s, led to small and confined modifications at the focal volume which resulted in single mode waveguides at 800 nm wavelength. Fabrication pulse energies above 450 nJ induced larger modifications at the focal volume resulting in structures with multimode guiding.

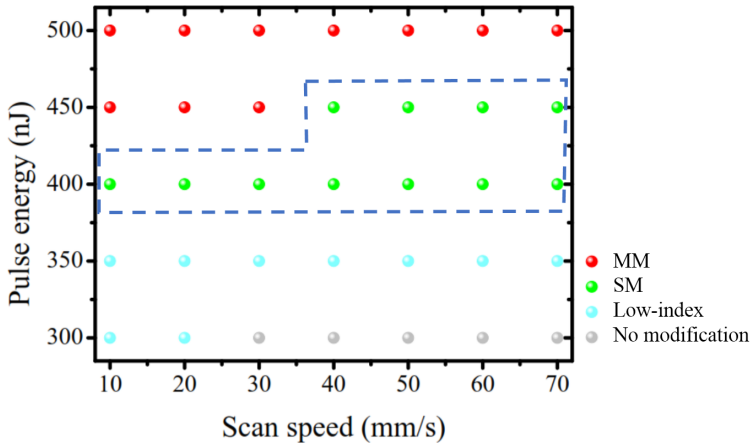

Fig. 4.1: Waveguide classification at 800 nm wavelength from a broad processing window of pulse energies and scan speeds in EAGLE2000 glass substrates. MM and SM indicate multimode and single mode waveguiding, respectively. The area within the dashed lines corresponds to the optimum processing window.

For pulse energies and scan speeds leading to the formation of single mode waveguides, a study of the effect that these parameters had on the insertion loss (IL), mode field diameter (MFD), coupling loss (CL) and propagation loss (α) of the waveguides is depicted in Fig. 4.2. Keeping the fabrication pulse energy constant, the effect of writing waveguides at faster speeds resulted in waveguides with lower insertion losses (Fig. 4.2(a)). This general trend can be observed for two set of waveguides written at 400 nJ and 450 nJ pulse energy. Simultaneously, increasing the translation speed led to less confined modes, presenting larger mode field diameters (Fig. 4.2(a)). This can be observed for optimum pulse energies (425 $\pm$ 25 nJ) where the MFD increases for higher values of the scan speed. Moreover, Fig. 4.2(b) presents the results of the waveguide coupling loss and propagation loss as a function of the scan speed and for the optimum pulse window of 425 $\pm$ 25 nJ.

The relation between the trends of the coupling loss and propagation loss with the general trend of the mode field diameter and insertion loss can be observed from Fig. 4.2(a), respectively. The coupling loss becomes larger for faster translation speeds regardless the pulse energy used. This general increase follows the same behaviour as the MFD of the waveguides, since the coupling loss is calculated as the power loss when light is coupled from the optical fiber used in the fiber butt coupled method into the laser written waveguide. The coupling loss is then related to a

mismatch between the fiber and the waveguide mode profiles, resulting in parameters following similar trends. Most of the insertion loss contribution is from propagation loss, with the general trends between IL and α being similar. An improvement in the IL with writing speeds may be associated to a change in surface roughness with writing speeds. Higher losses due to scattering are obtained at lower speeds while at faster speeds the waveguides may become smoother. The optimum waveguides with IL below 6 dB were achieved at a pulse energy of 450 nJ and for scan speeds between 50 mm/s to 70 mm/s. A minimum insertion loss of 5.1 dB was achieved for 450 nJ pulse energy and 70 mm/s scan speed, with a reported propagation loss of 0.8 dB/cm and a coupling loss of 0.6 dB per facet. These waveguide losses are similar to other results reported by other groups at 800 nm wavelength [31, 145].

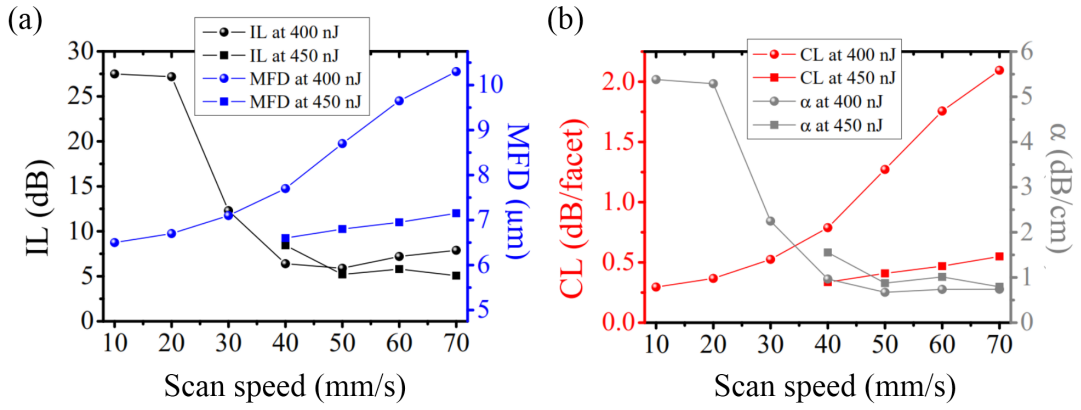

Fig. 4.2: (a) Waveguide insertion loss (*IL*) and mode field diameter (*MFD*) as a function of the scan speed for an optimum pulse energy window of 400 nJ and 450 nJ. (b) Waveguide coupling loss (CL) and propagation loss (α) as a function of the scan speed for an optimum pulse energy processing window of 425 $\pm$ 25 nJ.

Although waveguides written at 450 nJ and 70 mm/s presented the lowest insertion losses, other processing parameters were considered for optical circuit implementations in borosilicate glass platforms due to the inability of the machining system to inscribe the arcs of directional couplers at high speeds. A processing pulse energy and translation speed selection of 450 nJ and 50 mm/s allowed the fabrication of waveguides with S-bend geometries with insertion losses of 5.2 dB. Fig. 4.3(a) shows an overhead optical microscope image of the straight laser written waveguide processed at 450 nJ and 50 mm/s. The characteristic core-cladding structure for buried laser-written waveguides in borosilicate glass written at high repetition rates (1 MHz) can be observed [130]. Assuming a Gaussian temperature distribution at the focal volume, the inner core is

formed due to a high heat accumulation at the laser focal spot leading to a higher refractive index contrast. In comparison, the outer cladding volume has a smaller refractive index contrast due to a lower temperature contribution by means of thermal diffusion just above the melting point of the glass. The final size of the core is due to the contribution of the laser spot size at the focal volume ($\sim$2.2 μm) whereas the overall size of the cladding is determined by the spatial point where the temperature overtakes the softening point [130]. Ion migration may also contribute to the core-cladding structure in borosilicate glass [146].

Fig. 4.3(b) shows the cross section of the corresponding waveguide, with a typical ellipsoidal shape owing to rapid cooling from the melted volume [138]. A non-uniform refractive index profile has been reported in EAGLE2000 glass as a consequence of a resulting non-uniform glass density due to different cooling rates from different melted glass points [130]. This can be clearly observed from the cross sectional image of the waveguide. The small dark spot located at the lower area of the cladding has been previously explained as the position where the focal plane of the objective lens is located [138]. The higher darker contrast of the small spot reveals that most of the energy pulse was deposited at this focal plane. The corresponding guided mode at 800 nm wavelength is shown in Fig. 4.3(c). A nearly circular single mode waveguide with a MFD of 6.5 μm $\times$ 7.1 μm was achieved, similar to other results presented by other groups in commercial EAGLE2000 glass substrates [31, 145]. The waveguide losses reported through the fiber butt coupled method correspond to a propagation loss of 0.9 dB/cm, a coupling loss of 0.4 dB per facet and an insertion loss of 5.2 dB.

4.2 Waveguide pulse broadening characterization

A rough characterization of the pulse broadening effect of femtosecond pulses travelling along the laser-written waveguides in EAGLE2000 glass was investigated via an optical cross-correlator similar to the autocorrelation explained in Fig. 3.6 (chapter 3, section 3.4). The main aim of this measurement was to check the effect that the dispersion of the fabricated waveguides had over the pulsewidth of femtosecond pulses.

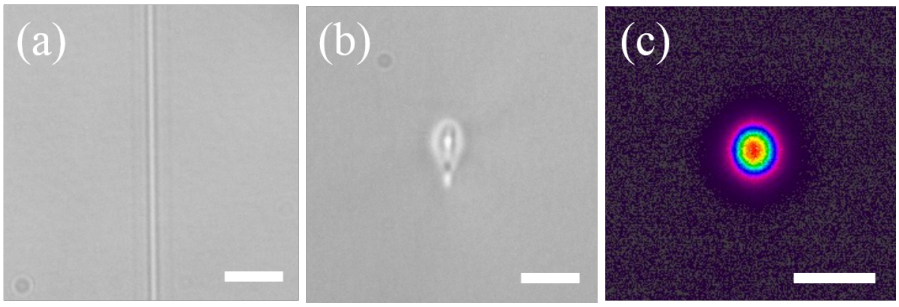

Fig. 4.3: (a) Overhead white-light microscopy of an ultrafast laser inscribed waveguide in EAGLE2000 glass. The core and cladding zones are clearly differentiated. (b) White-light mocroscopy of the cross-sectional view of a waveguide collected from its end facet. (c) Waveguide guided single mode at 800 nm wavelength with a MFD of 6.5 μm $\times$ 7.1 μm^2. The scale bars correspond to 10 μm.

The optical cross-correlator was set to check the pulse broadening of the femtosecond pulses coming from a Ti:Sapphire (Ti-Light) femtosecond oscillator after being coupled into a 5-cm long waveguide. This correlation setup is similar to the autocorrelation shown in chapter 3 with the only difference that a 5-cm length waveguide was placed between mirror M_2 and mirror M_3 along the fixed arm of the interferometer (Fig. 3.6). A 0.16 NA microscope objective was used to focus the light into the waveguide while a 0.25 NA lens was used to collimate the light at the output of the waveguide. After this, both light beams of the interferometer were directed to a nonlinear BBO crystal where the phase-matching conditions were satisfied in order to generate the second harmonic correlated signal. The detection of the correlated signal was realized using a silicon photodiode in connection to a lock-in amplifier for an optimum signal to noise ratio (SNR). During experimental data collection, a LabVIEW program allowed the simultaneous control of the components composing the correlator.

The plot in Fig. 4.4 shows the correlation of a waveguide inscribed in the bulk of EAGLE2000 glass with a length of 5 cm. The overall integrated signal has been fitted into a Gaussian curve with a FWHM equal to 285 $\pm$ 3 fs. Recalling a FWHM of 270 $\pm$ 3 fs from the autocorrelation signal generated from the output pulses coming from the Ti-Light oscillator (chapter 3, section 3.4), a broadening pulsewidth difference of 15 $\pm$ 6 fs between the cross-correlated and autocorrelated signals was obtained. The measured pulse broadening is relatively low, thus the laser-inscribed waveguides in EAGLE2000 glass are suitable for ultrafast optics.

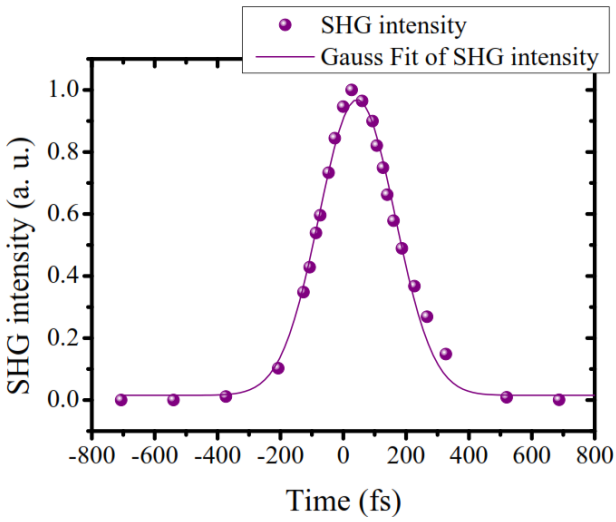

Fig. 4.4: Optical cross-correlation traces of a 5-cm laser-written waveguide in EAGLE2000 glass fitted to a Gaussian function.

4.3 Direct laser inscription of optical directional couplers

Prior to the inscription of directional couplers, optical waveguides with double S-bend geometries were laser written over a range of radii of curvature in order to find the optimum balance between waveguide bend losses and axial device size.

The writing conditions of the fabricated double S-bends correspond to the previously chosen irradiation pulse energy of 450 nJ and a scan speed of 50 mm/s, which led to the fabrication of low-loss single mode waveguides at 800 nm wavelength. Waveguides with double S-bend geometries were fabricated with different radii of curvature between 30-60 mm in steps of 10 mm. Also, theoretical simulations with Rsoft BeamPROP following the beam propagation method (BPM) were performed for a comparison with the experimental bend loss. For waveguide simulations, a core diameter of 2.5 μm was chosen, matching with the core diameter from the microscope image in Fig. 4.3(a). Also, a step linear refractive index profile was assumed during simulations and a refractive index increase of $\Delta n = 4.5 \times 10^{-3}$ was chosen since it led to a waveguide with a MFD of $\sim$7 μm, close to the experimental value.

A comparison between the experimental and the simulated waveguide bend loss as a function

of the bend radius is displayed in Fig. 4.5. As expected, the bend loss decreases as the radius of curvature becomes larger. A small discrepancy between theoretical and experimental bend losses in Fig. 4.5 is attributed to the simplified assumption of a step index profile, as the actual refractive index of the waveguide is more complex since it follows a non-uniform glass density distribution, as shown in Fig. 4.3(b). Also, the change in the physical device size as the bend radius keeps increasing is plotted in Fig. 4.5. For future device implementations, a reasonable trade-off between bend loss and device size was chosen for a radius of curvature of 40 mm.

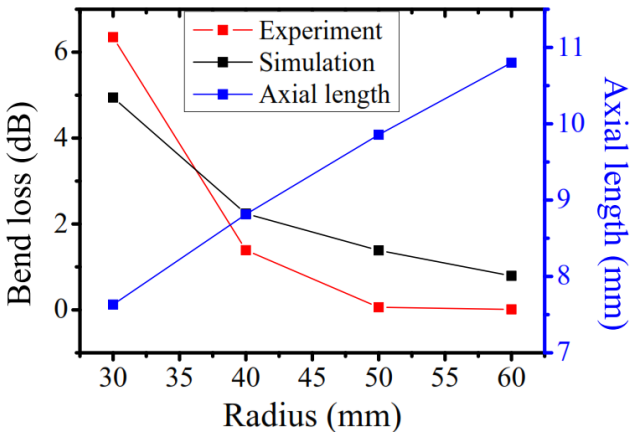

Fig. 4.5: Effect of a variable bend radius over experimental and simulated waveguide bend loss and physical device size.

Optical directional couplers with S-bend geometries were laser inscribed in EAGLE2000 glass. A directional coupler consists of two waveguides linked to two S-bends leading to an interaction region where both waveguides are close enough to enable evanescent light coupling between them (Fig. 4.6). A range of core-to-core separation distances, s, and interaction lengths, L, were studied. The bend radius chosen for directional coupler fabrications was $R = 40$ mm, ensuring a good compromise between waveguide bend loss and device size (Fig. 4.5). Core-to-core separation distances of 6, 7, 8 and 10 μm were studied for directional couplers covering different interaction lengths.

BPM simulations of optical directional couplers in EAGLE2000 glass were also performed in order to see the change in power coupling ratio for different directional couplers with specific core-to-core separation distances and interaction lengths. The power coupling ratio is calculated

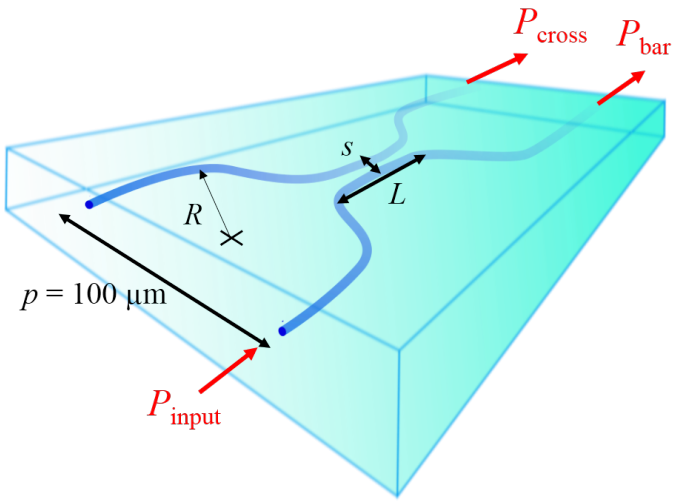

Fig. 4.6: Directional coupler with a S-bend geometry and its parameters: pitch between access ports (p), bend radius (R), core-to-core separation distance (s) and interaction length (L). The optical input power in one of the arms of the directional coupler is indicated as P_{input} and the bar and cross output powers are indicated as P_{bar} and P_{cross}, respectively.

as

$$CR = \frac{P_{cross}}{P_{bar} + P_{cross}}, \tag{4.1}$$

and it changes with the interaction length.

After a careful theoretical and experimental study of the coupling behaviour at different interaction lengths for directional couplers with core-to-core separation distances of $s = 6$, 7, 8 and 10 μm, the beat length, which is the length necessary for a full power coupling ratio oscillation, was plotted as a function of the core-to-core separation distance. The results are displayed in Fig. 4.7 where the beat length increases with the waveguide separation, since the coupling coefficient falls off exponentially with increasing distance. The discrepancy between the experimental and the simulated beat length is attributed once more to the simplified assumption of a step index profile of the waveguide refractive index in the simulations.

In the search for optimum 3-dB couplers inscribed within a minimum space for future implementations in more complex optical networks, Fig. 4.8 shows the power coupling ratio in directional couplers with 6, 7 and 8 μm separation distance as a function of the interaction length. The

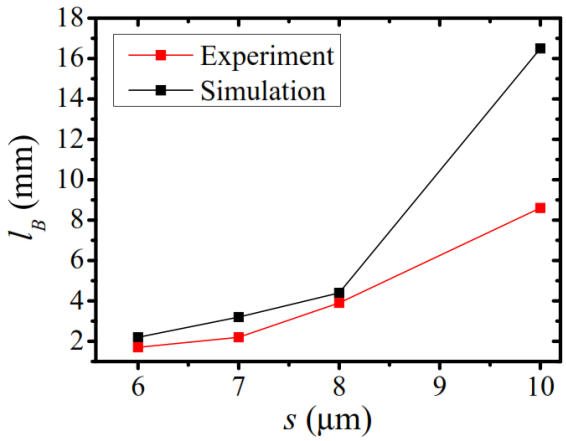

Fig. 4.7: Experimental and simulated beat length as a function of the core-to-core separation distance in laser-written optical directional couplers in EAGLE2000 glass.

experimental data points were fitted into a sine squared function according to coupled mode theory (chapter 2, section 2.2.2). Shorter separation distances below $s = 6$ μm could not be exploited since directional couplers were more sensitive to fabrication fluctuations. In all cases, the power coupling ratio varies sinusoidally between 0 and 1 as predicted by coupled mode theory [147]. To avoid any influence from fabrication fluctuations, as well as keeping a smaller device size, a separation distance of 7 μm was selected for future directional coupler building blocks. From the fitted sine square function at $s = 7$ μm, an interaction length of $L = 700$ μm for a 50:50 power splitting ratio was chosen as the most optimum 3-dB coupler achieved in borosilicate glass at 800 nm wavelength.

In order to use the directional couplers inscribed in borosilicate glass as the basic building blocks of future optical networks, a study of the directional coupler reproducibility via direct laser writing technique was performed. Three sets of directional couplers with a separation distance $s = 7$ μm were performed over a range of interaction lengths $L = 0$ - 2800 μm in steps of 200 μm. The three sets of directional couplers were fabricated on different days in order to check the laser stability and its fabrication reliability. Fig. 4.9(a) shows the results obtained from the three experiments conducted, where the three experimental sets of data points are fitted into a sine square function. The adjacent plot in Fig. 4.9(b) shows the main value (black squared dots) from the three sets of experimental data points in Fig. 4.9(a) and the error bars indicating the

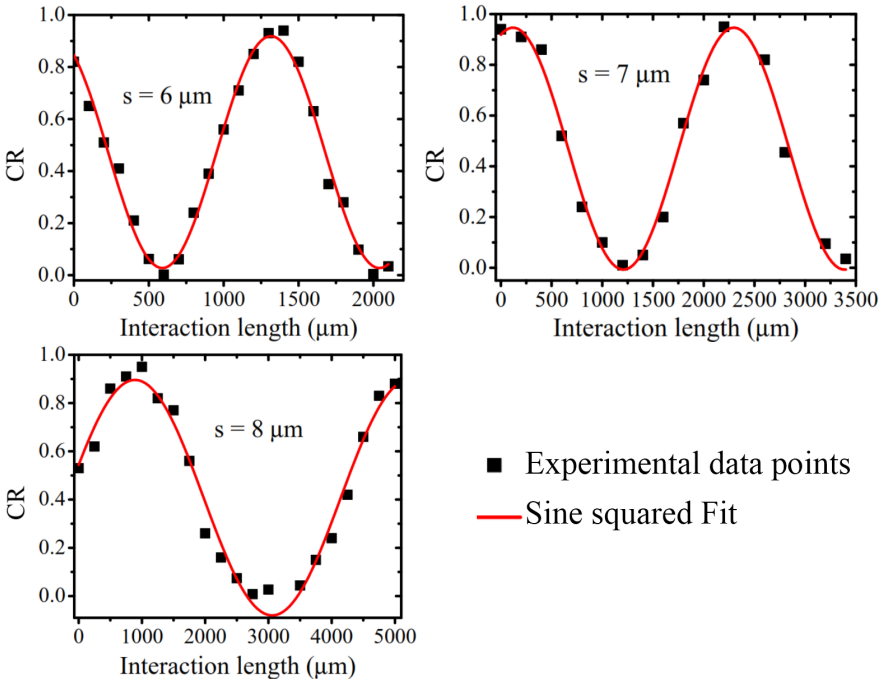

Fig. 4.8: Experimental data points of power coupling ratio as a function of the interaction length fitted to sine square functions for optical directional couplers inscribed in EAGLE2000 glass with core-to-core separations of $s = 6, 7, 8\ \mu$m.

standard deviation of the three data sets. It can be observed that the standard deviation is greater for CR within the range between 0.2 and 0.8 as well as for longer interaction lengths that can reach standard errors of $\pm$ 0.2. For the case of 3-dB directional couplers with an interaction length equal to 700 μm the standard deviation is about $\pm$ 0.1.

4.4 Optical non-deterministic polynomial problem solver in a laser-written waveguide platform

This section provides an example of a direct laser-written waveguide network in EAGLE2000 glass acting as an "oracle" for the solution of the Hamiltonian path problem. An introduction to non-polynomial complete problems followed by the proposal of using a laser-written optical

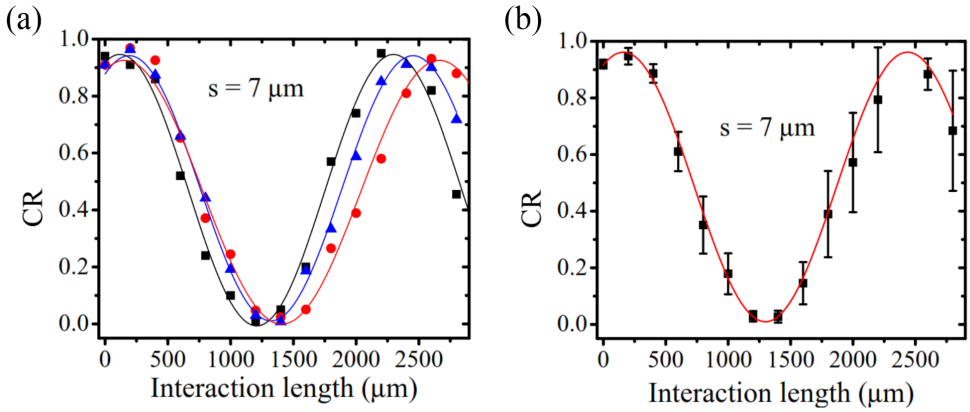

Fig. 4.9: (a) Reproducibility of power coupling ratios of optical directional couplers through three different experiments fitted into three sine square functions (indicated in three different colors). (b) Error bar graph of directional coupler fabrications via femtosecond laser writing. The black squares are the main values calculated from the three sets of experimental data points relative to the three experiments. The black bars indicate the standard deviation for each main calculated value. The red line is the fitted sine square function of the main calculated values.

oracle is detailed in this section. The work presented here has been published in [42].

In complexity theory, a NP complete problem (non-deterministic polynomial time complete problem) is a problem that requires exponential solving times since no polynomial-time algorithms are known for being solved on a non-deterministic Turing machine [148]. The time complexity of an algorithm defines the amount of time that the algorithm takes to be run and is a function of the input problem size (proportional to the number of nodes). There exist more than 2000 NP complete problems in our daily lives [149]. Some examples include the Clique problem, which requires finding the largest subset of people who all know each other in a social network [150], or the travelling salesman problem that looks for the shortest possible route that visits each city on a map exactly once [151]. Typically, a combinatorial graph problem with N nodes requires an execution time of 2^N times the clock time when solved through brute-force computing. For this particular time complexity function and a typical electronic computer clock speed of 3.6 GHz, a graph containing 10 nodes would require $\sim$300 nanoseconds to be solved, while it would take up to 10 years to obtain the exact solution for the case of a graph with 60 nodes.

In order to overcome the limitations that exponential time algorithms suffer, researchers seek more efficient methods for solving time demanding problems in reduced execution times. Flexible fabrication techniques offering down-scaling and integration of networks are beneficial for the investigation of new computing schemes. In the past decades, some alternative approaches to conventional combinatorics for a faster solution of NP complete problems have been proposed, including the use of soap bubbles [152], three dimensional microfluidic networks [153], protein folding [154,155], quantum [45,156–159] and DNA computing [160,161]. Optical computing has also been explored in different modalities due to the indisputable advantages that photonic devices might offer. Photonic approaches such as beam masking [151], free-space white light interference [162], time delay networks [144, 163] and cognitive photonics [164–166] have been proposed. Unfortunately, all these approaches demand exponentially increasing amount of physical resources as the problem size increases, leading to extremely large physical devices.

Particularly, time delay networks are an interesting approach due to their scalability in integrated photonic platforms. Within this modality, optical oracles that solve the Hamiltonian path problem have been proposed [163] and demonstrated in optical fiber networks [144]. An oracle is a "black box" that is able to generate a solution for any instance of a given decision making problem in a single operation. The potential of an optical computing scheme for an oracle allows speeding up execution times by parallel processing. However, one of the weaknesses of the time delay networks is the exponential increase of the physical network size with the number of nodes. For instance, in the case of an optical oracle for the study of the Hamiltonian path problem, the assignment of suitable delays for each node in the graph requires to avoid crossover of the optical signals within the network. For the general case of a graph with N nodes and arbitrary connections among different nodes, the optical delays between the nodes of the Hamiltonian path must satisfy the following relation:

$$\sum_{j=1}^{N} C_j T_j = \sum_{j=1}^{N} T_j \Longleftrightarrow C_1 = C_2 = \ldots = C_N = 1\,, \tag{4.2}$$

where C_j is a non-negative integer representing how many times node j has been visited, and N is the total number of nodes in the graph.

A possible delay assignment for the approach of a time delay network could be: $T_j = \Delta t \left(2^N - 2^{j-1}\right)$ with j = 1, 2, ..., N and Δt being the pulsewidth of the injected pulse. This formula was first

proposed by Oltean in [163] and was shown to generate a minimal set of optical delays (where the longest delay of the set is the smallest possible). This formula provides an efficient way to construct the network without knowing a priori whether the Hamiltonian path exists and it has already proved its validity in the solution of NP complete problems in the context of optical fiber networks [144] and DNA computers [167].

With the new advances in nanofabrication [168] and silicon photonics [169], a new interest in scalable photonic chips capable of solving hard computational problems has resurged in the last few years. Previous related work has shown a proof-of-concept demonstration of an optical fiber oracle, employed to find the existence of the Hamiltonian path within a graph by determining the time delay of propagating optical pulses [144]. For a 5-node graph, nanosecond optical pulses were used and the longest optical fiber length was 1.3 meters. Inspired by this work, an integration of this network is realized via the femtosecond laser writing technique, down-scaling the optical oracle network from meters to the centimeter scale and, correspondingly, from the nanosecond to the femtosecond optical time domain.

Here we demonstrate a femtosecond laser-written optical oracle based on cascaded directional couplers in borosilicate glass, for the solution of the Hamiltonian path problem. This work proves that graph theory problems may be easily implemented in integrated photonic networks, down scaling the net size and speeding up execution times.

4.4.1 Oracle chip design and fabrication

The design of the travelling salesman problem into the laser-written waveguide network was optimized in space in order to include as many nodes as possible into the network. Commercially available EAGLE2000 glass substrates with dimensions of $100 \times 100 \times 1$ mm^3 were used for the inscription of the NP problem. From the results presented in this chapter about waveguide fabrications in EAGLE2000 glass, the most optimum 3-dB directional couplers were found at a bend radius of $R = 40$ mm, a separation distance of $s = 7$ μm and an interaction length $L = 700$ μm. Considering that the axial length of a single 3-dB coupler is 9.52 mm and avoiding crossover

of optical signals in the femtosecond time scale, an optical waveguide network consisting of four directional couplers was the most optimum design feasible to fit along one dimension (100 mm length) of the glass substrate.

The topology of the laser-written optical network is depicted in Fig. 4.10. The photonic chip models a Hamiltonian path problem via a unidirectional graph containing four cascaded 2 $\times$ 2 directional couplers, where each coupler plays the role of a node (town), also acting as a beam splitter to direct the light to other nodes. The various nodes are connected to each other by waveguides (roads) with different lengths, introducing specific delays. Each waveguide connecting nodes is designated as d_{ij}, where i indicates the starting node, j indicates the ending node and i, $j = 1, 2, 3, 4$ with $i \neq j$. Considering the central waveguides as input and output ports, there are three possible paths that can be traveled by a single injected optical pulse: path A, path B and path C. d_{input} and d_{output} are the waveguides that connect the intput/output ports of the chip with the first/last node of the network with a length of 0.3 mm each. The tour followed along path A is: $d_{\text{input}} \rightarrow$ Node *1* $\rightarrow d_{12} \rightarrow$ Node *2* $\rightarrow d_{23} \rightarrow$ Node *3* $\rightarrow d_{34} \rightarrow$ Node *4* $\rightarrow d_{\text{output}}$. The route defined as path A corresponds to the Hamiltonian solution of the travelling salesman problem since it visits all the nodes exactly once. The route traveled by path B is: $d_{\text{input}} \rightarrow$ Node *1* $\rightarrow d_{13} \rightarrow$ Node *3* $\rightarrow$ d_{34} Node *4* $\rightarrow d_{\text{output}}$. And the tour folowed by path C is: $d_{\text{input}} \rightarrow$ Node 1 $\rightarrow d_{12} \rightarrow$ Node 2 $\rightarrow$ $d_{24} \rightarrow$ Node 4 $\rightarrow d_{\text{output}}$.

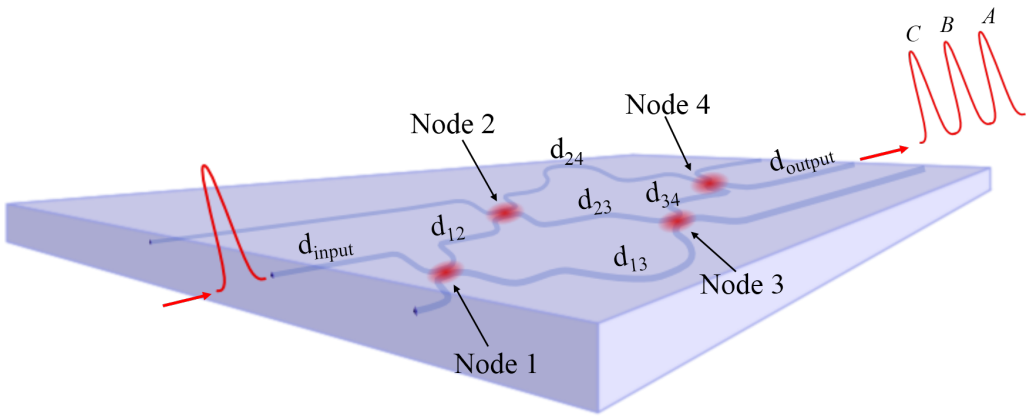

Fig. 4.10: Design of the ultrafast laser inscribed optical oracle. The laser integrated network mimics the topology of a network with four nodes, consisting of four 3-dB directional couplers.

To ensure unambiguous pulses arriving from the three possible optical paths, a suitable delay

selection for each node was performed corresponding to path lengths of 99.5 mm, 100.9 mm and 102.3 mm for path A, path B and path C, respectively. Table 4.1 shows the various segment lengths that make up each of the three paths in the optical oracle. If a single optical pulse is injected into the network from the central input port and assuming a waveguide refractive index of 1.5045, previously deducted from waveguide simulations in the waveguide characterization part of this chapter, the first optical pulse (pulse A) is expected to travel along path A and reach the network's output port after 165.8 ps, relative to propagation in free space. Under the same assumption, the expected arrival times of pulses B and C are 172.8 ps and 179.6 ps, respectively. The relative time delay between consecutive pulses is $\Delta t_{A\rightarrow B} = 7.0$ ps, $\Delta t_{B\rightarrow C} = 6.8$ ps, $\Delta t_{A\rightarrow C} = 13.8$ ps. To avoid crossover of optical pulses when interrogating the oracle, ultrashort optical pulses with pulse durations below $\sim$7 ps were required since the minimum relative time delay for pulses travelling along paths B and C is 6.8 ps.

Table 4.1: Designed waveguide (road) path lengths for the optical oracle chip.

	d_{12} (mm)	d_{13} (mm)	d_{23} (mm)	d_{24} (mm)	d_{34} (mm)	Total time (ps)
Path A	0.2	-	47.0	-	13.6	165.8
Path B	-	58.1	-	-	13.6	172.8
Path C	0.2	-	-	72.9	-	179.6

Two different optical oracle chips were laser fabricated. One of the oracle chips was intentionally fabricated with a gap of 20 μm along the waveguide d_{23}, eliminating the Hamiltonian solution since no connection between nodes 2 and 3 existed. After design and fabrication of the optical oracle chips, the devices were characterized through the fiber butt coupled method (chapter 3, section 3.3.2). The waveguides presented a propagation loss of 0.9 dB/cm and a total insertion loss of the entire optical oracle chip of 10.6 dB. The mode profiles of the guided modes of the three waveguides at the end facet of the sample were characterized via the mode profile characterization method detailed in chapter 3 (section 3.3.2) presenting MFD of 6.7×7.2 μm^2.

4.4.2 Experimental setup

Since the relative time delay between consecutive optical pulses travelling through the oracle chip are about 7 ps, the interrogation of the oracle chip required the use of ultrashort optical pulses with pulsewidths shorter than this value. The use of ultrashort optical pulses demands the usage of an ultrafast optical technique for the detection of the output pulses travelling through the oracle. An optical cross-correlation [143] was used to study the pulse distribution in time domain coming from the central output waveguide of the optical oracle chip by using a Ti:Sapphire femtosecond laser oscillator (Ti-Light) operating at a central wavelength of 800 nm and generating 170 fs pulses (FWHM) with 1 nJ pulse energy and 80 MHz repetition rate.

Fig. 4.11 depicts an scheme of the cross-correlator used to interrogate the oracle mimicking the travelling salesman problem. The output laser beam from the femtosecond oscillator was split into two separate beam paths by a beam splitter. 70% of the total output power was transmitted along the beam splitter and coupled into the optical oracle chip through a 0.16-NA focusing microscope objective. A 0.25-NA collimating objective lens was used to collect the output guided mode from the central waveguide at the end facet of the oracle chip. Optical spectra collected before and after the beam was coupled into the oracle chip confirmed that there was no noticeable self-phase modulation of the ultrashort pulses along the waveguides, which had a peak intensity of 10 GW/cm^2 when coupled into the oracle.

The remaining 30% of the light beam was reflected at the beam splitter and directed to a retroreflector placed over a motorized linear stage offering 2 μm resolution, with the ability to introduce optical delay to the beam. After this, the two beams were noncollinearly focused by a plano-convex lens with a $f = 75$ mm onto a 2 mm length BBO crystal cut at an angle of 30°. A second harmonic correlated signal due to the optical cross-correlation of pulses exiting the oracle chip could be generated after fulfillment of the phase-matching condition in the BBO crystal. A SCHOTT BG39 color glass filter was used to block the fundamental beams at 800 nm wavelength while an iris was used to remove the steady-state second harmonic signals. The resulting second harmonic cross-correlated signal was collected by a silicon photodiode detector, connected to a lock-in amplifier to discriminate the signal from the noise. The use of LabVIEW software allowed

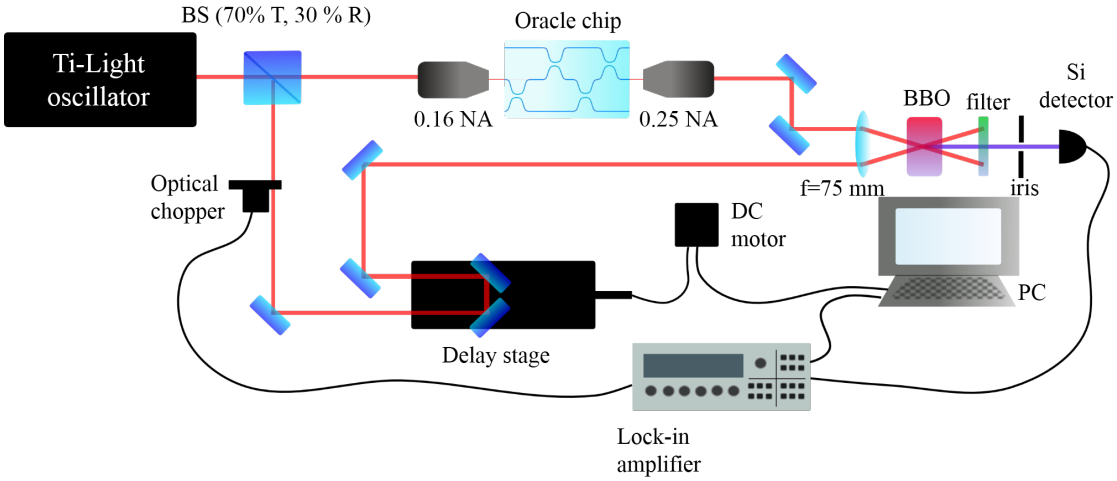

Fig. 4.11: Cross-correlation setup used to optically interrogate the optical oracle chip.

an integrated control of the linear motorized stage and lock-in amplifier in a single computerized program.

4.4.3 Results

The optical cross-correlation setup was used to interrogate two different oracle samples. One of the oracle samples contained the original design of the presented travelling salesman problem, including the Hamiltonian solution to the problem. The second oracle sample had the waveguide connecting nodes *2* and *3*, d_{23}, intentionally broken along a 20 μm gap. All the results obtained from the optical cross-correlation measurements were studied with respect to an absolute time zero defined by the autocorrelation signal detected in free space when the oracle chip was removed from the correlation setup.

The results obtained from the cross-correlation of the optical pulses coming from the two optical oracles are depicted in Fig. 4.12. The upper panel in Fig. 4.12 shows the autocorrelation signal of the Ti-Light femtosecond oscillator defining the absolute time zero. When interrogating the first optical oracle chip (*oracle chip 1*, central panel in Fig. 4.12) with femtosecond pulses, a spatial displacement of 24.45 mm of the linear motorized stage relative to the position in

which the free space autocorrelation was created led to the generation of the first cross-correlated output optical signal. This experimental displacement is equivalent to a time delay relative to the autocorrelation signal of $t = \frac{2\Delta x}{c} = 163$ ps, where Δx is the spatial displacement of the linear stage and c is the speed of light. The experimental relative arrival time of 163 ps is in good agreement with the expected theoretical value of 165.8 ps (Table 4.1), inferring that this pulse followed the route designated as path *A*. This optical pulse (pulse *A*) corresponds to the Hamiltonian solution of the travelling salesman problem since the optical pulse visits all the four nodes in the network exactly once.

The next pulse generated from the cross-correlation of *oracle chip 1* was obtained at a relative position of the linear stage with respect to the autocorrelation equal to 25.55 mm corresponding to a time delay of 170.3 ps, concluding that this optical pulse travelled all along path *B* (indicated as pulse *B*) since the calculated theoretical value is equal to 172.8 ps (Table 4.1). A third pulse was generated at a relative displacement of 26.66 mm, equivalent to a time delay with respect to the free space autocorrelation signal of 177.7 ps, concluding that it corresponds to a pulse that followed the route designated as path *C* in comparison with the expected theoretical value of 179.6 ps.

Table 4.2 shows a summary of the expected and the experimental arrival times of the optical signals generated from a cross-correlation of femtosecond pulses sent into optical *oracle chip 1* with respect to a theoretical and experimental free space autocorrelation signal. The small discrepancies between the theoretical and the experimental results are mostly due to a slight free space re-alignment needed to generate the second harmonic correlated signals when the oracle chip was introduced in the setup with respect to the generation of the free space autocorrelation signal. These time delay discrepancies correspond to spatial length discrepancies of 0.84 mm, 0.75 mm and 0.57 mm for pulses travelling along paths *A*, *B* and *C*, respectively. Considering the slight alignment required between different measurements, the experimental time delays are in extremely good agreement with the theoretical values. Hence, the three optical pulses generated from the cross-correlation of a single femtosecond pulse coupled into the first optical oracle chip represent the three possible paths that a single input pulse can travel along the optical network. The different relative intensities between pulses *A*, *B* and *C* are justified from a standard deviation of $\pm$ 0.1 for a power coupling ratio of 0.5 in each node of the network.

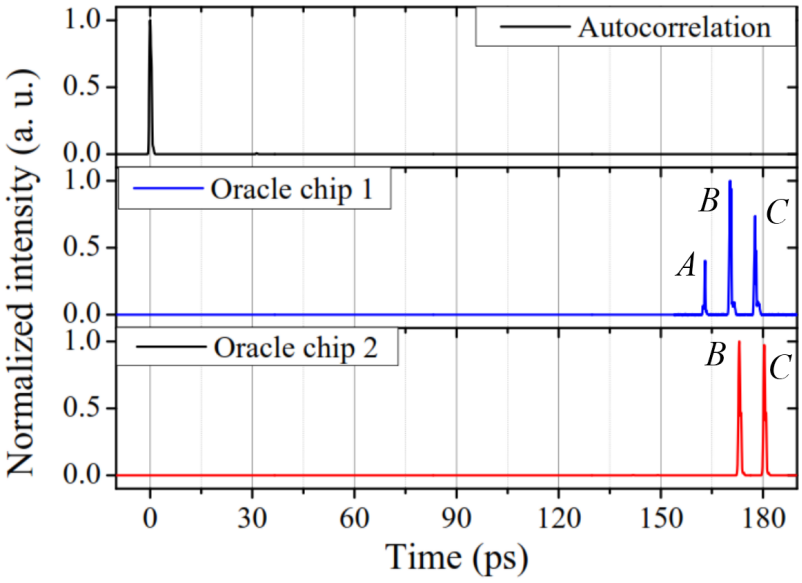

Fig. 4.12: Free space autocorrelation signal defining the absolute time zero (upper panel), cross-correlation of an input femtosecond pulse after travelling along the encoded optical oracle in chip 1 (centered panel) and cross-correlation of an input femtosecond pulse after being coupled into the encoded optical oracle in chip 2 (lower panel).

Table 4.2: Theoretical and experimental relative arrival times of correlated output pulses coming from *oracle chip 1* and their respective discrepancies.

	Expected time delay (ps)	Measured time delay (ps)	Discrepancy (ps)
Path *A*	165.8	163	2.8
Path *B*	172.8	170.3	2.5
Path *C*	179.6	177.7	1.9

The relative time delays between the three pulses generated from the cross-correlation of *oracle chip 1* have experimental values of $\Delta t_{A\to B} = 7.3$ ps, $\Delta t_{B\to C} = 7.3$ ps and $\Delta t_{A\to C} = 14.7$ ps. Table 4.3 shows the expected and the experimental time delays between pulses *A*, *B* and *C*, together with their discrepancies. The discrepancies between the expected and the experimental time delays are 0.3 ps, 0.5 ps and 0.9 ps between pulses *A*-*B*, *B*-*C* and *A*-*C*, respectively, corresponding to spatial distances of 0.09 mm, 0.15 mm and 0.27 mm, respectively. These discrepancies are notably low

and evince the reliability in the accuracy that ultrafast laser inscription technique provides.

Table 4.3: Theoretical and experimental relative time delays between the three pulses generated from the optical cross-correlation of *oracle chip 1*.

	Expected time delay (ps)	Measured time delay (ps)	Discrepancy (ps)
$\Delta t_{A\rightarrow B}$	7	7.3	0.3
$\Delta t_{B\rightarrow C}$	6.8	7.3	0.5
$\Delta t_{A\rightarrow C}$	13.8	14.7	0.9

The results from the cross-correlation obtained when interrogating the second sample (*oracle chip 2*), with a 20 μm gap along the waveguide d_{23}, are shown in the lower panel of Fig. 4.12. In this case, only two optical correlated pulses are generated after a single femtosecond pulse travels along the encoded oracle scheme. If a study of the relative arrival times is performed, the generation of the first pulse takes place at a relative position of the motorized stage of 25.95 mm, equivalent to a relative arrival time of 173.0 ps (optical path *B*). The next pulse is generated at the relative motorized stage position of 27.05 mm which is equivalent to a relative arrival time of 180.3 ps (optical path *C*). The relative delay between these two pulses is 7.3 ps, which replicates the experimental time delays previously obtained between consecutive pulses in the first optical oracle chip. The lack of a third pulse with shorter arrival time reveals the absence of a Hamiltonian solution in this second encoded sample (*oracle chip 2*), which only generates two correlated pulses at arrival times equivalent to optical paths *B* and *C*.

Summarizing the results, the presence of a Hamiltonian solution for the travelling salesman problem has been inferred from the interrogation of two optical oracles via an optical cross-correlation technique. This method provides all the possible encrypted solutions in the chips via a single operation.

4.5 Summary

Briefly, this chapter has presented the optimization of processing parameters to directly laser inscribe waveguides within the bulk of a borosilicate glass substrate (Corning EAGLE2000). Single mode waveguides at 800 nm wavelength were fabricated for their convenient compatibility and relevant applications with laser sources such as Ti:Sapphire oscillators and single photon emitters by SPDC. Borosilicate glass was chosen as a host platform for waveguide fabrication since it is a well-known material in ultrafast laser processing of waveguides with a wide transparency window covering wavelengths from 360 nm onwards. The use of high repetition rates during waveguide fabrication enabled high quality waveguides with nearly circular guided modes with a MFD = 6.5 $\times$ 7.1 μm^2 and insertion losses of 5.2 dB at 800 nm wavelength. A study of the pulse broadening effect of femtosecond pulses travelling along the waveguides has been also investigated concluding that waveguide dispersion is relatively low and therefore negligible for optical circuits probed with ultrashort pulses.

An optimum processing window for waveguides with double S-bend geometries and directional couplers has been detailed and compared with R-soft BeamPROP software simulations in order to find the most optimum 3-dB directional couplers to be included as part of the main building block of future optical networks. As well, the reproducibility of the ultrafast laser inscription technique has been tested for a range of directional couplers containing different lengths, resulting in a good performance for directional couplers with shorter interaction lengths and with power coupling ratios between 20% and 80%.

In the last part of the chapter, the Hamiltonian path solution of the travelling salesman problem has been implemented in a compact optical oracle chip by direct laser writing of a coupled optical waveguide network. One of the novelties of this approach has been solving the encrypted mathematical question within the optical glass chip by making use of an optical cross-correlation. Thus, two different oracle chips have been optically interrogated by sending femtosecond laser pulses into the waveguide network that maps the topology of a graph with four nodes (or towns). By measuring the time delay between the output pulses from the laser encrypted oracle, it has been possible to induce the presence of a Hamiltonian solution, whose delay equals the sum of the travel

times needed to visit all the nodes of the network, which is made unique by design. This work has enabled down-scaling of photonic schemes from previous work developed in optical fibers [144], allowing to move from meters of optical fiber towards the millimeter length scale in device integration and, thus, requiring to move from the nanosecond towards the femtosecond time scale for the solution of the optical encoded problem. Along with this decrease in the physical device size and the reduction of the optical pulse width, shorter execution times of the NP computational problems are feasible through this technique. This first demonstration of a laser-written optical oracle on a robust integrated optics platform proves the potential for reducing the solving time of computationally hard combinatorial problems exploiting the parallelism of light propagation in downscaled optical networks. By exploiting the three-dimensional patterning and the parallel processing offered by ultrafast laser writing, future designs up to $\sim$20 nodes could be implemented within a $100 \times 100 \times 1$ mm^3 glass substrates distributed in two different layers containing 10 nodes each and connected by a curved optical waveguide that inverts the direction of light propagation towards the second layer. Assuming single point detection at the output of the network, this oracle's decision time, which would be only limited by parallel pulse propagation time within the network, would require 1 ± 0.03 ns in comparison with the $\sim$6 μs needed for an electronic computer to find the combinatorial solution considering only a two-directional-node network and a clock speed of 3.6 GHz.

Chapter 5

Direct laser inscription of waveguides in gallium lanthanum sulfide glass

This chapter covers the fabrication and characterization of ultrafast laser inscribed waveguides, S-bends and directional couplers in the bulk of gallium lanthanum sulfide (GLS) glass. An optimum processing window for single mode guiding at 800 nm wavelength has been reported for the first time. The selected wavelength offers the possibility of having optical circuits compatible with Ti:Sapphire technologies for the use of highly nonlinear optical circuits and with spontaneous parametric down-conversion (SPDC) light sources for usage in the quantum regime. Directional couplers have been characterized as ultrafast all-optical switches by exploiting the high Kerr nonlinearity displayed in GLS glass. The nonlinear effect of femtosecond laser writing in the bulk of GLS has been inferred by the estimation of the nonlinear refractive index of the waveguides from the optical switching parameters of a directional coupler. The fabrication and characterization results presented in this chapter have been published in [139], together with μ-Raman and X-ray microanalysis (EDX) waveguide microanalysis to elucidate the origin of the laser-induced refractive index change in GLS. The last part of this chapter presents the fabricated laser inscribed waveguides in GLS as an approach for a neuromorphic platform. This approach is based on the work presented by Gholipur et al. in [166] where GLSO fibers are proposed as a "synaptic" photonic material. The search for devices based on the inherent capabilities of the human brain

is a re-emerging field since the last few years which expects to offer computational devices with an improved power efficiency and faster computation times due to a unique colocalized memory-computation structure. Within this context, ultrafast laser written waveguides in GLS are explored as a possible cognitive photonic platform including a series of features that mimick biological functions. The work performed here shows the potential of femtosecond laser writing in terms of compactness, offering the possiblity to laser write photonic networks in three dimensions in comparison with previous work performed in optical fibers [166] or silicon photonics [170].

5.1 Ultrafast laser inscription of waveguides in gallium lanthanum sulfide glass

Nonlinear optical processes gained increasing attention in the past decade as the basis for innovative technologies in optics and photonics and in particular for all-optical signal processing [171]. The highly nonlinear properties of chalcogenide glasses, i.e. glasses made of one or more chalcogen elements (O, S, Se, Te, Po) and network formers (such as As, Ge, Sb, Ga, Si or P), have attracted great interest as a nonlinear photonics platform. These glasses offer a high linear and nonlinear refractive indices, a wide transparency window up to the infrared region of the spectrum, a low maximum phonon energy and a nonlinear response in time within the femtosecond regime [52]. Among the chalcogenides commercially available, gallium lanthanum sulfide (GLS) has the highest nonlinear figure of merit (FOM) [140], being thermally stable up to 550°C and not presenting toxicity related issues as other commonly used chalcogenide glasses such as As_2Se_3.

Some of the approaches available for creating optical circuits in chalcogenide glasses are in the form of thin films, microspheres or optical fibers [3]. Of particular interest is the fabrication of optical waveguides and other components via femtosecond laser inscription, relying on the nonlinear absorption of ultrashort laser pulses focused in the bulk of the material. Unlike planar silica [172] and silicon technologies [173], laser writing is a versatile technique which allows the formation of waveguides in the bulk of a wide variety of dielectrics [1, 16, 69, 73] in three dimensional geometries.

Previous work developed via ultrafast laser inscription in GLS glass has demonstrated waveguides with low propagation losses of 1.5 dB/cm at 633 nm wavelength [47] and 0.65 dB/cm at 1560 nm wavelength [49]. Moreover, femtosecond laser inscribed mid-IR photonic circuits for astronomical applications were reported with $\sim$1 dB/cm propagation loss at 3.39 μm wavelength [174,175]. Here, the goal is to design waveguides operating at 800 nm since no laser-written photonic circuits hosted in GLS have been previously reported at this convenient wavelength. The desired waveguides should display single mode guidance at 800 nm wavelength, compatible with Ti:Sapphire technologies for ultrafast nonlinear switching applications [176] and single photon sources by SPDC for quantum information processing [177].

Gallium Lanthanum Sulfide is considered an exotic glass presenting a challenge for the laser inscription of symmetrically-shaped photonic structures in its bulk. The two main characteristics that make of it a challenging material for laser processing are its high linear ($n_0 = 2.4$) and nonlinear ($n_2 = 2.16\times10^{-14}$ cm^2/W) refractive indices. As a consequence of the large linear and nonlinear refractive index values, the critical power for self-focusing propagation of light [135] in GLS is two orders of magnitude less than in fused silica (see table 5.1).

Table 5.1: Comparison between critical power and energy for self-focusing of light in GLS and fused silica glasses during femtosecond laser pulse irradiation [3, 6].

Property (λ = 1030 nm)	**GLS**	**Fused silica**
n_0	2.4	1.45
n_2	2.2×10^{-14} (cm^2/W)	2.6×10^{-16} (cm^2/W)
$P_c = \frac{3.77\lambda^2}{8\pi n_0 n_2}$	30 kW	4 MW
E_c (for 300 fs pulses)	9 nJ	1.2 μJ

A high linear refractive index results in large spherical aberration during femtosecond laser inscription, whereas a high nonlinear refractive index causes self-focusing of light along the path travelled by the incident laser beam (see chapter 2, section 2.1.3). To reduce these detrimental effects, which would cause severe vertical elongation of waveguide cross section, a multiscan shaping modality [73] was chosen for waveguide fabrications (Fig. 5.1). This multiscan modality consists of several single laser scans at low pulse energies overlapping transversally to the wave-

guide writing direction. The multiscan approach allowed to construct a nearly squared shaped positive step-index cores of the waveguide cross section at lower pulse energies. Fabrications at lower pulse energies enabled gentler modifications at the focal volume of the material and resulted in smoother and more symmetric waveguides with minor insertion losses, in comparison with the single scan technique.

The micromachining workstation described in chapter 3, section 3.1, was used to laser write straight waveguides, S-bends and directional couplers in the bulk of GLS glass. The general fabrication conditions chosen from the machining system were a fundamental wavelength of 1030 nm, enabling nonlinear multiphoton absorption, 300 fs pulse duration and 500 kHz repetition rate. The laser beam was focused into the bulk of GLS glass using a 0.42 NA microscope objective, resulting in a diffraction-limited minimum waist radius, ω_0, of 0.8 μm and a Rayleigh range at the laser focal spot, z_0, of 4.5 μm (see equations 2.5 and 2.6 in chapter 2).

Seeking optimal processing conditions, straight waveguide fabrications were performed for a wide range of powers and scan speeds. Incident laser powers ranging from 10 to 250 mW, corresponding to pulse energies between 20 nJ to 500 nJ were used, in steps of 5 mW. The fabrications were done using translation speeds between 2.5 mm/s and 50 mm/s, in steps of 5 mm/s. The multiscan parameters chosen for an optimal processing window consisted of 9, 13 and 18 scans per line with a separation of 0.3 μm. Each multiscan line was transversally applied with respect to the longitudinal orientation of the resulting waveguide and the polarization was perpendicular to the scan direction (Fig. 5.1). Waveguide inscriptions were performed at a depth of 150 μm below the glass surface.

The morphology of the laser-inscribed photonic structures was characterized under an optical microscope in transmission mode using 10$\times$ and 40$\times$ magnification objectives (Eclipse ME600, Nikon). For waveguide loss measurements, the chip to fiber butt coupled method explained in chapter 3 (section 3.3.2) was employed. The near-field waveguide mode was measured using a 60$\times$ aspheric lens (5721-H-B, Newport) to image the guided mode onto a beam profiler (SP620U, Spiricon).

All the waveguide results shown hereafter correspond to a processing multiscan parameter of

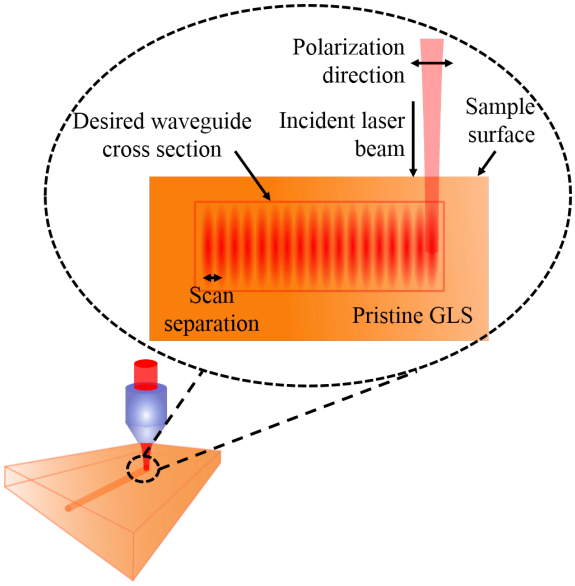

Fig. 5.1: Sketch of the multiscan shaping modality in the bulk of GLS glass. The incident light is perpendicularly polarized to the scanning direction. The multiscan lines are transversal to the longitudinal direction of the resulting waveguide. The modified region in a single line is composed of several scans, each of them irradiated at a certain separation distance and giving form to the final shape of the laser written waveguide.

18 scans per line with a separation distance of 0.3 μm, which allowed for the best compromise between CL and α while mantaining single mode behavior. The writing parameter that had the greatest impact in waveguide fabrications was the pulse energy. The effect of the pulse energy during femtosecond laser irradiation in the bulk of GLS glass can be observed from a preliminary characterization of the optical microscope images in Fig. 5.2. For incident pulse energies lower than 50 nJ, no visible signs of laser modification were observed. Generally, pulse energies between 50 nJ to 60 nJ led to weak modifications of the substrate at the focal volume, resulting in waveguides with high insertion losses ($>$ 7 dB) as a consequence of the small refractive index change achieved. When the pulse energies are further increased up to 100 nJ, the modifications at the focal volume are better defined and brighter cross sections with rectangular shapes are formed. Generally, a processing window in pulse energies ranging from 50 nJ to 100 nJ resulted in symmetrically-shaped single mode guiding structures. Fabrication pulse energies above 100 nJ led to a non uniform and higher Δn with waveguides having multimode behavior and guiding in different regions. For pulse energies above 200 nJ, cross sections with typical teardrop shapes are

formed due to the higher field irradiances within the bulk of the substrate. As the pulse energy keeps rising above 300 nJ, the teardrop cross sections increase in size and undesired optical damage along the incident laser beam path leads to surface ablation until the substrate, eventually, gets fractured.

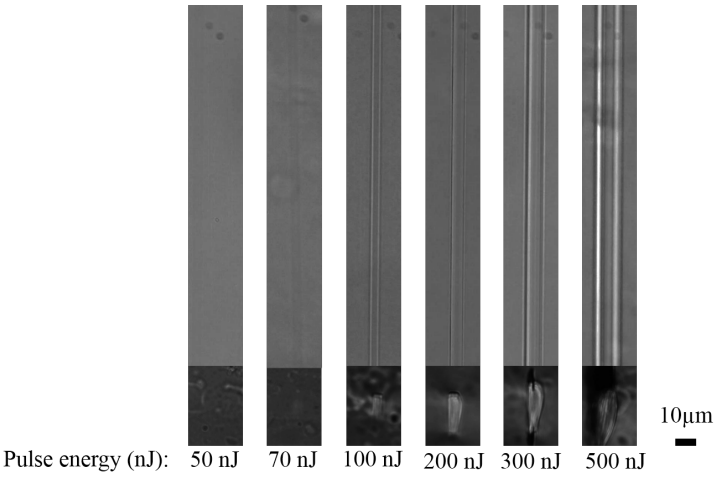

Fig. 5.2: Effect of pulse energy during femtosecond laser inscription of waveguides in GLS glass from top (microscope images at the top of the figure) and side views (microscope images at the bottom of the figure) for a fixed scan speed of 20 mm/s.

A graph describing the trend of the waveguide cross-section area as a function of the pulse energy is shown in 5.3.

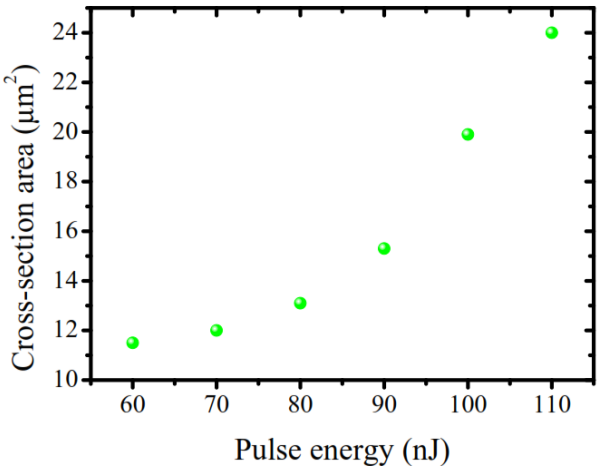

Fig. 5.3: Growing trend of the waveguide cross section area with increasing the pulse energy.

The general trend of varying the scan speed during ultrafast laser inscription of waveguides can be also observed in Fig. 5.4. At high scan speeds, the number of pulses overlapping is smaller, resulting in smaller modifications and in lower Δn. Smaller modified volumes lead to smaller cross sections, producing single mode waveguides. When moving towards lower scan speeds, a large number of pulses overlapping within the focal volume results in stronger modifications which result in more contrasted and larger cross sections. In some cases, the use of low translation speeds ($\leq$3 mm/s) led to waveguides operating at the multimode regime.

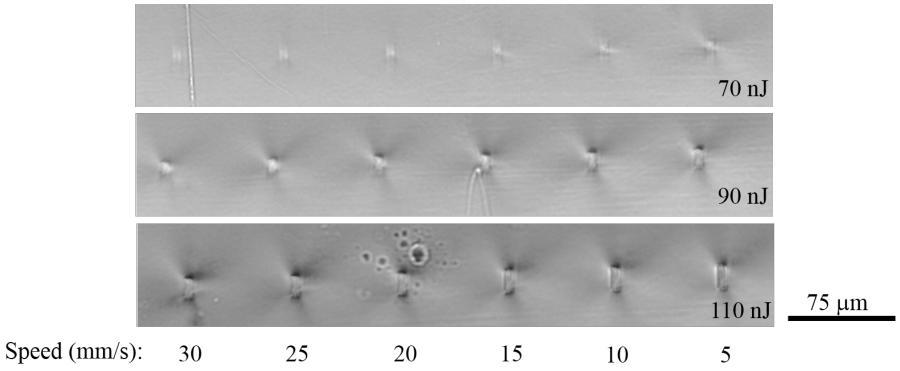

Fig. 5.4: General trend in the formation of waveguide cross section with varying translation speeds during femtosecond laser writing in GLS glass for three different sets of waveguides written at the pulse energies of 70 nJ, 90 nJ and 110 nJ pulse, respectively.

The general trend for a combined effect of pulse energy and scan speed during waveguide fabrication is shown in Fig. 5.5. Low insertion loss waveguides are found for a narrow 60-80 nJ range of pulse energies and for a broad processing window of scan speeds within the range of 2.5 mm/s to 10 mm/s. This processing window leads to the best waveguides with insertion losses below 6 dB (indicated by the green spots). When moving towards lower pulse energies but higher scan speeds, the guides present large insertion losses, whereas moving towards higher pulse energies but lower translation speeds results in large waveguide cross sections with multimode guiding.

A reasonable balance between pulse energy and translation speed led to the optimal waveguide, obtained at 70 nJ and at 5 mm/s. Fig. 5.6 shows the longitudinal and transverse views of the waveguide under white-light microscopy. The rectangular shape of the cross section is due to the employed multiscan approach. The resulting waveguide has a mode field diameter (MFD) of 7.5

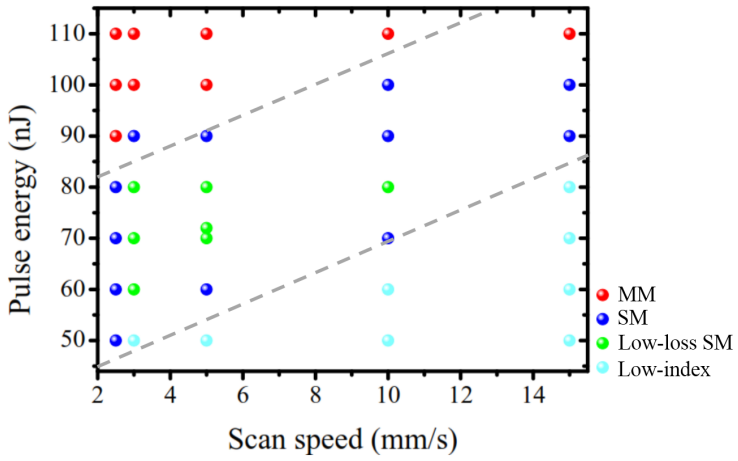

Fig. 5.5: Waveguide characteristics as a function of pulse energy and scan speed in GLS glass. The green spots indicate single mode waveguides with insertion losses below 6 dB.

μm [139]. The measured insertion loss was 2.0 dB, with an estimated coupling loss of 0.7 dB/facet obtained from the overlap integral between the waveguide and the fiber guiding modes. After accounting for a Fresnel reflection loss of 0.2 dB/facet, the propagation loss was $\sim$0.1 dB/cm. An estimation of the refractive index change, deduced from the assumption of a refractive index step profile and a measured MFD of 7.5 μm, was inferred to be of $\Delta n = 10^{-3}$ using a commercial mode solver (Lumerical MODE Solutions). In contrast with the single scan technique, the multiscan approach induces gentler material modifications as a result of the low pulse energies employed. In addition, the refractive index profile is more uniform, as several scans at low energy are used to build up the waveguide cross section. Larger pulse energies used during the single scan technique lead to refractive index profiles with more complex distributions [47].

5.2 Ultrafast laser inscription of directional couplers

With the aim of characterizing the optical nonlinear switching behaviour of GLS glass, directional couplers were fabricated in the bulk of GLS via femtosecond laser writing technique. Since each arm of a directional coupler is composed of a double S-bend waveguide, double S-bends were

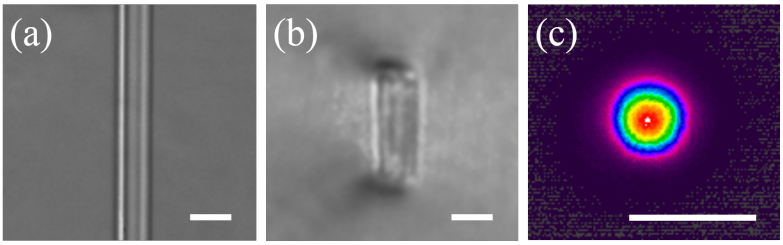

Fig. 5.6: (a) Overhead microscope view of the most optimum femtosecond laser formed waveguide in GLS glass. (b) Cross-sectional microscope view of the best waveguide. (c) Gaussian transmitted mode at 800 nm with a MFD = 7.5 μm. The scale bars indicate 10 μm.

formed prior to directional coupler fabrications in order to study the bend losses contributing to the waveguide.

Waveguides with double S-bend shapes were formed at 150 μm below the glass surface and for a scan speed of 5 mm/s. Incident laser powers $P = 45$ and 55 mW, corresponding in pulse energy to 90 and 110 nJ, were chosen with radii of curvature (R) ranging from 30-70 mm in steps of 10 mm. To find an optimum radius of curvature, a study of bend losses with varying bend radii in laser inscribed S-bend waveguides was performed. The bend loss corresponds to the additional insertion loss in a single arm of a double S-bend waveguide (single arm of a directional coupler) compared to a straight waveguide. Therefore, this loss includes pure bend loss from the four arcs and transition loss from the six points where there is an abrupt change in curvature. The bend loss was calculated by subtracting the insertion loss of a straight waveguide, fabricated under the same irradiation conditions, from the insertion losses inserted by the two double S-bends [6].

Fig. 5.7 shows the general trend of the bend loss as a function of the bend radius. Larger radii of curvature result in lower losses, but simultaneously lead to longer axial lengths of the laser formed S-bends. Hence, the overall size of the chip, defined as the axial footprint of a directional coupler with zero interaction length, increases for larger bend radii. A reasonable compromise between bend losses and chip size was obtained for a radius of curvature of 45 mm, which was selected for the directional coupler design.

With an optimum bend radius chosen from a careful characterization of S-bends, directional

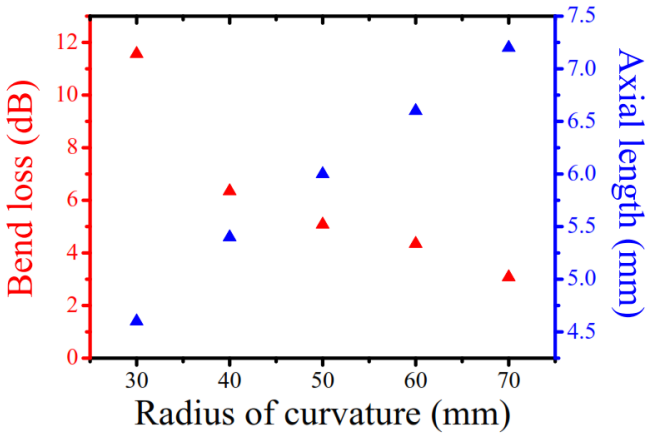

Fig. 5.7: Bend loss and axial size of double S-bend waveguides inscribed in GLS glass as a function of the bend radius.

coupler fabrications were performed. The coupler structures were written at 150 μm below the sample surface and at a translation speed of 5 mm/s. The input-to-input port distance was fixed at $p = 100$ μm. Keeping all these parameters constant, the incident laser powers chosen belonged to a range between $P =$ 36-55 mW. The core-to-core separation distances at the interaction region between the two arms of the directional coupler were varied from $s =$ 5.4-8 μm. The number of scans performed in a single line for directional coupler fabrications was 18 scans, with a constant separation of 0.3 μm.

The laser written directional couplers were characterized by launching light at 800 nm wavelength into one of the arms of the directional coupler and measuring the output power at the cross and through output ports. The power coupling ratio is calculated as

$$\mathrm{CR} = \frac{P_{\mathrm{cross}}}{P_{\mathrm{bar}} + P_{\mathrm{cross}}}, \tag{5.1}$$

and it varies with interaction length. The trend of the power coupling ratio of directional couplers written at a pulse energy of 72 nJ with a separation distance of 7 μm is shown in Fig. 5.8. The plot is fitted to a sine square function according to the equation $\mathrm{CR} = \sin^2\left(\frac{\pi}{l_B(\lambda)}L\right)$, where l_B is the beat length, which is the length necessary for a full power coupling ratio oscillation, λ is the operating wavelength and L corresponds to the interaction length (see chapter 2, section 2.2.2). The peak coupling ratio for directional couplers is $\sim$55%, notably lower than the value of 100% achieved in borosilicate glasses [147].

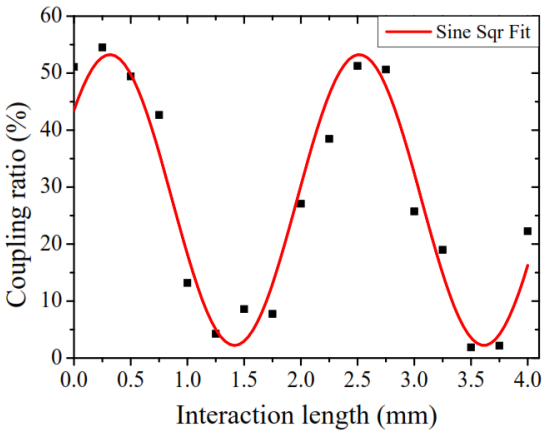

Fig. 5.8: Coupling ratio as a function of the interaction length at 800 nm wavelength for directional couplers written at 18 scans per line, 72 nJ pulse energy, 5 mm/s scan speed and 7 μm core-to-core separation distance.

The low peak coupling ratio can be attributed to the different propagation constants relative to the two waveguides forming the arms of the directional couplers [178]. In the course of the inscription of the second waveguide, the characteristics of the first waveguide in a directional coupler may be altered due to the small core-to-core separation distance of 7 μm. One other explanation for the differing propagation constant is the multiscan approach used for fabrications which relies on lower pulse energies during waveguide formation without triggering heat accumulation. This implies that waveguides are more sensitive to fabrication fluctuations in comparison with waveguides formed in the less fabrication sensitive cumulative heating process during the application of the single scan technique [178].

In order to achieve larger coupling ratios in directional couplers in the bulk of GLS glass, a possible solution is to create directional couplers with core-to-core separation distances larger than $\sim$15 μm [179]. In [179], an increase in the separation distance from $s = 7.5$ μm to $s = 15$ μm in directional coupler written in GLS substrates showed an increase in the peak coupling ratio of $\sim$10%. One of the main disadvantages of this solution is the notable decrease in the coupling coefficient of the directional coupler due to the large separation distance, requiring long interaction lengths of the order of millimiters in order to obtain the maximum amount of light transferred to the cross waveguide. This would have a notable impact on the manufactured chip size, where one of the main practical uses of having optical circuits in the bulk of highly nonlinear glasses

is the shorter lengths required to have nonlinear phase shifts compared to circuits hosted in more convential fused silica based glasses.

Further optimization of the directional coupler design was achieved by lowering the number of scans per line during directional coupler fabrication to 13 scans per line, keeping the rest of the processing parameters unaltered. After the fabrication, optical microscope images showed a modification width of 5 μm for directional couplers with 13 scans per line, in contrast with a modification width of 5.8 μm observed in directional couplers with 18 scans per line.

Fig. 5.9 shows the results obtained for the directional couplers fabricated at 13 scans per line. The plot is fitted to a sine square function as in the previous figure, following the theoretical formula. The peak coupling ratio achieved in this case is 65%. The increased peak coupling ratio is attributed to the fewer scans used to fabricate the coupler, reducing the sensitivity to laser power fluctuations. In aditiion, the large edge-to-ege separation in the case of 13 scans results in an increase of $\sim$10% of the peak coupling ratio.

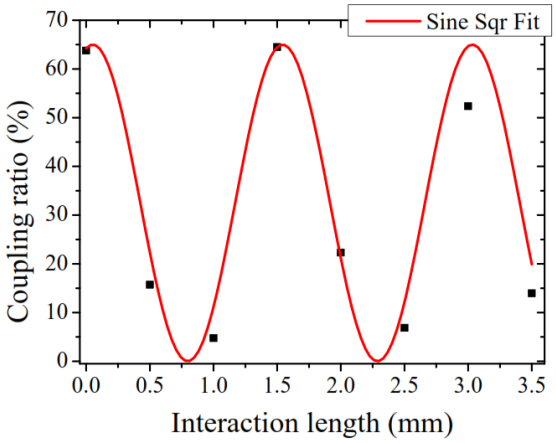

Fig. 5.9: Cross to bar light coupling ratio as a function of the interaction length at 800 nm wavelength for directional couplers written at 13 scans per line, 72 nJ pulse energy, 5 mm/s scan speed and 7 μm core-to-core separation distance.

5.3 Directional couplers as ultrafast all-optical switches

An optical switch is a device that enables, selectively, to switch on and off optical signals or allows to redirect an optical signal from one channel to another. Optical switching is driven by the need of providing flexibility in connectivity between optical networks. When the control of the switch is performed via an optical signal, in the absence of any mechanical, electrical or magnetic signal, then the device is an all-optical switch. Despite the good performance of current electronic switching devices [180], the growing need for developing switches already working with light, operating at faster speeds and offering higher bandwidths can be especially profitable. All these possible benefits lead to exploit the potential characteristics that optical devices offer [176].

In the search for novel switching materials, chalcogenide glasses are suitable candidates as nonlinear media presenting high third order nonlinearities and low multiphoton absorption coefficients [181], allowing the interaction between two or more light beams. Specifically for an all-optical switching device, the control of light by using light becomes essential. Here, the nonlinear directional couplers inscribed in GLS glass act as ultrafast all-optical switching devices due to the power control of a unique input signal. The foundation of the all-optical switching relies on the refractive index change of the material, induced by the nonlinear Kerr effect. The optical Kerr effect is the effect of an instantaneously ocurring nonlinear response when an intense electromagnetic field is applied in a medium and, specifically, is directly related to the nonlinear optical susceptibility of the medium. The optical Kerr effect can be described as a modification of the refractive index of the nonlinear medium due to the high optical intensity applied. Therefore, all-optical switching is manifested as an intensity dependent refractive index change induced in the nonlinear material [182]:

$$n = n_0 + n_2 I\,, \tag{5.2}$$

where n_0 corresponds to the linear refractive index, n_2 is the nonlinear refractive index and I is the intensity of the control light.

The design of the directional couplers is made in such a way that, when a low irradiance light is launched into the bar input port, a maximum optical power is transferred to the cross waveguide output through evanescent coupling along the interaction region between the two waveguides. In

order to have such a large amount of light being transferred to the cross waveguide, the interaction length of the directional coupler must be equal to a half beat length. As the input irradiance continues rising, the overall refractive index of the bar waveguide starts increasing. For a sufficient input power, a required overall refractive index change in the bar waveguide is eventually reached and all-optical switching will be achieved. This increase of the refractive index causes a change in the propagation constant, β_1, of the bar waveguide and induces a mismatch between the two propagating modes along the two waveguides. As a result of this mismatch, the cross to bar coupling ratio diminishes, as it can be seen from Eq. 2.30.

A single beam experiment was carried out (Fig. 5.10). The optical source used in this setup was a home-built amplified Ti:Sapphire laser offering a centered operating wavelength of 800 nm, with a repetition rate of 2 kHz and 180 fs pulsewidth. The laser beam from the home-built amplified system was coupled into one of the input ports of the directional coupler using a 0.16-NA anti-reflection coated objective lens. Both guided modes of the directional coupler were collected by a 0.25-NA AR coated objective lens at the end facet of the sample. A Si CCD camera (SP620U, Spiricon) was used to image the collected output modes and to detect the optical powers of both outputs. A Si photodetector placed ahead of the 0.16-NA focusing objective lens was used for power detection of the incoming light into the input port of the directional coupler. The input optical irradiances for the optical switching measurements were selected using different combinations of ND filters placed before the focusing lens.

The selected directional coupler was fabricated at 18 scans per line, at a pulse energy of 72 nJ and at a scan speed of 5 mm/s, having a bend radius $R = 45$ mm, an interaction length $L = 250$ μm and a separation distance $s = 7$ μm. The directional coupler selected had a power coupling ratio of $\sim$55% within the linear regime (Fig. 5.8), being possible to be operated as an all-optical switch. The results of this measurement are shown in Fig. 5.11, where the relative transmission along the bar and cross output waveguide ports is variable with the input irradiance.

As can be seen from the plot in Fig. 5.11, the output cross and bar relative transmission of the selected directional coupler, indicated as stars, was measured with a CW diode laser source at 800 nm wavelength, prior to the switching characterization experiment. This prevents the presence of any nonlinearities during light propagation along the directional coupler at the low irradiance

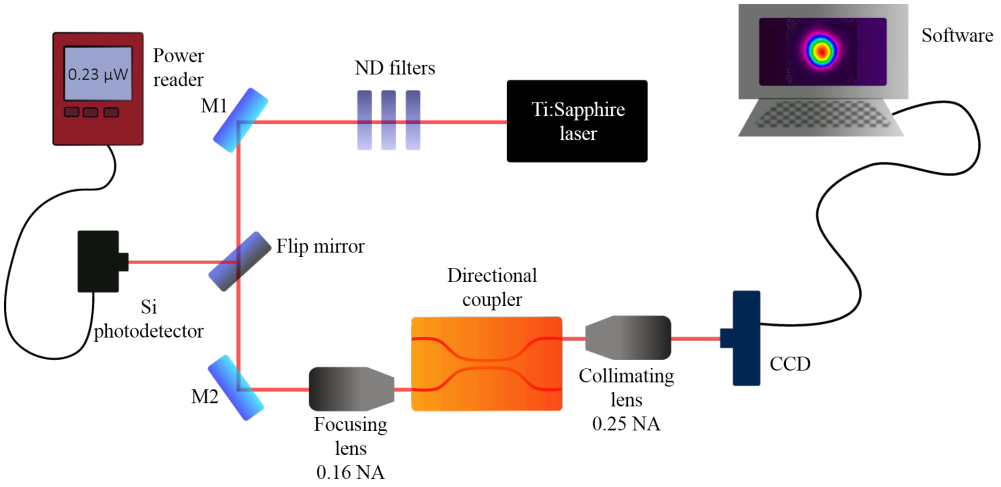

Fig. 5.10: Experimental setup for the nonlinear characterization of directional couplers in GLS glass as all-optical switches.

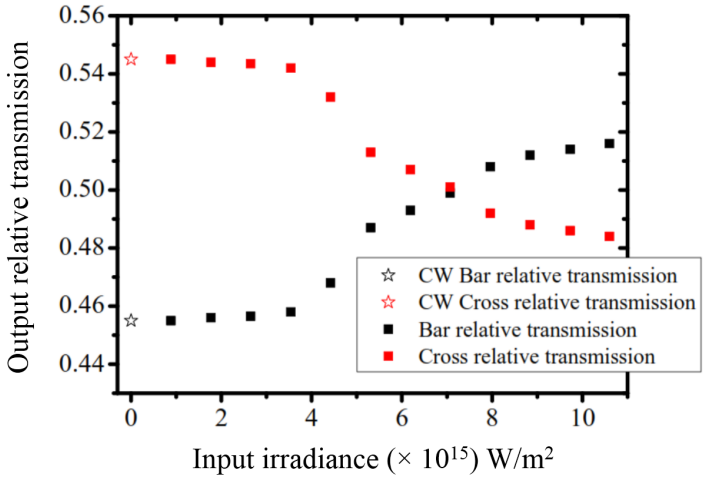

Fig. 5.11: Output cross and bar relative transmissions as a function of the input irradiance in a laser inscribed directional coupler within the bulk of GLS glass.

regime before any switching could take place. At this low input irradiance, the medium operates within the linear regime and light experiences its maximum evanescent coupling towards the cross waveguide, reaching a power coupling ratio of ∼55%. When the input irradiance increases, the medium responds within the nonlinear regime as a consequence of the high third order nonlinear polarizability of the sulfide ion present in GLS glass [3], meaning that the refractive index of the bar waveguide increases. As a result of this intensity dependent refractive index change, the

propagation constant of the bar waveguide changes, altering the cross to bar transmission ratio. An equal output cross and bar relative transmission occurs at the input irradiance of 7.1×10^{15} W/m^2. As the input irradiance keeps gradually increasing, the cross to bar coupling ratio is reversed from 55% to 48 % when the required overall refractive index change of the bar waveguide is reached (as shown in Eq. 1.1). The input irradiance required to completely switch the transmitted light from the cross to the bar waveguide is 7.8×10^{15} W/m^2.

The optical switching effect was observed to be a reversible process since the cross and bar output relative transmissions could be replicated by lowering the input irradiances to the previous values used. The fact that the directional coupler works as an all-optical switch within a reversible operating range suggests that no permanent optical damage or material modification is achieved.

5.4 Deduction of the nonlinear refractive index of laser inscribed waveguides in the bulk of gallium lanthanum sulfide glass

In order to elucidate the effect on the nonlinear properties produced by the laser writing technique during inscription of optical circuits, the nonlinear refractive index of the laser inscribed waveguides was retrieved from the optical switching parameters of a directional coupler.

The nonlinear phase shift responsible for optical switching is induced by a nonlinear refraction and is given by [182]:

$$\Delta\phi = \frac{2\pi L n_2 I}{\lambda}, \tag{5.3}$$

where L is the interaction length of the directional coupler, n_2 is the nonlinear refractive index, I is the irradiance and λ is the operating wavelength.

The light-induced nonlinear phase shift of an all-optical switching device is proportional to $m\pi$, where $0 < m < 4$, depending on the specific device [183]. For the case of optical directional

couplers, the nonlinear phase shift caused by nonlinear refraction is of the order of 4π [184]. Taking into account that the input irradiance necessary to completely switch the optical power from the cross to the bar waveguide of the directional coupler used in Fig. 1.11 is $\sim 7.8 \times 10^{15}$ W/m^2, and accounting a Fresnel loss of 0.2 dB/facet, the estimated nonlinear refractive index of the laser written waveguide is 9.0×10^{-19} m^2/W, where propagation losses were ignored due to the low value. Considering the reported value of the nonlinear refractive index for pristine GLS glass through the Z-scan technique [3], 2.16×10^{-18} m^2/W, a nonlinear refractive index reduction of $\sim$2.4 times for laser written waveguides compared to the nonlinear refractive index of the pristine glass was observed. The laser inscription induces a decrease of the nonlinear refractive index in the laser irradiated region. Kar's group previously reported a reduction in the nonlinear refractive index of laser-written waveguides in GLS of approximately 4 to 5 times at 1550 nm wavelength [53].

Despite the reduction induced in the nonlinear refractive index during femtosecond laser writing in the bulk of GLS glass, the nonlinear properties of the waveguides are still strongly evident, proving that GLS glass is a promising platform for laser-written integrated nonlinear photonic circuits.

5.5 Gallium lanthanum sulfide waveguides as a cognitive photonic platform

In this section, some of the inherent characteristics of GLS glass are exploited in order to explore the functionality of this platform as a possible synaptic-like device, exploiting the photosensitivity of the laser formed waveguides in GLS glass.

Neuromorphic engineering is a re-emerging field that seeks the development of brain-inspired devices based on computations performed through biological synapses [185]. The principles sustaining the foundation of biological nervous systems have been the inspiration for the development of neuromorphic based software and devices since the late 1980s. The human brain consists of

$\sim 10^{11}$ neurons and $\sim 10^{14}$ synapses connecting all the neurons. Its unique colocalized memory and computation within a single unit [186], in contrast to Von Neumann architectures, has motivated intense research driven by the needs of artificial intelligence [187, 188] and "big data" [189]. A colocalization of storage and computational tasks within a single unit would provide more efficient devices with an optimized power consumption and computation times [190].

Compared to standard computational architectures, devices based on cognitive learning principles with neuromorphic distributed schemes are more advantageous. Apart from offering colocalization of storage and computation, cognitive hardware must also be self-learning, fault tolerant and adaptive to changing environments, massively parallel, three-dimensionally distributed and extremely compact [191–194].

Up to now, some of the most relevant work already demonstrated within this field entails complete cognitive computing systems. The clinical applicability of deep learning for diagnosis of diseases offering faster solutions than expert clinicians is already a reality [188, 195, 196]. For instance, Watson for Oncology developed by IBM is a supercomputer system that is being applied in several types of cancer diagnosis [195, 196]. Despite the enormous advance in software development, one of the main limitations of conventional computers is that they consume large amount of energy and time to compute these algorithms [197]. Just a 5 second simulation of human brain takes 500 s of computation in the most advanced cognitive softwares and needs a 1.4 MW of power [198]. As a solution, the integration of devices able to emulate neural networks, as a replacement of some small software blocks, has shown to speed up computation times while using less power [197, 199].

In the design of new cognitive devices, the selection of suitable materials capable of mimicking properties present in biological neural networks is indispensable. In this context, chalcogenide materials are a suitable platform for hosting photonic devices where non-volatile optical memories can coexist together with computing units due to their inherent characteristic as phase change materials [57, 58, 200]. Different synaptic electronic devices with programmable conductances have been previously explored, such as phase change and resistive change memories, ferroelectric switches, carbon nanotubes or field effect transistors [201–204]. Notwithstanding the progress in microelectronic devices, photonic approaches are expected to compete with the electronic counter-

part with possible ultrafast transmission speeds, higher bandwidths and improved power consumption [170,205]. Some of the photonic approaches already demonstrated are based on chalcogenide fibers [166] and silicon waveguides attached to phase change materials [11].

In this section, the results presented in [166] in GLSO optical fibers are investigated in laser inscribed waveguides in the bulk of GLS glass. The work presented here shows the potential of using femtosecond laser writing in terms of compactness and integration of optical circuits, preserving the intrinsic properties of the pristine material.

5.5.1 Biological system to imitate

Before describing the experimental details, a brief description of a biological synapse, including generation and transmission of action potentials for information flow across the brain, is explained.

Neurons are electrically excitable nerve cells capable of receiving, processing and transmitting information in the form of electrical and chemical signals. They are composed of dendrites, a body cell and an axon (with the axon terminals at its end). The dendrites are the input ports of a neuron and they are connected to junctions (synapses) between other neurons in order to receive the signals sent by them. The body cell carries out the basic life processes of the neurons. Axons are elongated channels that act as the output of a neuron, carrying the information from the body cell down towards the axon terminals. Axon terminals make the connections to the next neurons through synapses. The directionality of the information flow between two neurons starts in a pre-synaptic cell, being this one the sender cell, and moves towards a post-synaptic cell, being this last one the receiving cell. Neurons can connect to each other in order to form neural circuits with a vast number of interconnections. Fig. 5.12 shows a schematic representation of a pre-synaptic and a post-synaptic cells, where the synaptic cleft between both cells is shown in a magnified view in the inset.

Neurons have voltage-gated ion channels embedded in their plasma membrane and are electrically excitable since the membrane potential depends on the cell polarity. This potential is

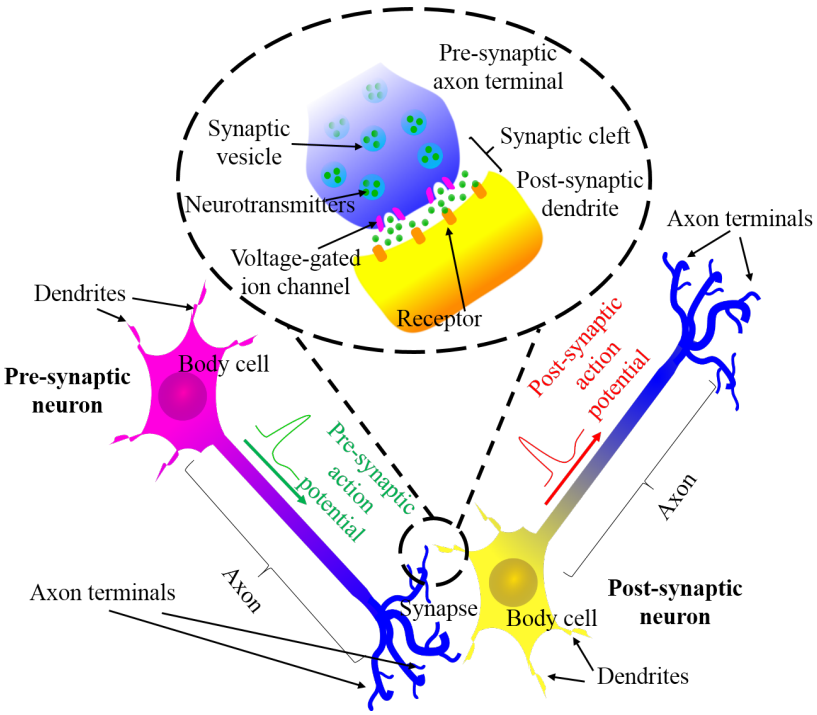

Fig. 5.12: Biological synapse between a pre-synaptic cell and a post-synaptic cell.

controlled by the ion concentration, such as Na^+ and K^+ concentrations, in the fluids inside and outside the membrane. Typically, the membrane of a neuron has a resting potential of -70 mV. When a cell is at its resting potential, the sodium and potassium ion channels remain closed, with Na^+ ions outside the membrane and K^+ ions concentrated within the cell. When an external stimulus takes place, such as a change in brightness, temperature or sound, the sodium channels begin to open as a response, allowing Na^+ ions rushing into the cell's membrane. This inward flow of sodium ions produces an increase of the membrane potential (depolarization). If the depolarization of the membrane potential reaches a certain threshold (about -55 mV), the process is followed by the opening of all the available ion channels in the cell, resulting in a large upswing of the membrane potential reaching a typical value of +40 mV. The rapid influx of sodium ions produces a throwback of the plasma membrane and the sodium ion channels are inactivated. Immediately, potassium ion channels activate and an outward flow of potassium ions takes place, giving back the electrochemical gradient to the resting state (repolarization). This process entails the generation of an action potential within a cell. A transient negative shift (hyperpolarization) occurs after the generation of an action potential. This continuous change in polarity allows the transmission of the action potential all along the axon of a single cell until its axon terminal, where it excites

other neurons.

In order to promote the flow of information towards other neurons, the generated action potential in a pre-synaptic cell is sent to the next (post-synaptic) neuron. Once the action potential has reached the axon terminals of the pre-synaptic neuron, the voltage-gated ion channels start to open, and an inward flow of sodium ions at the axon terminal's membrane of the pre-synaptic cell takes place. The exchange of calcium and sodium ions at the membrane of the axon terminal of the pre-synaptic cell causes the release of chemicals, called neurotransmitters, to the synaptic cleft. After neurotransmitters are released to the synapse, they diffuse across the synaptic cleft and get binded to receptors located in the plasma membrane of the post-synaptic cell. As a result, the membrane potential of the post-synaptic cell becomes more positive and if a certain threshold potential is achieved, the post-synaptic cell triggers an action potential.

In brief, action potentials are generated by neurons, propagated along their axons and transmitted to the next neuron across the synapses. Generation and transmission of action potentials is essential for information flow and processing in mammalian brains.

Inspired by the biological synapse, a photonic implementation simulating the generation and transmission of action potentials across laser inscribed waveguides in GLS glass is realized in this work. The laser inscribed waveguide represents a biological axon which carries the information, in the form of light, towards its output terminal. Under light irradiation (external stimulus) with energies near the absorption edge of GLS glass, the photonic axon or waveguide responds with a change in transmission, passing from a usual resting potential state towards triggering a spike and propagating it all along itself, towards its output (axon terminal).

5.5.2 Photonic synapse experimental setup

The experimental setup shown in Fig. 1.13 was developed in order to prove the functionality of the femtosecond laser written waveguides in GLS glass as artificial axons and synapses. Two diode lasers operating at the wavelengths of 800 nm and 532 nm were used. The 800-nm laser source was

a CW fiber-coupled laser (S1FC808, Thorlabs) offering a maximum output power of ∼20 mW. The emitted light from the laser output was coupled to a single-mode optical fiber (780HP, Thorlabs) and redirected to a fiber collimator (F280FC-780, Thorlabs) ensuring proper collimation for free space light transmission. The 532-nm light source was a CW free space light transmission laser (MGL-532-H-500, Roithner LaserTechnik) giving powers up to 500 mW. Two function generators connected to both light sources provided independent external signal modulations. The monitoring of the two modulated optical signals was given by the collection of the Fresnel reflections from two transparent glass slides into two independent optical detectors connected to an oscilloscope. A cube beam splitter with a 50:50 R/T ratio was used in order to make the remaining transmitted beams overlap in space. After the splitting of the optical beams, the collinear beam alignment was used to focus both of the optical beams into the input port of a laser-written waveguide by using an objective lens with a 10× magnification (5721-H-B, Newport). The guided light along the waveguide was collected at its output with a 16× collimating objective lens (5721-H-B, Newport) and filtered at 532-nm wavelength (NF03-532E-25, 532 nm StopLine single-notch filter) before being directed to a Si detector (818-SL-L-FC/DB, Newport) connected to the oscilloscope for a temporal control of the evolution of the optical power along the waveguide.

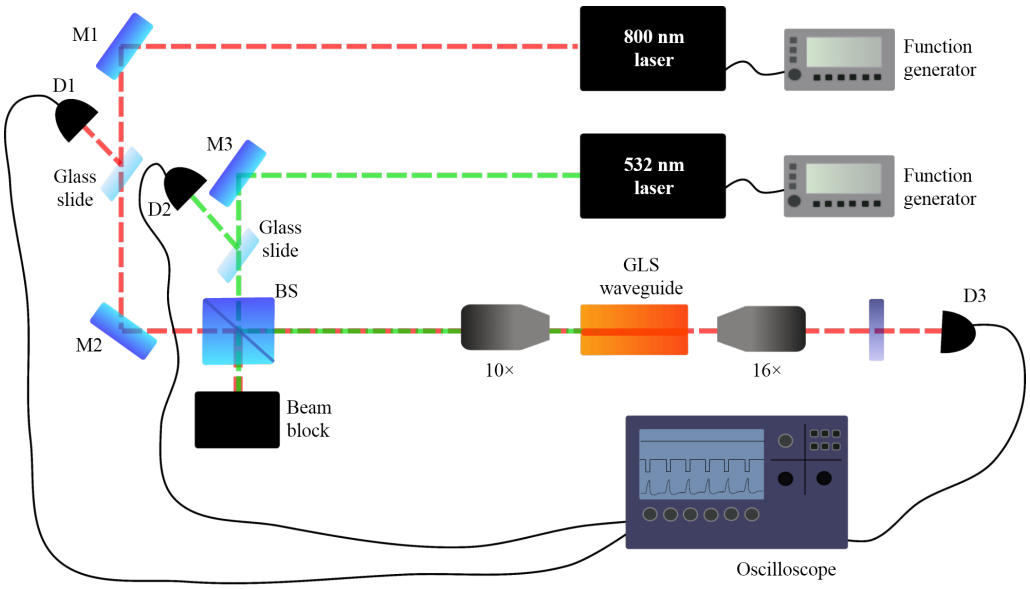

Fig. 5.13: Experimental setup used to mimic a biological synapse in a femtosecond laser written waveguide.

5.5.3 Results

Photodarkening

In the collinear beam experiment used to mimic the biological synapse the two incident beams contribute differently to the transmitted beam along the waveguide. The 800-nm laser beam is coupled and guided along the waveguide when focused at the waveguide input spot, whereas the 532-nm laser beam is absorbed when focused at the same region. This light absorption at 532 nm wavelength is due to a photoinduced effect in the GLS waveguide under illumination with energies below but near the optical gap of GLS glass. The absorption edge of the GLS substrates is about 527 nm. Photodarkening is the mechanism underlying the absorption of the 532-nm laser beam with a shift in the Urbach edge towards lower energies [181]. For energies far below the optical gap of GLS the waveguide material is transparent to the incident beam and allows light guiding along itself (see absorption spectrum from Fig. 3.2(b) in chapter 3).

Besides the independent behavior of each beam, it was observed that the transmission of the 800-nm laser beam was influenced by the presence of the 532-nm beam when both beams were focused at the input of the waveguide. This is possible due to the photodarkening induced by the beam at 532 nm, leading to a reduction in transmission of the 800-nm beam along the waveguide. In analogy to a biological synapse, the 532-nm beam plays the role of a pre-synaptic signal that sends information down to a post-synaptic neuron (the laser-written waveguide). This pre-synaptic beam creates a photonic synapse at the input facet of the waveguide where both beams, the one at 800 nm wavelength and the pre-synaptic beam at 532 nm, intersect. The pre-synaptic beam then induces a change in the membrane voltage (optical transmission) along the waveguide. The light launched into the waveguide at 800 nm wavelength is monitored to study the level of photodarkening induced in the waveguide.

Photodarkening can work in transient or in permanent regimes, depending upon optical power and exposure time. A transitory photosensitivity is observed when applying relatively low powers for short illumination times of the order of seconds. This transitory effect vanishes after the 532-

nm light is turned off and is accompanied by a full recovery of the waveguide transmission from the guided beam at 800 nm wavelength. The effect becomes permanent at either higher optical powers or longer exposure times than the ones leading to a transient photosensitivity, not obtaining a recovery in transmission of the guided 800-nm light after removal of the the 532-nm laser beam. The permanent photosensitivity displayed in the waveguide can be reversed by increasing the optical power of the 800-nm guided beam, causing a thermal annealing in the waveguide at the exposure point and recovering the initial transmission level [166].

Fig. 1.14 shows the effect of transient photodarkening. The transmission of the 800-nm beam along the waveguide as a function of the optical power applied from the 532-nm light source can be observed. Higher 532-nm optical powers cause larger reduction in the transmission of the 800 nm laser beam for a window of time of 15 seconds. A maximum power attenuation of 4.5% is achieved when applying ∼100 mW of optical power from the light source operating at 532 nm wavelength. For larger optical powers, the photodarkening saturates and the reduction in transmission is unaltered.

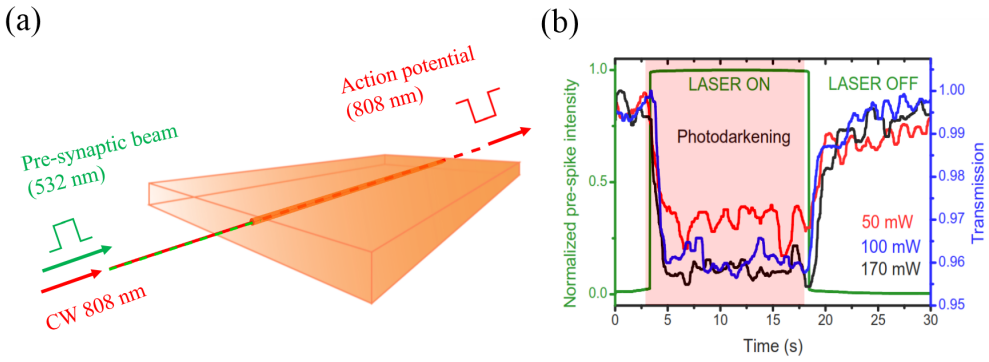

Fig. 5.14: (a) Schematic representation of the collinear beam approach. A CW laser beam at 800 nm wavelength is coupled into the laser-written waveguide and a pre-synaptic signal with energy near the absorption edge of GLS is sent to the waveguide in the form of a square pulse with a duration of 15 seconds. (b) By modifying the power of the 532-nm laser beam, the transmission along the optical waveguide can be modulated via transient photodarkening.

Excitatory and inhibitory post-synaptic potentials

In biological neural networks, synapses can either excite or inhibit its post-synaptic partner. There are neurons that release neurotransmitters that get binded to the receptors embedded in the post-synaptic neurons and trigger a *positive change* in the membrane potential of that neuron. These neurons are excitatory because they contribute to increase the probability of firing an action potential at the post-synaptic neuron by a *depolarization* of the post-synaptic membrane potential. If the triggering of an action potential from the excitatory pre-synaptic neuron occurs, then this action potential is known as an excitatory post-synaptic potential (EPSP). This phenomenon is caused by the entrance of positively charged ions within the post-synaptic neuron.

In contrast to this, there are also inhibitory neurons that release neurotransmitters through the synapse and these bind to the receptors of the post-synaptic neurons inducing a *negative change* in the membrane potential of the post-synaptic neurons. The opposite effect of an EPSP is an inhibitory post-synaptic potential (IPSP), which contributes with a decrease in the probability of a post-synaptic neuron firing an action potential. This phenomenon takes place either when positively charged ions flow out of the post-synaptic neuron or when negatively charged ions flow inside the post-synaptic neuron, causing a *repolarization* of the membrane potential.

By applying a selective modulation of the optical power from the 532-nm laser source, a desired modulation in transmission of the guided beam at 800 nm wavelength is performed. For the generation of photonic action potentials at the input of the waveguide (photonic synapse), three levels of transmission are selected: the resting state, the dark state and the depression state (Fig. 1.15). The resting state refers to the resting potential of a biological neuron and is achieved for an optical power of 20 mW from the pre-synaptic light beam. The dark state makes reference to the maximum membrane voltage that is achieved in a real neuron and corresponds to a fully transmission state in the absence of any pre-synaptic illumination. The depression state refers to the minimum membrane voltage achieved during the generation of an action potential in a nerve cell and is obtained at an optical power of 50 mW from the pre-spiking light source.

In analogy with the biological neural system, the generation and transmission of EPSPs and

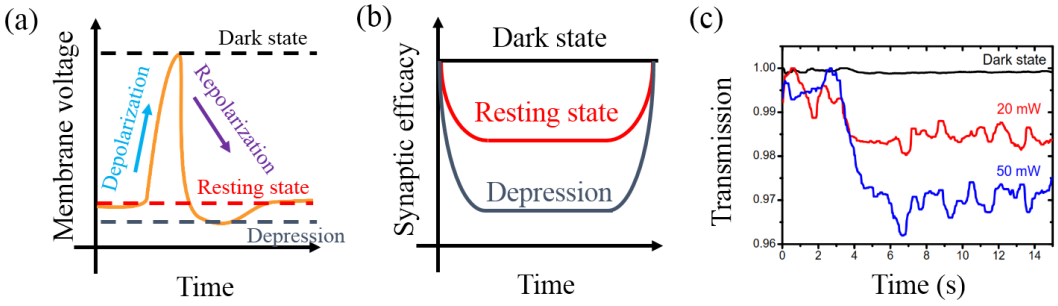

Fig. 5.15: (a) Typical plot of the membrane voltage over time during the generation of an action potential. (b) Three attenuation levels: dark, resting and depression states. (c) Three experimental power levels corresponding to the dark, resting and depression states found at the powers of 0 mW, 20 mW and 50 mW, respectively, from the pre-synaptic signal at 532 nm.

IPSPs is induced in the laser written waveguides. A constant modulation of the pre-synaptic beam between the transmission levels corresponding to the resting and dark states causes continuous depolarizations of the waveguide transmission at 800 nm wavelength, leading to the generation of a train of excitatory pulses (EPSPs) at the photonic synapse which travels all along the photonic axon. The EPSPs obtained in Fig. 1.16 where accomplished for a duty cycle of 70% and a modulation frequency of 13 Hz. The intensity modulation of the EPSPs is 0.4%. Similarly, power modulation of the pre-synaptic beam between power levels corresponding to the resting and the depression states induce continuous repolarizations in the waveguide transmission which result in the creation of an inhibitory pulse train (IPSPs). The IPSPs shown in Fig. 1.16 were achieved with a duty cycle of 30% at a modulation frequency of 13 Hz. A reduction in transmission of $\sim$0.6% is achieved in these IPSPs.

The duration of a single EPSP or IPSP generated at the photonic axon is about 15 ms and 20 ms, respectively. These pulse durations are in the same order of magnitude as the action potentials generated in animal's cells where the two main type of responses, the ones caused through calcium ion channels and the ones induced by sodium ion channels, present time durations of $\sim$1 ms and $\sim$100 ms, respectively.

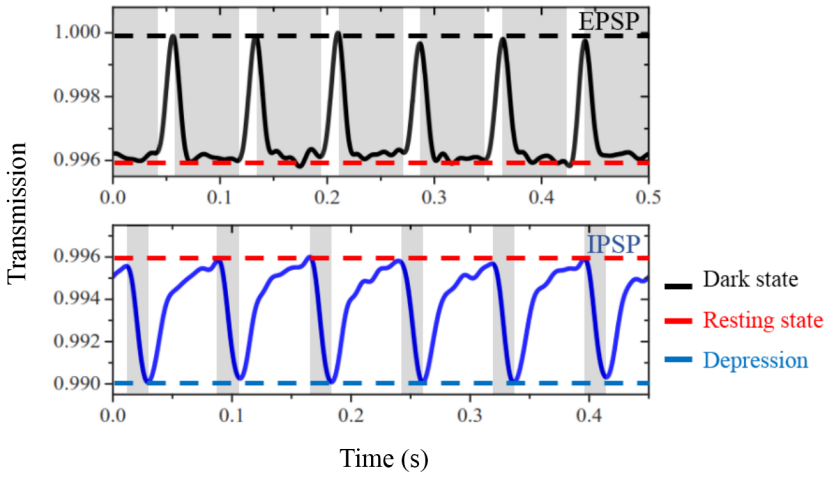

Fig. 5.16: By biasing the photonic synapse between different power levels, excitatory (upper panel) and inhibitory (lower panel) action potentials are generated at the photonic synapse and transmitted along the waveguide.

Temporal summations

In addition to individual excitatory and inhibitory potentials, the biological nervous system is able to integrate in time the individual EPSPs and IPSPs that are sent to a post-synaptic neuron. One of these types of synaptic integration is the temporal summation which takes place when a target neuron receives inputs from a single axon terminal repeatedly at short intervals causing the inputs to summate temporarily. The generation of a post-synaptic potential due to a temporal summation has always a longer duration than the interval between the input potentials from a pre-synaptic neuron. Sometimes, the biological temporal summation does not occur for all the received inputs but only for a partial number of them. This process is randomly selected in biological neurons depending on the synaptic strength between a pre-synaptic cell and a post-synaptic cell. The synaptic strength refers to the strength or amplitude of the connection between two neurons in order to fire a summation.

Laser-inscribed waveguides in GLS show the same behavior as in biological neurons. When a burst of optical pulses coming from the pre-synaptic beam is sent into the waveguide at high enough modulation power, temporal summation of the individual pulses, coming from a unique

photonic synapse located at the input of the waveguide, is achieved. In this case, the modulation of the pre-spike beam is applied between two power levels as in the case of generating EPSPs and IPSPs. However, in order to induce the temporal summation in the waveguide, one of the modulation power levels must overcome the power used as a depression state (50 mW) during the generation of individual excitatory and inhibitory action potentials. Input spikes at optical powers above ∼50 mW have shown to increase the probability of causing temporal summations in waveguide transmission since the time needed for a full recovery of the waveguide transmission, due to transient photodarkening, is longer than at lower powers, causing the input spikes to overlap or summate.

Fig. 1.17 shows the results obtained from temporal summations in a laser inscribed waveguide in GLS glass. The first case (Fig. 1.17(a)) corresponds to a complete temporal summation of a three-input-pulse train obtained with a 50% duty cycle and a modulation frequency of 5 Hz. The modulation intensity achieved in this case is $\sim 2\%$. The second graph (Fig. 1.17(b)) shows two burst of pulses coming from the input pre-synaptic signal, each of them form by a five-pulse train. Each burst of pulses was obtained with a 50% duty cycle and 10 Hz of modulation frequency. In this case, for two equal bursts of pulses the temporal summation takes place only for the two last pulses of the first burst, indicating an uncercainty about when and for how many pulses the photonic axon will trigger a summation. The modulation intensity achieved in this summation reaches almost the 3%. The photonic summations occur in a similar way than biological neural systems where decision uncertainty of neuron firing is always present.

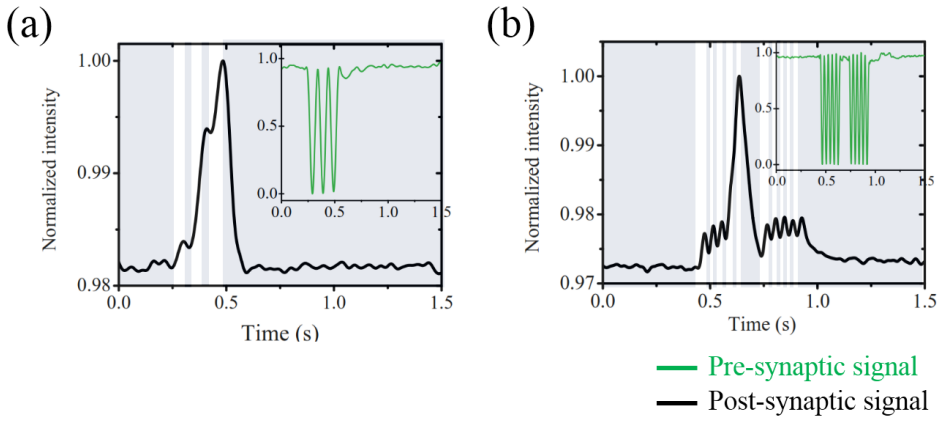

Fig. 5.17: Temporal summations in direct laser written waveguides in GLS glass.

Synaptic plasticity

During information processing across the biological nervous system, the synaptic junctions connecting neurons are constantly strengthened (potentiated) and weakened (depressed). This ability of the brain of tuning and undoing neural connections is known as plasticity and it controls how effectively two neurons communicate with each other. Plasticity is the brain's skill to adapt to new information and it underlies learning and cognition. Biological synapses are able to change their strength based on their own activity and/ or the activity in other pathways. The concept of neuralplasticity was first introduced by Donal Hebb in 1949 [206] stating that the connection strength between neurons is modified based on neural activities in pre-synaptic and post-synaptic cells. Within this frame, the concept of time plays an important factor for neuron firing. This theory accounting for time is a form of Hebbian learning known as Spike-timing-dependent plasticity (STDP) and postulates that the connection strength (synaptic weight) depends on the relative timing between a pre-skipe and a post-spike [207].

For propagation of action potentials in a biological system, a pre-synaptic cell must spike in order to promote the release of neurotransmitters into the synaptic cleft. As well, the post-synaptic cell must spike to induce the opening of the receptor valves that allow the binding of the neurotransmitters into them. The spiking of the post-synaptic cell must occur before the neurotransmitters are completely vanished or taken away. Thus, the closer a pre-spike is to a post-spike at the synaptic junction, the higher the connection strength (or relative synaptic weight change) induced in the post-synaptic neuron. The synaptic weight will keep diminishing in time as the neurotransmitter concentration drops in the synapse. In biological systems, the synaptic weight potentiates (increases) whenever a pre-synaptic spike precedes a post-synaptic spike repeteadly, and the synaptic weight depresses (decreases) when a post-synaptic spike precedes a pre-synaptic spike repeteadly. The change in percentage of synaptic weight is governed by the difference in time between a pre-neuron's and a post-neuron's firing spikes. Typically, the changes in intensity and sign of the synaptic weight occur within a temporal window of $\sim$100 ms in biological synapses.

As it occurs in biological neural networks, STDP is demonstrated in femtosecond laser-written

waveguides in GLS glass. In this part of the experiment, the pre-spike beam at 532 nm wavelength is applied in the form of a burst of pulses oscillating between two different power levels, following the same modulation frequencies and intensities used previously to form the EPSP and IPSP responses. This constant modulation makes possible to mimic the strengthening and weakening cycles at the photonic synapse in terms of waveguide transmission (Fig. 1.18(a)). As the photodarkening level keeps oscillating, a post-synaptic beam at the wavelength of 800 nm is launched into the waveguide, probing the level of photodarkening induced at the photonic junction. When the post-spike passes through the photodarkened point, it is alike when the post-synapse opens up the receptor valves to take in whichever neurotransmitters are released in the junction. The post-spike acts as a gate function for the pre-spike. The opening or closing position of the post-spike can be anywhere in this constant cycle.

Some of these curves containing potentiation and depression cycles, known as Hebbian learning windows, are shown in Fig. 1.18(b). Various forms of STDP are collected at different timings (for $\Delta t = 0$ chosen at t_1, t_2, t_3 and t_4) from measurements performed in waveguides inscribed in GLS glass. The plots show changes in the synaptic weight as a function of the relative arrival time between pre- and post- spikes. The relative change in waveguide transmission represents the changes in the neural connection strength (synaptic weight) between pre- and post- synaptic spikes. The arrival time of the post-spike relative to the pre-spike at the photonic synaptic junction ($\Delta t = t_{\text{post}} - t_{\text{pre}}$) contributes to a change in transmission along the waveguide, going through potentiation and depression cycles. For the case of the two windows with $\Delta t = 0$ fixed at timings t_1 and t_2, the relative spike timing equal to zero corresponds to the point where the post-synapse makes the decision to either open or close and remains being zero until this one opens again. As STDP predicts, whenever the pre-synaptic spike precedes the post-synaptic spike ($\Delta t > 0$), the synaptic strength increases or potentiates. Conversely, when the post-synaptic spike precedes the pre-synaptic spike ($\Delta t < 0$), the synapse decreases and goes through depression. Similar to biological systems, the proximity in time of the two spikes at the photonic junction changes the transmission levels generated within the waveguide. The closer a pre-spike is to a post-spike ($\Delta t \sim 0$), the larger is the change in the synaptic weight or waveguide transmission. Conversely, the further a pre-spike is to a post-spike ($|\Delta t| >> 0$), the smaller is the change induced in the synaptic weight or waveguide transmission.

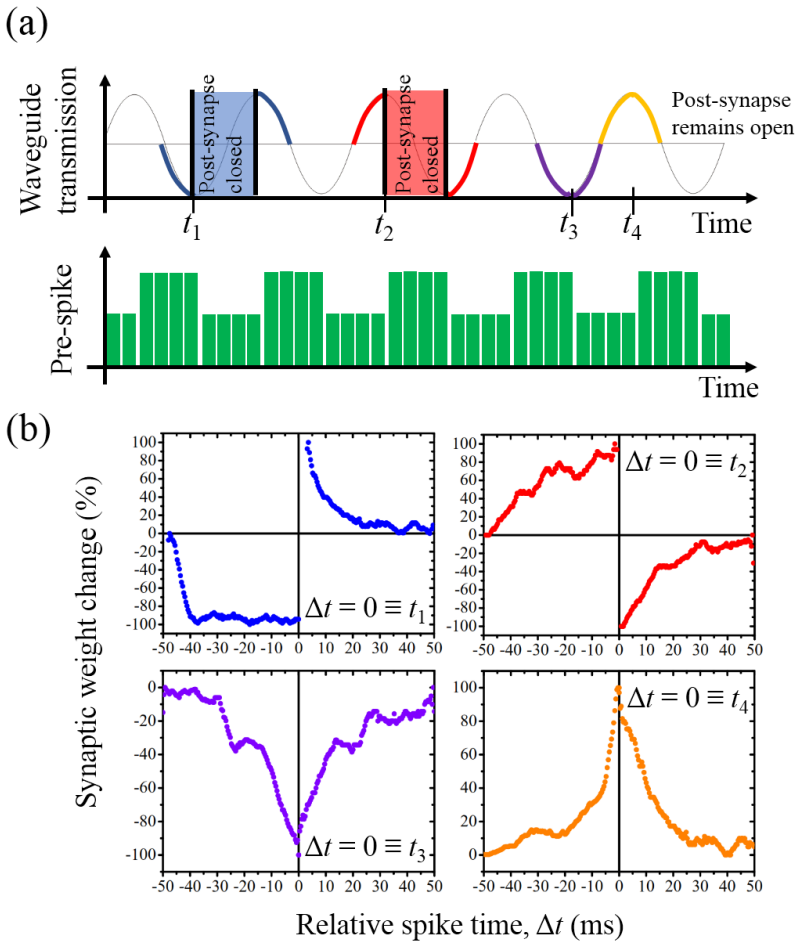

Fig. 5.18: (a) Pulsing scheme used to induce plasticity at the photonic synapse. (b) Various Hebbian learning windows obtained from a laser inscribed waveguide in GLS glass.

5.6 Summary

This chapter describes the first report of an optimum processing window for femtosecond laser inscription of waveguides in GLS glass offering single mode guiding at 800 nm wavelength. GLS glass was selected as the hosting material for nonlinear optical circuits due to its excellent FOM, presenting a high nonlinear refractive index and a low multiphoton absorption coefficient. The multiscan inscription approach used allowed waveguide fabrications at lower pulse energies than the single scan technique and led to waveguides with more symmetric and confined propagation modes with low insertion losses up to 2 dB for a MFD of 7.5 μm at 800 nm. Assuming a step

profile of the refractive index change and given the experimentally measured MFD of 7.5 μm, an estimated refractive index increase of $\Delta n = 10^{-3}$ was deduced using a commercial mode solver (Lumerical MODE Solutions).

The fabrication of S-bends and directional couplers, accompanied by a careful analysis on the number of scans used during directional coupler inscription and its effect on the power coupling ratio, has been reported. The role of directional couplers as ultrafast nonlinear all-optical switches has been performed by exploiting the Kerr nonlinearities of GLS glass. The resulting nonlinear properties of the femtosecond laser pulse irradiated volume in the bulk of GLS glass was studied by observing the nonlinear refractive index of the waveguides, obtained from the switching parameters. Femtosecond laser writing induced a reduction of the nonlinear refractive index of the irradiated volume of about 2 times, ensuring that laser written GLS waveguides are promising for integrated nonlinear photonics. The new processing window provided for ultrafast laser inscription of optical circuits operating in single mode at 800 nm offers solutions to optical circuits that can be employed as the building block of more advanced near infrared devices compatible with Ti:Sapphire technologies for ultrafast nonlinear switching and SPDC light sources for use in quantum information processing.

Finally, in the search for plastic and synaptic-like devices, we have demonstrated a photonic waveguide inscribed in chalcogenide material as the basic unit of an all-optical neural network. Intraneuronal communication protocols such as transmission of optical action potentials along the photonic axon have been demonstrated. Additionally, inter-neuronal communication protocols such as generation of action potentials at the synaptic junction, excitatory and inhibitory responses, neural summations and spike-timing dependent plasticity are displayed by the photonic axon. The plasticity and spiking characteristics come from the pristine material itself. The laser inscribed waveguide shows the potential of developing neuromorphic hardware by optically inscribing circuits hosted in chalcogenide glasses. Direct ultrafast laser inscription has enabled the integration of the work developed in optical fibers [166] into waveguides hosted within a centimeter-length chip. The low photodarkening efficiency accomplished within the waveguide, with a maximum reduction in transmission of about 4.5%, is attributed to the collinear alignment employed from the pre-spike beam. In future work, shallower waveguides will be employed in order to enhance the photodarkening efficiency by applying the pre-synaptic light beam from top of the waveguides.

Moreover, the inherent characteristic of chalcogenides as phase change materials could lead to a more complete integrated neuromorphic device where both optical memories and computing parts coexist together within the same unit. Colocalization of memory and computation units could be embedded through a controlled optical phase change at different illumination exposure points along a single waveguide, simultaneously increasing the number of synapses in a "photonic cell". Development of all-optical deep artificial neural networks might be feasible by inscribing multiple waveguides connected to each other in a different-layer distribution, offering enhanced power efficiency and computational speeds.

Chapter 6

Direct laser writing of waveguides in diamond

This chapter introduces the nitrogen-vacancy (NV) color center hosted in diamond and provides a review of the different fabrication methods employed to date for building optical guiding structures in diamond. The need of creating optical waveguiding deep in the bulk of diamond to reach NV centers with improved optical properties is pointed out here and the ultrafast laser writing technique is proposed as a feasible fabrication method able to supply buried optical waveguiding in diamond substrates. Moreover, the laser inscription technique is also proposed as an indirect fabrication method for the formation of NV color centers within the bulk of diamond by applying single femtosecond laser pulses below the amorphization threshold of the material. A review on the progress done in femtosecond laser writing in diamond is included and diamond substrates containing high nitrogen impurity concentrations of about 100 parts per million, grown by a high pressure high temperature (HPHT) process, have been selected for laser inscription of buried optical waveguides and NV color centers. Type II single mode optical waveguiding has been achieved at visible wavelengths. After waveguide formation and crystal lattice relaxation, laser writing has been applied in the way of single femtosecond laser pulse irradiation along the waveguides in order to induce the formation of vacancies within the crystal lattice. A subsequent thermal treatment has been employed in order to promote the diffusion of the laser-induced vacancies towards

the vicinity of intrinsic nitrogen impurities contained in the diamond substrates. The thermal annealing employed does not affect the guiding properties. The waveguide-NV ensemble structures provide an optimum optical guiding at 532 nm wavelength for optical excitation of NV defects placed all along the waveguides and an enhanced optical collection of the photoluminescence emission from NV centers. The photoluminescence emission coming from waveguides with and without irradiated single pulses has been characterized and the role of the single femtosecond pulse irradiation for the formation of NV color centers in HPHT diamond substrates has been studied from confocal photoluminescence mapping.

The work presented in this chapter has been performed at the Politecnico di Milano, Italy, as an attachment of the PhD program.

6.1 The diamond nitrogen-vacancy center

The nitrogen-vacancy color center is a point defect in the carbon lattice of diamond consisting of a nearest neighbor pair of a substitutional nitrogen atom with a lattice vacancy. Fig. 6.1(a) shows a schematic representation of the atomic structure of an NV center in diamond. Since nitrogen has five valence electrons, three of them are shared with the nearest-neighbor carbons and the other two form part of the "bond" with the vacancy. On the other hand, the vacancy holds five unsatisfied bonding electrons, two from the nitrogen atom and three from the surrounding carbon atoms. The color defect can coexist in two different charge states: the neutral charge state, NV^0, with five electrons occupying the vacancy's surroundings, and the negative charge state, NV^-, when there is an additional electron forming part of the dangling bond of the vacancy, coming from another defect in the lattice. Especially, the NV center in its negative charge state has been exploited as a single photon emitter for applications in quantum information and magnetic sensing, between others [208, 209].

The characteristic electronic structure of the NV^- center is depicted in Fig. 6.1(b), consisting of a ground and excited states formed by spin triplets with ^{3}A and ^{3}E symmetries, respectively, and an intermediate metastable single state ^{1}A. The triplet ground state of the NV^- center can be

polarized by optically pumping at 532 nm wavelength, leading to a de-excitation via a fluorescence emission with a characteristic zero phonon line (ZPL) at 637 nm.

The peculiarity that the ground state sub-level $m_s = 0$ fluoresces more brightly than the $m_s = \pm 1$ ground sub-level spin state, due to the possibility that the latter electronic state goes through relaxation via a non-radiative decay path, which is useful for optical readout of the spin state and its initial state preparation for further manipulations. In this way, the NV^- center can be used as the basic unit for quantum information processing, a qubit, in which a two-spin-state system can be either in one of the two states allowed or in a coherent superposition of both spin states (as depicted in Fig. 6.1(a)).

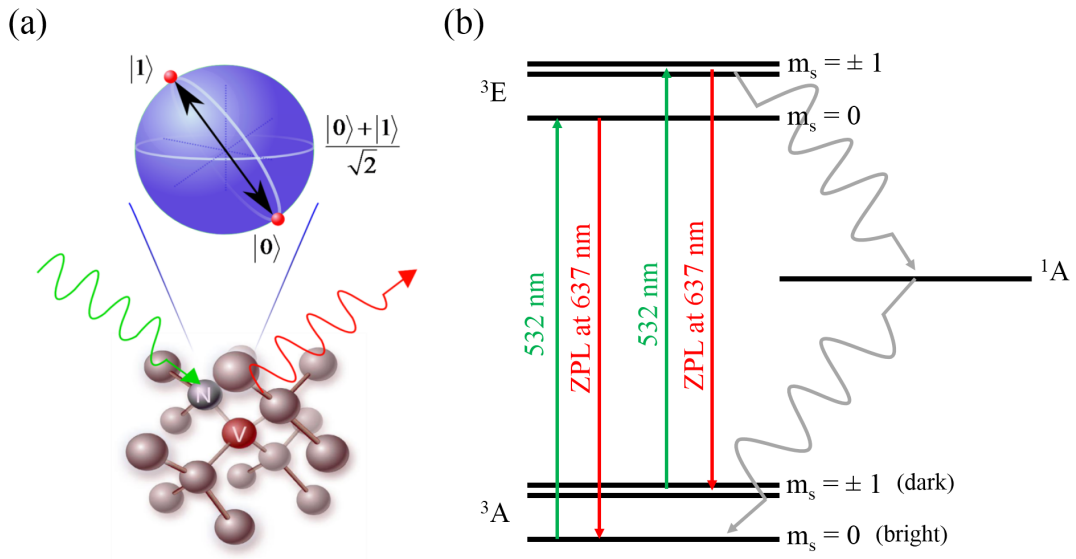

Fig. 6.1: (a) Typical atomic structure of the tetrahedral carbon lattice of diamond hosting an NV color center which is optically excited at 532 nm wavelength, resulting in a photoluminescence emission with a ZPL at 637 nm. The NV may be used as a quantum qubit. (b) Electronic structure of an NV color center in its negative charge state and all the viable optical excitation and de-excitation paths.

NV^- centers present weak spin-orbit coupling and are surrounded by a spinless carbon lattice which results in a low-noise quantum system with outstanding coherence times of $\sim$1 ms, comparable to that of trapped ions, at operational room temperatures [2]. Additionally, the NV^- spin states have shown to respond in the presence of magnetic fields via the Zeeman splitting [210], offering capabilities as magnetometers with atomic sizes and extraordinary sensitivities comparable

with existing technologies, as shown in Fig. 6.2.

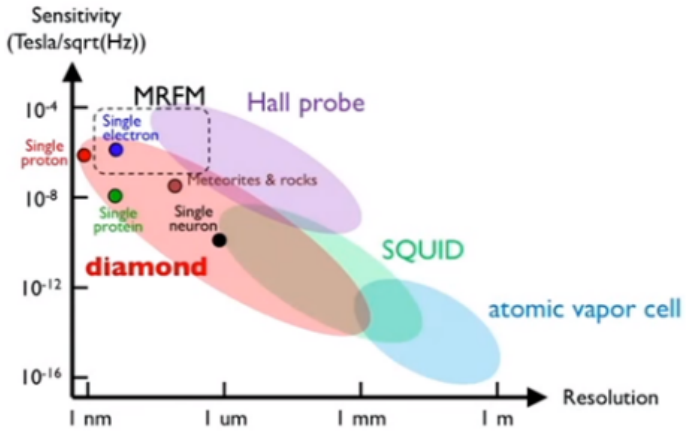

Fig. 6.2: Classification of current competitive technologies for magnetic sensing. Figure acquired from a talk given by Prof. Ronald Walsworth, Harvard University at the DIADEMS summer school 2016, Cargese, France.

Depending on the properties of the hosting diamond, NV^- centers can emerge as isolated defects or in high density ensembles with viable NV^--NV^- spin entanglement over relatively long distances via photonic excitation through optical guiding structures [2]. The NV^- color center in diamond has emerged as an advantageous defect for compact and scalable quantum information systems and high sensitivity magnetic sensors. The fabrication of optical guiding structures enabling optical excitation of NV centers and an optimum collection of their photoluminescence emission is indispensable. From now on, the NV^- color center will be referred to simply as NV.

6.2 Review in fabrication methods for optical waveguiding structures in diamond substrates

With the aim of using the beneficial properties displayed by NV color centers hosted in the bulk of diamond, the search for fabrication methods that enable optimum optical excitation of NV centers and subsequent collection of NV flourescence emission is indispensable. The challenges met when trying to find a way to process optical waveguiding in diamond are many. In first place, shallow NV centers in diamond present reduced coherence times induced by external noise introduced into

the system due to proximity to the diamond surface. The coherence time, T_2, involving the dipolar interaction of the spin of a single NV center with the "spin bath" formed by the surrounding NV centers [2], has been measured in implanted shallow NV centers located at a depth of 2.1 nm with values of 12.2 μs, whereas deeper native NV centers placed 6 μm below the surface of diamond present coherence times notably improved with a value $T_2 \sim$128 μs for the case of quantum grade diamond (5 parts per billion of nitrogen impurities) [211]. For this reason, a fabrication method that enables deep optical waveguiding within the bulk of diamond, where NV coherence times are highly improved, is desirable.

Aside from the issue of creating guiding structures deep in the bulk of diamond to not deteriorate the original properties of NV centers, the high refractive index of 2.4 in diamond presents a challenge when it comes to collecting the fluorescence emission coming from NV centers. A high refractive index results in a small angle of total internal reflection at the diamond-air interface. This reduces the optical collection efficiency of the NV fluorescence emission from the bulk of the substrate, making direct optical collection from a microscope objective a non-viable option since the optical collection efficiency is notably reduced due to refraction at the interface between the substrate and the air. The choice of using index matching oil connecting the diamond-air interface for optical collection of NV centers has been discarded since it is not feasible for low temperature measurements.

Some of the approaches used to create optical waveguiding in diamond have employed the focused ion beam technique along with thermal annealing, chemical etching and a lift-off process. The first waveguide fabricated in the bulk of single-crystalline diamond was reported by Olivero *et al.* in 2005 [212] by using this method. Despite all the efforts, the focused ion beam implantation has shown to degradate the properties of the NV color centers due to an induced stress in the diamond films [213]. More recent work has been based on thin film deposition of high refractive index materials on top of diamond substrates. The use of this technique has enabled micro and nano cavities coupled to NV centers near the diamond surface [214] and optical waveguides [215]. However, the coupling efficiency of surface guiding structures with NV centers located in the bulk of diamond is not ideal, being also influenced by surface roughness.

In a trial for improving the optical collection efficiency of NV fluorescence emission, recent

efforts based on photolithography and selective ablation of diamond to form air-diamond interfaces have been employed [216, 217]. Also, a novel etching technique has been reported by Burek *et al.* [218] introducing the use of an angled-etching method which requires the use of a Faraday cage, enabling free-standing photonic components in diamond such as suspended nanobeam optical waveguides, nanobeam mechanical resonators and microdisk cavities. However, etching fabrication methods are not desirable since they exhibit remarkable sensitivity to surface roughness and poor repeatibility depending on concentration and temperature of the etchant. Also, they require the use of cleanroom facilities and multi-step material processing. Additionally, ion beam writing has been used for the fabrication of shallow waveguides, but with limitations to two-dimensional fabrication geometries [219]. Despite all the multiple techniques presented, none of them provide a solution for the fabrication of deep waveguides in the bulk of diamond.

To overcome all the actual challenges, a direct practical solution is the use of a fabrication technique that enables the formation of guiding structures within the bulk of diamond, simultaneously enabling an optimal NV optical excitation and collection efficiencies while still maintaining the NV coherence times.

6.3 Progress in femtosecond laser writing of waveguides in diamond

Femtosecond laser writing could provide a solution for all the challenges mentioned in the previous section. The first demonstration of a femtosecond laser written waveguide in the bulk of optical grade diamond (containing 100 parts per billion of nitrogen impurities) was reported in 2016 by Sotillo *et al.* [109]. In this work, the prevention of graphite formation during waveguide fabrication, which would be detrimental due to its optical absorptivity, was achieved by processing waveguides at high repetition rates (500 kHz). The resulting waveguides, located at 40 μm below the diamond surface, belonged to a type II modality and presented single mode guiding with an insertion loss of 11 dB at 635 nm wavelength. Photoluminescence confocal measurements provided equal photoluminescence spectrum coming from the optical guiding region and the pristine

material, proving that the waveguide fabrication method did not degrade the diamond lattice along the optical guiding region [109]. This work also reported the linewidths of the hyperfine structure of the diamond's intrinsic NV centers located along the optical guiding region and in the pristine diamond, resulting in comparable values demonstrating preservation of the NV's properties. [109].

Previous studies to this first demonstration had shown formation of graphitic lines along the focal region of irradiated pulses during femtosecond laser writing in diamond substrates at 1 kHz repetition rate [220]. Shortly after the first demonstration of a laser-written waveguide in diamond substrates [109], Courvoisier *et al.* reported also the formation of waveguides in diamond through ultrafast laser inscription at low repetition rates (1 kHz) with the use of a spatial light modulator and a vertical multiscan approach [221]. The use of a spatial light modulator ensured the correction of the strong spherical aberration created in diamond, allowing waveguide fabrications at any depth within the diamond substrates. Single mode optical waveguides and a Y-splitter with a 50:50 splitting ratio with estimated insertion losses of 7.9 dB and 7 dB were respectively reported at 780 nm wavelength [221].

In [109], it has been described that the laser writing in diamond induces the formation of amorphous carbon and photoluminescence measurements have confirmed the formation of a large amount of defects, mainly vacancies or vacancy complexes. This fact led to the idea of creating vacancies within the bulk of diamond by using femtosecond laser writing at low pulse energies below the amorphization threshold of the crystal ($\sim$50 nJ). Usual methodologies for implantation of color centers consist of electron or ion irradiations within the diamond samples, introducing residual damage into the crystal lattice and deteriorating the properties of the NV centers [222].

The first demonstration of single NV generation within the bulk of diamond via laser writing was reported by Chen *et al.* [223], showing a controlled selection of the position of the NV centers within the diamond lattice by using adaptive optics for aberration correction. Single femtosecond laser pulses were used to generate vacancies in the bulk of diamond. A subsequent thermal annealing was used to promote the vacancy migration towards the intrinsic nitrogen impurities contained in the diamond samples, resulting in the formation of stable NV color centers. The reported success probability of creating an NV defect within 200 nm distance from the irradiated area was 45 $\pm$ 15% for diamond samples with a nitrogen concentration below 5 parts per billion ($\sim$900 atoms

per μm). After this work, Sotillo *et al.* [112] showed deterministic placement of single NV centers in diamond without the need of using adaptive optics, obtaining a success probability of forming an NV center within a spatial accuracy of $\sim$1 μm^3 volume of about 50% for diamond samples containing the same nitrogen impurity concentration as the diamond used in [223].

The achievement of combining optical waveguides and single NV color centers as an integrated waveguide-NV coupled device by exclusively using femtosecond laser writing has been reported by Hadden *et al.* [69]. The work developed here enabled optical excitation and collection of laser-written NV color centers via light coupling into a laser-written optical waveguide in bulk diamond. It was also proved that the required thermal annealing, applied after laser writing of waveguides and vacancies to induce the mobility of vacancies towards the nitrogen impurities, did not deteriorate the properties of the waveguides, mantaining the same mode profiles and waveguide losses presented before the realization of the annealing. The reported probability of creating single NV color centers within the waveguides was 40% for a diamond substrate containing a nitrogen density below 5 parts per billion and single photon emission at room temperature was detected from the laser-written single NV centers.

Lastly, a recent improvement in the probability of laser-written NV center formation within diamond substrates was accomplished by replacing the thermal annealing usually employed with a train of focused femtosecond pulses at low energies [224]. The substituent low energy femtosecond pulse writing proved the mobilization of the vacancies at the laser exposed spots with a yield of 96% in NV center formation and a positioning accuracy of 50 nm for diamond samples with high nitrogen impurity concentration ($\sim$100 parts per million) [224].

Although there is great room for improvement, femtosecond laser writing has demonstrated to be a competitive technology for the formation of optical guiding structures, color center defects and the integration of these two combined in an on-chip diamond platform with feasible applicability in quatum information systems.

6.4 Ultrafast laser inscription of type II bulk diamond waveguides coupled to an ensemble of NV centers

After providing a detailed review of the work already developed in laser writing of waveguides in diamond in the previous section, the next challenging step is the ultrafast laser fabrication of ensembles of NVs that can be optically excited and collected in an efficient manner and, thus, providing an enhanced photoluminescence emission compared to single isolated NVs.

For instance, one of the drawbacks of using single NVs as magnetic and electric nanoscale sensors is that their sensitivity is limited by the measurement of a single NV center. As a solution, devices based on spin state entanglement of a large number of NVs would result in a greater sensitivity led by an enhancement proportional to $\sqrt{N}$, where N is the number of NV centers constituting the ensemble [225]. As an example, ion-implanted NV ensembles contained at the surface of thin film diamond substrates have already demonstrated their role as sensors in the detection of single neural action potentials [226] and larger sensitivities have been demonstrated by using NV ensembles in naturally NV rich bulk diamond substrates [227, 228].

Femtosecond laser writing offers the possibility of creating optical waveguides coupled to an ensemble of NVs, enabling optical excitation and collection of the ensemble acting as a spin entangled system for quantum sensing devices. Here, the fabrication of optical waveguides and vacancy defects within the bulk of diamond substrates using the femtosecond laser writing technique has been employed. The diamond substrates selected were commercially available and had been subjected to a growth process of high pressure high temperature (HPHT), which leads to the formation of diamond substrates containing a high amount of nitrogen impurities ($\sim$100 parts per million), as it was convenient for creation of large ensembles of NV centers.

The micromachining workstation detailed in chapter 3 (section 3.1) was used to laser write waveguides within the bulk of HPHT diamond substrates. Due to the high linear refractive index of 2.4 in diamond, an oil immersion objective lens (RMS100X-O 100$\times$ Olympus Plan Achromat Oil Immersion Objective, 100$\times$ oil immersion, Olympus) was required during waveguide fabrica-

tions to reduce the refraction caused at the optical path between the objective lens and the diamond substrate. Also, the oil immersion objective lens had a high NA of 1.25, needed to form uniform laser modifications within the bulk of diamond with a reduced spherical aberration, since the use of adaptive optics was not available from the fabrication system. Unlike laser writing of waveguides in glasses, where the irradiated volume experiences an increase in the refractive index enabling direct optical waveguiding, femtosecond laser pulses focused within the bulk of crystals produce a lattice damage which results in a decrease of the refractive index and creating a stress around it [229]. Thus, optical waveguiding within the bulk of diamond can be achieved by laser writing two closely spaced parallel lines [109], as illustrated in Fig. 6.3. This waveguide fabrication technique is known as the type II modality [109].

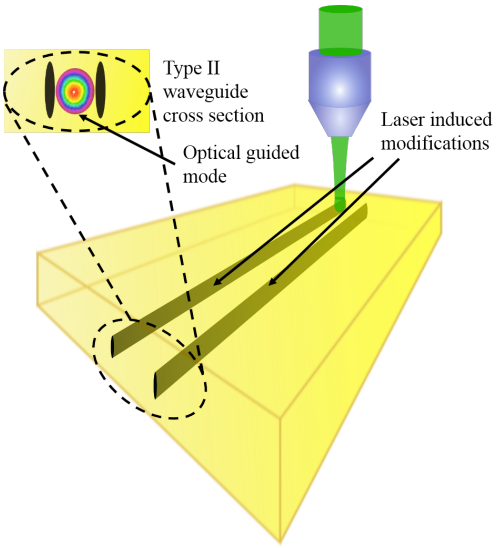

Fig. 6.3: Type II waveguide laser writing modality in diamond. The laser induced modifications result in a lower refractive index than the pristine crystal lattice, allowing optical mode confinement in between two laser written lines due to stress.

Single mode waveguides operating at visible wavelengths were targeted in order to ensure an efficient optical excitation of the NV centers through an optical guiding at 532 nm wavelength and optical collection of the photoluminescence emission from NVs at about 637 nm wavelength. The general processing parameters chosen from the machining station to form waveguides in HPHT diamond samples were an incident wavelength of 515 nm, enabling nonlinear absorption of two photons within the focal volume, 300 fs pulse duration and a repetition rate of 500 kHz. The high repetition rate used was selected in order to prevent the formation of graphite within the laser irradiated lines, as reported in [109]. Incident pulse energies ranging from 40 nJ to 60 nJ, in steps

of 10 nJ, and a scan speed of 0.5 mm/s were employed for waveguide fabrications. To achieve single mode optical waveguiding at visible wavelengths, the spacing between the two parallel laser-written lines composing a single type II optical waveguide was chosen to be 13 μm, as it was previously reported by Sotillo *et al*. [109], and the inscriptions were performed at 18 μm, 20 μm and 22 μm below the sample surface. The polarization of the incident laser beam did not show any dependence during waveguide inscriptions within diamond substrates.

Right after the inscription of each optical waveguide and subsequent material relaxation, the ultrafast laser inscription technique was used to focus single femtosecond laser pulses all along the waveguide in consideration, at an equidistant midpoint between the two laser-written lines forming the type II waveguide. The distance between consecutive irradiated femtosecond pulses along the axial direction of the waveguides was kept at 1 μm. The single static exposures were employed to induce the formation of vacancy defects at the irradiated volume within the substrate [112, 223]. Incident pulse energies ranging from 12 nJ to 20 nJ, in steps of 2 nJ, were used for the inscription of single pulses along different waveguides, keeping the pulse energies employed below the amorphization threshold of diamond ($\sim$50 nJ) [112]. The inscription of single static exposures was performed at 20 μm depth.

After laser writing of waveguides and vacancy defects, the substrates were subjected to a thermal annealing in a tubular furnace (Lenton LTF15/50/450), where the substrates were placed in a quartz boat and covered with diamond powder to prevent the sample surface from any oxidation. The oxygen present in the furnace was extracted using a diaphragm pump and a nitrogen flow during 1 hour. Subsequently, a thermal treatment was performed under a nitrogen atmosphere by following a three steps process: from ambient temperature, a thermal rising ramp rate of 5.4°C per minute was employed for 3 hours until the temperature rised to 1000°C, then the substrate was hold at 1000°C for 3 hours and, lastly, the furnace was switched off in order to let the substrate cool down to ambient temperature. The employed thermal annealing was used to activate the vacancy migration process, where the vacancies created through laser writing of single pulses start moving towards the nitrogen atoms fixed in the diamond lattice and, thus, leading to the formation of NV color centers [112, 223]. This is possible because the diffusion of the vacancies in diamond starts at 650°C, whereas the diffusion of nitrogen atoms in diamond occurs at 1500°C [2].

The morphology of the laser-inscribed waveguides within the bulk of diamond substrates was characterized under an optical microscope, in transmission mode, using $10\times$ and $40\times$ magnification objectives (Eclipse ME600, Nikon). For characterization of waveguide losses, the chip to fiber butt coupled method detailed in chapter 3, section 3.3.2, was employed. The waveguide mode profile at the near field was characterized with a $60\times$ aspheric lens (5721-H-B, Newport) in order to image the guided mode onto a beam profiler (SP620U, Spiricon).

The resulting waveguides showed optical waveguiding only for TM polarized light, as reported elsewhere [109, 221]. The reason for having only one guiding polarization is due to the presence of compressive stress in the horizontal direction and tensile stress in the vertical direction, as reported in [230] through polarized micro-Raman studies of the laser-written waveguides. This stress distribution induces an increase in the refractive index for the TM polarization, whereas the TE polarization sees a decrease in the refractive index between the two lines. The TM polarized mode can be confined in the horizontal direction due to the two laser-written lines which have a reduced refractive index compared with the pristine crystal lattice, while its confinement in the vertical direction is due to a stress-induced refractive index change [230]. The waveguide performance (mode field diameter and waveguide losses) was not affected by the single static exposures employed to create the vacancy defects and resulting NV color centers along the waveguides, since the pulse energies used were relatively low.

The laser pulse energy showed to have a dependence with the size of the waveguides. Usually, applying higher pulse energies during waveguide fabrications led to more vertically elongated optical modes when coupling light at 635 nm wavelength. Fig. 6.4(a) gives information about the vertical elongation of the optical guided modes in waveguides formed under different pulse energies and depths, where $\mathrm{MFD_Y} - \mathrm{MFD_X}$ refers to the difference between the experimentally measured mode field diameter along the vertical direction and the experimentally measured mode field diameter along the horizontal direction of the optical mode at 635 nm wavelength. But, not all the cases followed strictly this general trend, the increase in the vertical elongation of the modes is due to a larger spherical aberration when higher pulse energies are focused within the bulk of diamond. Generally, the mode field diameter along the horizontal direction ($\mathrm{MFD_X}$) did not experience any changes when varying the pulse energy, and only the mode field diameter along the vertical direction ($\mathrm{MFD_Y}$) experienced a general growth of few micrometers when slightly

increasing the pulse energy for waveguide fabrications. This can be attributed to the elongation of the vertical side walls due to spherical aberration with the power.

The waveguide depth did not show any clear effect on the resulting waveguide properties. Fig. 6.4(b) shows the waveguide insertion loss (IL) as a function of the pulse energies used during waveguide fabrications at a depth of 20 μm. The waveguide insertion loss did not show any dependence on any of the processing parameters used. Despite presenting a pronounced vertical elongation, the waveguide containing a minimum loss was obtained at a pulse energy of 60 nJ for an inscription depth of 20 μm, resulting in an overall insertion loss of 6.8 dB, from a Fresnel reflection loss of 0.3 dB/facet, a coupling loss of 3 dB/facet and a propagation loss of 1 dB/cm when launching light from a polarization-mantaining optical fiber in TM mode at 635 nm wavelength.

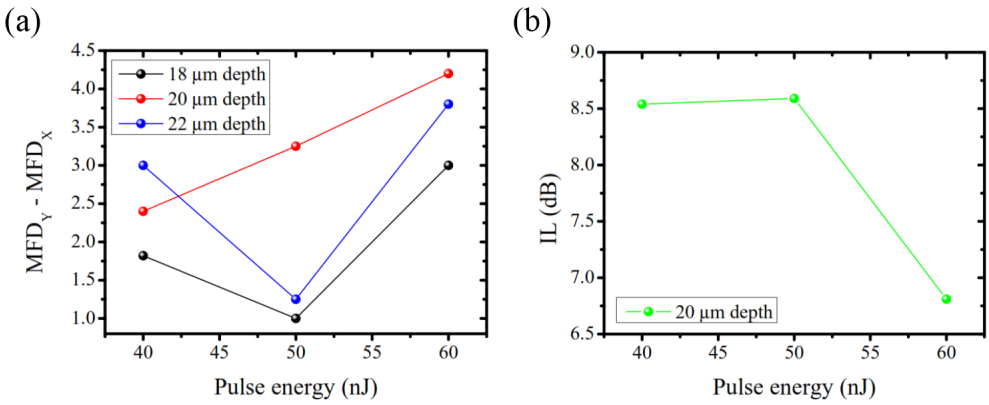

Fig. 6.4: (a) Effect of processing pulse energy on the vertical elongation of the optically confined waveguide modes at 635 nm wavelength. (b) Waveguide insertion loss as a function of the incident pulse energy for waveguides fabricated at 20 μm below the sample surface.

Fig. 6.5(a) shows an overhead white-light microscope image of various laser-written lines composing an array of type II waveguides within the bulk of diamond substrates. Unlike laser inscribed waveguides in glasses, the modifications formed by the focused femtosecond laser pulses within the diamond lattice result in dark lines at the focal volume, inferring a strong material change, such as amorphization/ graphitization of the original crystal lattice. The spots where single static exposures were applied in order to form vacancy defects along the waveguides are not distinguishable under optical microscopy due to the low pulse energies used below the amorphization threshold of diamond. A transverse view of a laser-written waveguide in the bulk of diamond can be observed in Fig. 6.5(b). The vertically elongated laser induced lines composing the type II waveguide are due to the spherical aberration caused within the bulk of diamond due to its high linear refractive index. The optical guided mode of the waveguide presenting minimum insertion losses of 6.8 dB at 635 nm wavelength is illustrated in Fig. 6.5(c).

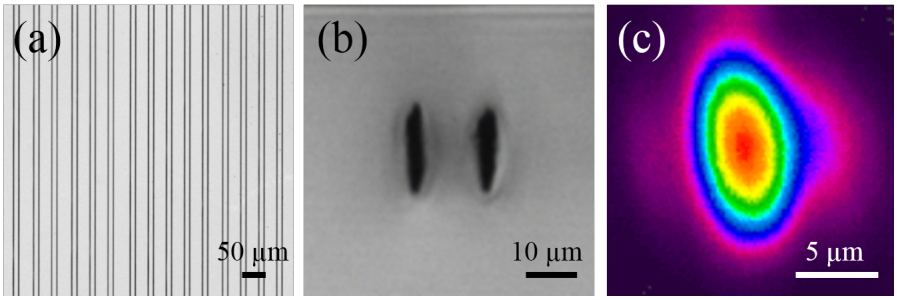

Fig. 6.5: (a) Overhead microscope image of an array of type II laser-written waveguides in diamond. (b) Cross section of a type II laser inscribed waveguide within the bulk of diamond. (c) Waveguide optical mode with a MFD $= (11 \times 15)\ \mu\text{m}^2$ for launched TM polarized light at 635 nm wavelength.

6.5 Photoluminescence characterization setup

A free space optics setup was used for the characterization of the photoluminescence signal generated all along the laser-written waveguides in diamond, as depicted in Fig. 6.6. The output optical beam of a doubled frequency Nd:YAG laser was directed onto a half wave plate (HWP) and subsequently coupled into the waveguide under consideration by using a 0.16 NA focusing lens. The optical coupling and waveguiding, centered at 532 nm wavelength, was used to optically

excite the ensemble of NV centers formed along the waveguides. The guided light was collected at the output of the waveguide by a 0.25 NA collimating objective lens and subsequently filtered at 532 nm wavelength by using a single-notch filter (NF03532E-25, 532 nm StopLine) in order to substract the optical pump from the NV optical emission. The filtered beam was then directed onto a spectrometer (Ocean Optics USB2000) for the collection of the optical emission generated along the laser-written waveguides.

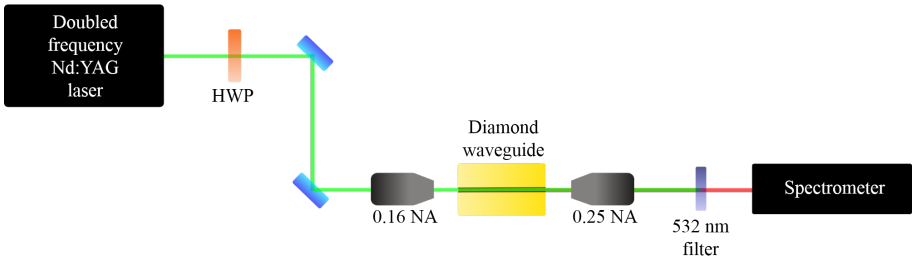

Fig. 6.6: Free space optical setup for characterization of the photoluminescence emission coming from ensembles of NV color centers located along the laser-written waveguides in diamond.

6.6 Photoluminescence results

Using the free space optics setup described in the previous section, the optical emission coming from one of the laser inscribed waveguides in HPHT diamond, containing single static exposures, is shown in Fig. 6.7 after filtering the optical pump. The experimental data in black color corresponds to the photoluminescence signal collected at the output of a waveguide when the optical pump has a TM polarization. The data in red indicates the photoluminescence emission of the same waveguide but when the polarization of the optical pump was TE. The experimental data in blue comes from the optical collection of the pump signal filtered when shining the outer proximity of one of the laser-damaged lines that composes the waveguide (corresponding to the bulk diamond). In this last case, no photoluminescence signal has been detected. From the black and red color curves, a luminescence collection 4-5 times larger for TM polarized pump light with respect to the luminescence intensity collected at TE polarization of the pump is due to the unique TM polarization guiding allowed in type II waveguides in diamond. The various peaks that can be distinguished from the emission spectra coming from the waveguide for both TM and TE pump

polarizations correspond to the first order Raman peak located at 572 nm, a zero phonon line (ZPL) at 576 nm associated to NV^0 color centers, the strong ZPL at 637 nm from NV^- centers and its associated vibronic band that extends from the ZPL towards longer wavelengths [2]. These results suggest the formation of NV centers along the laser-written waveguides in comparison with the bulk, indicating that only a TM polarized optical pump is optimum for an efficient optical guiding and posterior excitation of NV centers.

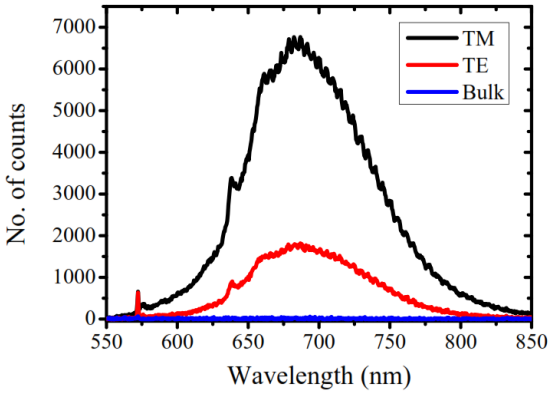

Fig. 6.7: Emission spectra coming from a waveguide and from bulk diamond after optically pumping with a 532-nm light and subsequently filtering the pump. The spectrum in black refers to the optical emission from a waveguide containing single static exposures for a TM polarization of the pump. The spectrum in red corresponds to the emission of the same waveguide when the optical pump is TE polarized. The experimental data in blue corresponds to the optical collection from the bulk of the substrate.

A study of the luminescence emitted from waveguides containing single static exposures irradiated at different pulse energies, ranging from 12 nJ to 20 nJ, is shown in Fig. 6.8. The two plots in Fig. 6.8 correspond to two sets of waveguides that were processed at pulse energies of 50 nJ and 60 nJ and at 18 μm depth. In both plots, the intensity of the photoluminescence emitted along the waveguides with single static exposures generated at a minimum pulse energy of 12 nJ is greater than for the remaining cases. However, the subsequent photoluminescence emission carrying sufficient intensity is measured for waveguides with static exposures formed at the maximum pulse energy of 20 nJ. Waveguides containing single static exposures fabricated at pulse energies between 14 nJ and 18 nJ are the waveguides that, surprisingly, emit a less intense photoluminescence signal. These results conclude that the pulse energies employed to induce the

formation of vacancies in the diamond lattice do not show any clear effect on the intensity of the photoluminescence signal generated along the waveguides.

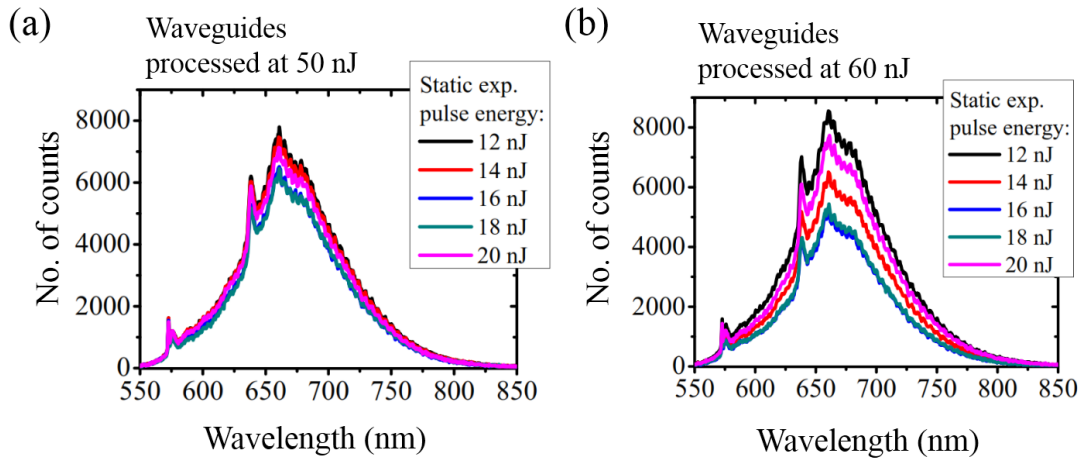

Fig. 6.8: (a) Photoluminescence emission of laser-written waveguides fabricated at 50 nJ pulse energy, containing single static exposures with processing pulse energies ranging between 12 nJ to 20 nJ. (b) Photoluminescence emission of laser-inscribed waveguides fabricated at a pulse energy of 60 nJ, containing single static exposures with processing pulse energies ranging between 12 nJ to 20 nJ. All the waveguide inscriptions were formed at 18 μm depth.

Since no correlation between the pulse energies used to form vacancies along the diamond waveguides and the intensity of the luminescence emission was found, the optical emission of waveguides containing static exposures irradiated at a fixed pulse energy of 16 nJ was studied for waveguides occupying different regions of the same diamond substrate. Fig. 6.9 presents the photoluminescence spectra emitted from different waveguides, containing single static exposures fabricated at 16 nJ, and inscribed within the same diamond sample. The legend of the plot in Fig. 6.9 follows the order of the waveguides distributed in space along the same diamond substrate, indicating the waveguide fabrication depth and the waveguide fabrication pulse energy. A decreasing trend in luminescence intensity can be observed for waveguides spatially distributed throughout the sample, coinciding with a gradual decrease in photoluminescence for waveguides inscribed at greater depths. On the other hand, no influence of the pulse energies used for waveguide fabrications over the intensity of the luminescence signal can be observed.

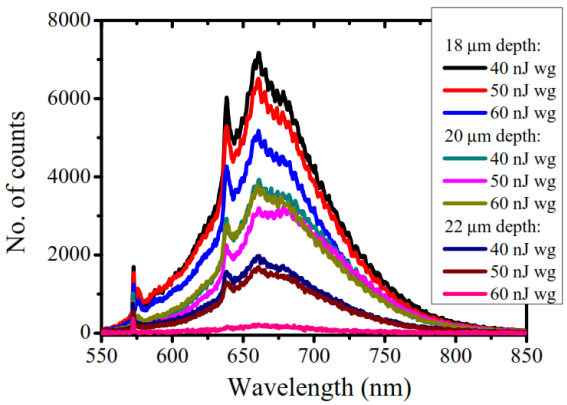

Fig. 6.9: Photoluminescence spectra of waveguides containing single static exposures fabricated at a pulse energy of 16 nJ within the same diamond substrate. The legend of the plot follows the spatial order of the waveguide distribution contained within the substrate, indicating the waveguide fabrication depth and waveguide fabrication pulse energy.

The gradual reduction in photoluminescence intensity following the spatial waveguide distribution inscribed along the substrate suggests that the sample contained an inhomogeneous distribution of intrinsic nitrogen impurities throughout the substrate, with higher nitrogen concentrations located at one of the sample edges and closer to the top surface, since shallower waveguides present enhanced luminescences, and getting reduced towards the central region of the substrate and at deeper locations, with deeper waveguide emitting reduced photoluminescence intensities.

The waveguide layout inscribed within the diamond sample under consideration can be seen in Fig. 6.10 from an overhead optical microscope image. The results obtained from the spectra in Fig. 6.9 can be contrasted with the waveguide positions throughout the sample in Fig. 6.10, where shallow waveguides at 18 μm depth and closer to the sample edge (delimited within a red rectangle in Fig. 6.10) offer enhanced photoluminescence signal (as seen in Fig. 6.9) in comparison with waveguides located closer to the central region of the substrate and placed at slightly deeper positions within the substrate (waveguides delimited within a green rectangle).

Waveguides without single static exposures inscribed in the substrate shown in Fig. 6.10 were also characterized using the free space optics setup described in the previous section. Fig. 6.11

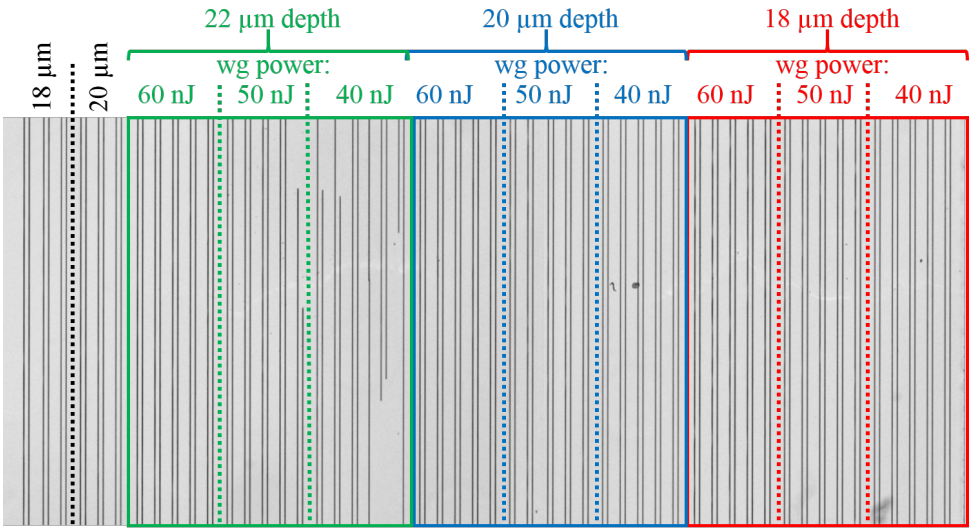

Fig. 6.10: Overhead optical microscope image showing the waveguide layout of the substrate under study. Each subset delimited within red, blue and green rectangles contains five laser inscribed waveguides with single static exposures fabricated at pulse energies ranging from 12 nJ to 20 nJ in steps of 2 nJ, from right to left. The two sets on the left side are composed of three waveguides and no single static exposures were irradiated along them. Some of the waveguides inscribed at 22 μm depth within the green rectangle present discontinuities due to instabilities during laser fabrication.

presents the photoluminescence emitted by waveguides with and without single static exposures contained within the substrate. The legend of the plot indicates the waveguide fabrication depth, the waveguide fabrication pulse energy and the single static exposure fabrication pulse energy for those waveguides containing static exposures. The legent follows the order of the spatial distribution of the waveguides inscribed along the sample. The photoluminescence intensity generated from waveguides with and without static exposures does not seem to follow a general trend, finding in some cases enhanced luminescence intensities coming from waveguides without static exposures in comparison with the pholuminescence generated in waveguides containing single exposures.

All the luminescence results obtained from waveguides inscribed within the same diamond substrate suggest that the photoluminescence intensity is more conditioned by the intrinsic nitrogen impurity concentration distributed at different regions of the diamond substrates which, for the

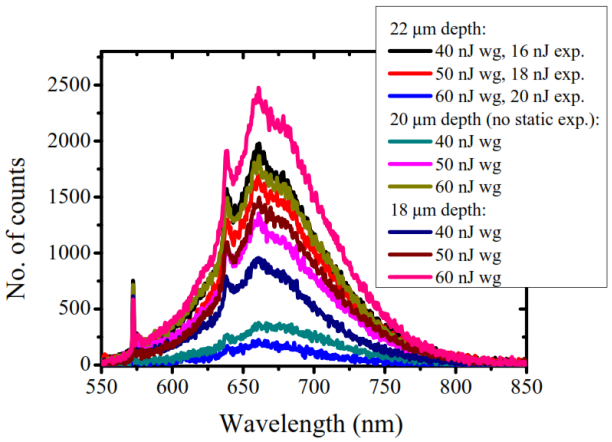

Fig. 6.11: Photoluminescence spectra of waveguides fabricated within the same diamond substrate. The legend follows the order of the waveguide spatial distribution along the sample and indicates the waveguide depth, the waveguide fabrication pulse energy and the static exposure fabrication pulse energy for the case of waveguides containing single exposures.

cases shown in Fig. 6.9 and Fig. 6.10, is larger in regions located near the sample edges and also closer to the top sample surface (shallower waveguides at 18 μm depth seem to emit an enhanced photoluminescence signal in comparison with deeper waveguides). Although a clear enhancement in the photoluminescence signal is obtained for shallow waveguides at 18 μm depth containing static exposures (Fig. 6.9) in comparison with waveguides inscribed within the same substrate at 18 μm depth but without any static exposures (Fig. 6.11), the formation of NV centers and its contribution to an enhancement of the photoluminescence signal is not evident.

To better understand the effect of laser writing within the bulk of HPHT diamond samples, a confocal photoluminescence mapping of the waveguides was performed by our collaborators Belén Sotillo and Andrea Chiappini in Trento, Italy. The optical setup was a Labram Aramis Jobin Yvon Horiba microRaman system with a diode-pumped solid-state laser source opterating at 532 nm wavelength to optically excite the possible NV color centers contained within the diamond substrates. The setup was equipped with a confocal microsocope and an air-cooled CCD. The measurements were taken by focusing a 100$\times$ objective lens onto the sample and the emitted signal was directed to a diffraction grating of 600 l/mm to selectively study the photoluminescence emission at different particular wavelengths.

Results from confocal measurements carried out in HPHT diamond substrates revealed that NV color centers were formed at the spots where single static exposures were intentionally laser written for fabrication pulse energies above 18 nJ. Pulse energies below 18 nJ did not show any visible photoluminescence from confocal maps. Static exposures processed at 30 nJ presented the most enhanced photoluminescence. However, the brightest photoluminescence signal was generated at the vicinity of the two laser damaged lines that compose a single type II waveguide. This bright photoluminescence tends to accumulate on top of the two laser-written lines and it masks the photoluminescence coming from the NV color centers formed within the single static exposures located along the waveguides. This bright photoluminescence coming from a cloud of defects formed at the proximity of the two laser damaged lines explains the reason why the photoluminescence spectra collected from the free space optics setup in Fig. 6.6 did not provide any conclusive results for waveguides containing static exposures at different fabrication energies.

Some of the results obtained from confocal measurements are shown in Fig. 6.12, where the maps correspond to the transverse view of a waveguide in HPHT diamond. The maps correspond to a waveguide containing single static exposures fabricated at 30 nJ pulse energy and placed in a spatial distribution consisting of four lines of single static exposures throughout the waveguide, consecutively spaced by 1 μm along the waveguide and transversely separated by 4 μm. A schematic representation of the transverse distribution of the four static exposures between the two laser-written lines composing the waveguide is illustrated in Fig. 6.12(a). The confocal map in black and white color shown in Fig. 6.12(b) represents the Raman peak intensity of the waveguide cross section and is used as a reference to keep track of the position of the laser written lines composing the type II waveguide. Alongside of the Raman peak intensity map, its corresponding color map indicating the intensity of the emitted light at 637 nm wavelength is found. The two dashed horizontal lines in the maps of Fig. 6.12(b) and 6.12(c) delimit the upper and lower edges of the laser damaged lines composing the type II waveguide. The map reveals a bright photoluminescence emission coming from above the laser damaged lines that form the guiding structures in diamond. There is also a clear evidence of NV color center formation at three out of four sites irradiated with single static exposures, located in between the two laser damaged lines. The closer the NV centers are to the laser-written lines, the lower the emission of these ones.

In conclusion, results from ultrafast laser writing in HPHT diamond samples (with nitrogen

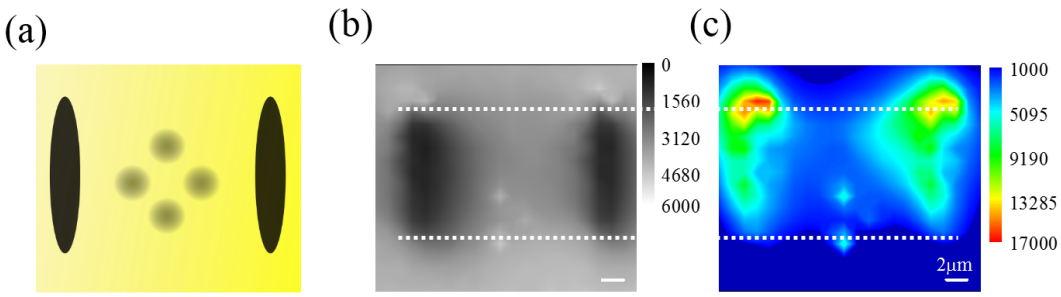

Fig. 6.12: (a) Scheme of the waveguide cross section (b) Raman peak intensity map of a laser-written waveguide in HPHT diamond, centered at 572 nm from an optical excitation at 532 nm wavelength. (c) Photoluminescence emission at 637 nm from the transverse view of the laser-written waveguide in (b). The horizontal dashed lines indicate the top and bottom endings of the two laser damaged lines forming the type II waveguide.

impurity concentrations ∼100 parts per million) reveal that the damage generated by the laser-written lines composing the type II waveguides is creating a cloud of defects that extends into the waveguide region after thermal annealing. Most of the photoluminescence signal is generated from this cloud of defects, rather than coming from the static exposures, and this cloud of defects tends to concentrate on top of the laser-written lines, as it was shown from confocal photoluminescence maps. Since the photoluminescence intensity created by the laser modified lines changes for each waveguide, the photoluminescence signal generated after the thermal treatment is conditioned by the distribution of intrinsic nitrogen defects at different regions of the substrates. From confocal photoluminescence measurements, static exposures at pulse energies below 18 nJ could not be distinguished from the photoluminescence generated at the laser modified lines. The brightest photoluminescence obtained from the sites where static exposures were applied occurred for static exposures fabricated at 30 nJ pulse energy. Moreover, static exposures fabricated closer to the laser modified lines were hardly visible from the confocal maps.

6.7 Summary

This chapter has provided a detailed review of the NV color defect hosted in diamond and the work developed until date in optical guiding structures created in diamond substrates through different fabrication techniques. The importance of having waveguiding within the bulk of diamond has been shown, which can be conveniently realized using femtosecond laser writing. Following some previous work on ultrafast laser writing of waveguides and NV color centers, this technique has been applied in diamond samples containing a high amount of nitrogen impurities, synthesized via the HPHT method for the formation of large ensembles of NV color centers. The laser writing technique was used to create buried type II optical waveguides in diamond and to induce the formation of vacancies throughout the laser-written lines composing the waveguides by irradiation of single femtosecond laser pulses at pulse energies below the amorphization threshold of diamond. A subsequent thermal annealing was performed in order to promote vacancy mobility towards the nitrogen impurities contained in the diamond substrates. The irradiation of single static exposures through the waveguides did not affect any optical properties of the waveguides and single mode optical waveguiding has been reported with optimum insertion losses of 6.8 dB at 635 nm wavelength.

The results obtained from a free space optics photoluminescence characterization setup and from confocal photoluminescence maps revealed that the emission of an intense photoluminescence signal is mostly due to the vacancies produced in the surroundings of the laser damaged lines composing the type II waveguides inscribed in diamond, rather than coming from the sites where the laser static exposures were applied. Also, the intensity of the photoluminescence emitted by the laser modified lines seemed to be highly dependent on the concentration distribution of nitrogen impurities at specific sites of the diamond samples. These results allow to save a fabrication step since no irradiation of single static exposures is needed for the particular case of HPHT diamond to achieve an enhanced photoluminescence, in contrast with ultrafast laser writing employed in diamond substrates with lower nitrogen impurity concentrations [69]. Future experiments will study the effect of using higher pulse energy for the formation of static exposures in order to discriminate the effect of the PL generated by the laser-written lines and the PL generated by the static exposures.

Conclusions and perspectives

The work presented in this thesis has explored direct waveguide fabrication in new material platforms with special characteristics, presenting high nonlinear optical properties and quantum features at room temperature.

In first place, borosilicate glass was chosen as a host platform for waveguide fabrication since it is a well-studied material in laser processing of waveguides and offers a wide transparency window. An optimum processing window for laser writing low-loss waveguides, S-bends and directional couplers has been investigated at 800 nm wavelength for optical circuits presenting compatibility with Ti:Sapphire lasers and SPDC quantum sources. A relatively low pulse broadening effect found in these waveguides enabled the study of the travelling salesman problem, which was implemented into an integrated laser written photonic platform. The novelty here has been the implementation of an optical cross-correlator as a method to study graph theory problems, offering other ways to explore problems that are computationally hard to solve and require high power consumption and exponential growth of computation time with the number of nodes. Femtosecond laser writing offers a flexible tool for fast prototyping as an alternative to usual computational software by means of exploiting three-dimensional parallel patterning. By employing this technique, new emerging platforms may be used for the study of algorithm optimization and new photonic architectures.

In future, new designs containing up to 20 nodes can be fabricated in glass substrates with dimensions of $100 \times 100 \times 1$ mm^3 by distributing the network into two different layers containing 10 nodes each and connecting them through a curved optical waveguide. Under the assumption of

single point detection at the network's output, this type of oracle's decision time, only limited by parallel pulse propagation in the network, will require about 1 ns to find all the existent solutions, while for the case of an electronic computer with 3.6 GHz of clock speed it would take $\sim$6 μs. Moreover, it would be interesting to apply the optical correlation technique used here in silicon waveguides, offering an improvement of the network size.

In second place, a multiscan laser writing approach has enabled the fabrication of low-loss optical waveguides in nonlinear GLS glass, offering single mode guiding at 800 nm wavelength. The performance of the optical circuits as optical switches has been studied and the effect of direct laser writing into nonlinear GLS glass has also been investigated through an estimate of the nonlinear refractive index of the waveguides, inferring that laser-written waveguides in GLS are a suitable platform for nonlinear photonic applications.

In addition, the photorefractivity displayed by GLS glass has been exploited to mimick typical features of a biological neural system in the laser inscribed waveguides. The implementation of laser written waveguides as the basic unit of an all-optical neural network has been demonstrated, including generation of action potentials, excitatory and inhibitory responses, temporal summations and spike-timing dependent plasticity. Laser writing offers a suitable fabrication technique for the development of neuromorphic hardware by optically inscribing photonic circuits in chalcogenide materials.

The novelty of this work opens a path towards the development of scalable all-optical deep neural networks through photonic platforms containing multiple laser-written waveguides connected to each other in a several-layer distribution, offering improved power efficiencies and computational speeds than actual software. Moreover, future perspectives in GLS glass head towards the investigation of phase-change transitions along laser-written optical waveguides, with simultaneous application in non-volatile optical memories and synaptic-like platforms, all embedded into a single chip.

In third place, type II optical waveguiding in bulk diamond substrates containing a high density of nitrogen impurities, grown through a process at high pressure and high temperature, has been achieved. Laser writing has been used as an intermediate process for the formation of NV centers

placed throughout the laser-written waveguides. Photoluminescence results suggested that the origin of a strong photoluminescence signal was coming from the laser-induced lines that compose a type II optical waveguide rather than from the sites where static exposures were applied, allowing to skip one step in the fabrication process. A strong dependence of the photoluminescence intensity with nitrogen impurity distribution along the diamond substrates has been observed.

Femtosecond laser writing has shown a viable fabrication solution to exploit the NV centers located at the bulk of diamond crystals, offering improved ways to optically excite and collect the photoluminescence generated in NVs. Next experiments will explore the effect of irradiating single static exposures throughout the waveguides at slightly higher pulse energies than the ones used in this work, in order to search for better quality laser-induced NVs that allow to discriminate the photoluminescence coming from the two laser-damaged lines of a waveguide. The work shown here goes one step closer towards the integration of laser-written NVs combined with optical circuits for new emerging platforms with applications in quantum information processing and magnetic sensing.

In summary, femtosecond laser writing has been explored as a potential fabrication method for new emerging platforms that are relevant for the study of new optical computing schemes, neuromorphic photonic networks and quantum platforms at room temperatures, offering rapid prototyping and compactness in a single chip.

Published work

- Journal papers:
  - **M. R. Vázquez**, V. Bharadwaj, B. Sotillo, B. Gholipour, R. Ramponi, S. M. Eaton, and C. Soci, "Gallium lanthanum sulfide waveguides as biological axons and synapses," (to be submitted).
  - **M. R. Vázquez**, V. Bharadwaj, and S. M. Eaton, "Diamond quantum computing," *Journal of Optics*, 21(6), p. 063001, 2019.
  - V. Bharadwaj, O. Jedrkiewicz, J. P. Hadden, B. Sotillo, **M. R. Vázquez**, P. Dentella, T. T. Fernandez, A. Chiappini, A. N. Giakoumaki, T. L. Phu, M. Bollani, M. Ferrari, R. Ramponi, P. E. Barclay, and S. M. Eaton, "Femtosecond laser written microfluidic and photonic circuits in diamond," *Journal of Physics: Photonics*, 1(2), p. 022001, 2019.
  - **M. R. Vázquez**, B. Sotillo, S. Rampini, V. Bharadwaj, B.Gholipour, P. Fernández, R. Ramponi, C. Soci, and S. M. Eaton, "Femtosecond laser inscription of nonlinear photonic circuits in Gallium Lanthanum Sulphide glass," *Journal of Physics: Photonics*, 1(1), p. 015006, 2018.
  - **M. R. Vázquez**, V. Bharadwaj, B. Sotillo, S. Z. A. Lo, R. Ramponi, N. I. Zheludev, G. Lanzani, S. M. Eaton, and C. Soci, "Optical NP problem solver on laser-written waveguide platform," *Optics Express*, 26(2), p. 702, 2018.
  - B. Sotillo, A. Chiappini, V. Bharadwaj, **M. Ramos**, T. T. Fernandez, S. Rampini, M. Ferrari, R. Ramponi, P. Fernández, B. Gholipour, and C. Soci, "Raman spectroscopy of femtosecond laser written low propagation loss optical waveguides in Schott N-

SF8 glass," *Optical Materials*, 72, p. 626, 2017.

- Book chapters:

  – S. M. Eaton, B. Sotillo, T. T. Fernandez, V. Bharadwaj, A. N. Giakoumaki, **M. Ramos Vázquez**, A. Ancona, R. Osellame, and R. Ramponi, "Femtosecond laser writing of optical structures in glasses" (under review).

Conferences

- V. Bharadwaj, J. P. Hadden, **M. R. Vázquez**, A. N. Giakoumaki, O. Jedrkiewicz, B. Sotillo, T. L. Phu, P. E. Barclay, R. Ramponi, and S. M. Eaton, "Femtosecond laser inscription of integrated diamond quantum photonics for quantum information and sensing," *CLEO Conference 2019*, Munich, Germany.

- V. Bharadwaj, B. Sotillo, A. Giakoumaki, T. Le Phu, **M. Ramos**, O. Jedrkiewicz, R. Osellame, T. T. Fernandez, J. P. Hadden, A. Chiappini, M. Ferrari, P. E. Barclay, R. Ramponi, P. S. Salter, and S. M. Eaton, "Femtosecond laser inscribed color centers, microfluidics and photonics in single-crystal diamond". *SPIE Photonics West 2018*, San Francisco, USA.

- B. Sotillo, V. Bharadwaj, T. T. Fernandez, **M. Ramos**, J. P. Hadden, A. Chiappini, M. Ferrari, R. Osellame, G. Galzerano, P. E. Barclay, R. Ramponi, P. S. Salter, and S. M. Eaton, "Femtosecond laser written diamond photonics". *Advanced Photonics Congress 2018*, Zurich, Switzerland.

- **M. Ramos**, V. Bharadwaj, B. Sotillo, G. Galzerano, B. Gholipour, S. M. Eaton, C. Soci, "All-optical intra and inter neuronal communication protocol platform". *Advanced Photonics Congress 2018*, Zurich, Switzerland.

- **M. R. Vázquez**, V. Bharadwaj, B. Sotillo, S. Z. A. Lo, R. Ramponi, N. Zheludev, S. Eaton, and C. Soci, "Laser-written Waveguide Network as Optical Oracle," *IPS Meeting 2017*, Singapore.

- **M. R. Vázquez**, V. Bharadwaj, B. Sotillo, D. M. Nguyen, S. M. Eaton, and C. Soci, "Implementation of optical oracle in laser written waveguide network", *IPS Meeting 2016*, Singapore (poster presentation).

Bibliography

[1] R. R. Gattass and E. Mazur, "Femtosecond laser micromachining in transparent materials," *Nature Photonics*, vol. 2, no. 4, p. 219, 2008.

[2] R. Mildren and J. Rabeau, *Optical engineering of diamond*. John Wiley & Sons, 2013.

[3] D. W. Hewak, D. Brady, R. J. Curry, G. Elliott, C.-C. Huang, M. Hughes, K. Knight, A. Mairaj, M. Petrovich, R. Simpson, *et al.*, "Chalcogenide glasses for photonics device applications," *Photonic glasses and glass-ceramics*, p. 29, 2010.

[4] M. Petrovich, *Gallium lanthanum sulphide glasses for near-infrared photonic applications*. PhD thesis, University of Southampton, 2003.

[5] N. P. Bansal and R. H. Doremus, *Handbook of glass properties*. Elsevier, 2013.

[6] R. Osellame, G. Cerullo, and R. Ramponi, *Femtosecond laser micromachining: photonic and microfluidic devices in transparent materials*, vol. 123. Springer Science & Business Media, 2012.

[7] G. Stitt, R. Lysecky, and F. Vahid, "Dynamic hardware/software partitioning: a first approach," in *Proceedings of the 40th Annual Design Automation Conference*, p. 250, ACM, 2003.

[8] J. I. Cirac and P. Zoller, "Quantum computations with cold trapped ions," *Physical Review Letters*, vol. 74, no. 20, p. 4091, 1995.

[9] S. Chu, "Cold atoms and quantum control," *Nature*, vol. 416, no. 6877, p. 206, 2002.

[10] S. Hudgens and B. Johnson, "Overview of phase-change chalcogenide nonvolatile memory technology," *MRS Bulletin*, vol. 29, no. 11, p. 829, 2004.

[11] Z. Cheng, C. Ríos, W. H. Pernice, C. D. Wright, and H. Bhaskaran, "On-chip photonic synapse," *Science Advances*, vol. 3, no. 9, p. e1700160, 2017.

[12] G. Balasubramanian, P. Neumann, D. Twitchen, M. Markham, R. Kolesov, N. Mizuochi, J. Isoya, J. Achard, J. Beck, J. Tissler, *et al.*, "Ultralong spin coherence time in isotopically engineered diamond," *Nature Materials*, vol. 8, no. 5, p. 383, 2009.

[13] D. Du, X. Liu, G. Korn, J. Squier, and G. Mourou, "Laser-induced breakdown by impact ionization in SiO_2 with pulse widths from 7 ns to 150 fs," *Applied Physics Letters*, vol. 64, no. 23, p. 3071, 1994.

[14] K. M. Davis, K. Miura, N. Sugimoto, and K. Hirao, "Writing waveguides in glass with a femtosecond laser," *Optics Letters*, vol. 21, no. 21, p. 1729, 1996.

[15] K. K. Seet, V. Mizeikis, S. Matsuo, S. Juodkazis, and H. Misawa, "Three-dimensional spiral-architecture photonic crystals obtained by direct laser writing," *Advanced Materials*, vol. 17, no. 5, p. 541, 2005.

[16] S. M. Eaton, C. De Marco, R. Martinez-Vazquez, R. Ramponi, S. Turri, G. Cerullo, and R. Osellame, "Femtosecond laser microstructuring for polymeric lab-on-chips," *Journal of Biophotonics*, vol. 5, no. 8-9, p. 687, 2012.

[17] C. Hnatovsky, R. Taylor, E. Simova, P. Rajeev, D. Rayner, V. Bhardwaj, and P. Corkum, "Fabrication of microchannels in glass using focused femtosecond laser radiation and selective chemical etching," *Applied Physics A*, vol. 84, no. 1-2, p. 47, 2006.

[18] M. Farsari and B. N. Chichkov, "Materials processing: Two-photon fabrication," *Nature Photonics*, vol. 3, no. 8, p. 450, 2009.

[19] S. M. Eaton, H. Zhang, P. R. Herman, F. Yoshino, L. Shah, J. Bovatsek, and A. Y. Arai, "Heat accumulation effects in femtosecond laser-written waveguides with variable repetition rate," *Optics Express*, vol. 13, no. 12, p. 4708, 2005.

[20] A. M. Streltsov and N. F. Borrelli, "Study of femtosecond-laser-written waveguides in glasses," *JOSA B*, vol. 19, no. 10, p. 2496, 2002.

[21] D. Homoelle, S. Wielandy, A. L. Gaeta, N. Borrelli, and C. Smith, "Infrared photosensitivity in silica glasses exposed to femtosecond laser pulses," *Optics Letters*, vol. 24, no. 18, p. 1311, 1999.

[22] G. Della Valle, R. Osellame, and P. Laporta, "Micromachining of photonic devices by femtosecond laser pulses," *Journal of Optics A: Pure and Applied Optics*, vol. 11, no. 1, p. 013001, 2008.

[23] S. Nolte, M. Will, J. Burghoff, and A. Tuennermann, "Femtosecond waveguide writing: a new avenue to three-dimensional integrated optics," *Applied Physics A*, vol. 77, no. 1, p. 109, 2003.

[24] J. Liu, Z. Zhang, S. Chang, C. Flueraru, and C. P. Grover, "Directly writing of 1-to-N optical waveguide power splitters in fused silica glass using a femtosecond laser," *Optics Communications*, vol. 253, no. 4-6, p. 315, 2005.

[25] M. Sakakura, T. Sawano, Y. Shimotsuma, K. Miura, and K. Hirao, "Fabrication of three-dimensional 1×4 splitter waveguides inside a glass substrate with spatially phase modulated laser beam," *Optics Express*, vol. 18, no. 12, p. 12136, 2010.

[26] A. M. Streltsov and N. F. Borrelli, "Fabrication and analysis of a directional coupler written in glass by nanojoule femtosecond laser pulses," *Optics Letters*, vol. 26, no. 1, p. 42, 2001.

[27] W. Watanabe, T. Asano, K. Yamada, K. Itoh, and J. Nishii, "Wavelength division with three-dimensional couplers fabricated by filamentation of femtosecond laser pulses," *Optics Letters*, vol. 28, no. 24, p. 2491, 2003.

[28] K. Minoshima, A. M. Kowalevicz, E. P. Ippen, and J. G. Fujimoto, "Fabrication of coupled mode photonic devices in glass by nonlinear femtosecond laser materials processing," *Optics Express*, vol. 10, no. 15, p. 645, 2002.

[29] R. Osellame, V. Maselli, N. Chiodo, D. Polli, R. M. Vazquez, R. Ramponi, and G. Cerullo, "Fabrication of 3D photonic devices at 1.55 μm wavelength by femtosecond Ti: Sapphire oscillator," *Electronics Letters*, vol. 41, no. 6, p. 315, 2005.

[30] S. M. Eaton, W.-J. Chen, H. Zhang, R. Iyer, J. Li, M. L. Ng, S. Ho, J. S. Aitchison, and P. R. Herman, "Spectral loss characterization of femtosecond laser written waveguides in glass with application to demultiplexing of 1300 and 1550 nm wavelengths," *Journal of Lightwave Technology*, vol. 27, no. 9, p. 1079, 2009.

[31] L. Sansoni, F. Sciarrino, G. Vallone, P. Mataloni, A. Crespi, R. Ramponi, and R. Osellame, "Polarization entangled state measurement on a chip," *Physical Review Letters*, vol. 105, no. 20, p. 200503, 2010.

[32] K. Suzuki, V. Sharma, J. G. Fujimoto, E. P. Ippen, and Y. Nasu, "Characterization of symmetric [3×3] directional couplers fabricated by direct writing with a femtosecond laser oscillator," *Optics Express*, vol. 14, no. 6, p. 2335, 2006.

[33] Y. Lai, K. Zhou, K. Sugden, and I. Bennion, "Point-by-point inscription of first-order fiber Bragg grating for C-band applications," *Optics Express*, vol. 15, no. 26, p. 18318, 2007.

[34] A. Kowalevicz, V. Sharma, E. Ippen, J. G. Fujimoto, and K. Minoshima, "Three-dimensional photonic devices fabricated in glass by use of a femtosecond laser oscillator," *Optics Letters*, vol. 30, no. 9, p. 1060, 2005.

[35] A. Crespi, Y. Gu, B. Ngamsom, H. J. Hoekstra, C. Dongre, M. Pollnau, R. Ramponi, H. H. van den Vlekkert, P. Watts, G. Cerullo, *et al.*, "Three-dimensional Mach-Zehnder interferometer in a microfluidic chip for spatially-resolved label-free detection," *Lab on a Chip*, vol. 10, no. 9, p. 1167, 2010.

[36] M. Will, S. Nolte, B. N. Chichkov, and A. Tünnermann, "Optical properties of waveguides fabricated in fused silica by femtosecond laser pulses," *Applied Optics*, vol. 41, no. 21, p. 4360, 2002.

[37] C. Florea and K. A. Winick, "Fabrication and characterization of photonic devices directly written in glass using femtosecond laser pulses," *Journal of Lightwave Technology*, vol. 21, no. 1, p. 246, 2003.

[38] R. Osellame, N. Chiodo, V. Maselli, A. Yin, M. Zavelani-Rossi, G. Cerullo, P. Laporta, L. Aiello, S. De Nicola, P. Ferraro, *et al.*, "Optical properties of waveguides written by a 26 MHz stretched cavity Ti:Sapphire femtosecond oscillator," *Optics Express*, vol. 13, no. 2, p. 612, 2005.

[39] L. Shah, A. Y. Arai, S. M. Eaton, and P. R. Herman, "Waveguide writing in fused silica with a femtosecond fiber laser at 522 nm and 1 MHz repetition rate," *Optics Express*, vol. 13, no. 6, p. 1999, 2005.

[40] H. Zhang, S. M. Eaton, and P. R. Herman, "Low-loss type II waveguide writing in fused silica with single picosecond laser pulses," *Optics Express*, vol. 14, no. 11, p. 4826, 2006.

[41] L. Tong, R. R. Gattass, I. Maxwell, J. B. Ashcom, and E. Mazur, "Optical loss measurements in femtosecond laser written waveguides in glass," *Optics communications*, vol. 259, no. 2, p. 626, 2006.

[42] M. R. Vázquez, V. Bharadwaj, B. Sotillo, S.-Z. A. Lo, R. Ramponi, N. I. Zheludev, G. Lanzani, S. M. Eaton, and C. Soci, "Optical NP problem solver on laser-written waveguide platform," *Optics Express*, vol. 26, no. 2, p. 702, 2018.

[43] A. Crespi, R. Osellame, R. Ramponi, D. J. Brod, E. F. Galvao, N. Spagnolo, C. Vitelli, E. Maiorino, P. Mataloni, and F. Sciarrino, "Integrated multimode interferometers with arbitrary designs for photonic boson sampling," *Nature Photonics*, vol. 7, no. 7, p. 545, 2013.

[44] M. Tillmann, B. Dakić, R. Heilmann, S. Nolte, A. Szameit, and P. Walther, "Experimental boson sampling," *Nature Photonics*, vol. 7, no. 7, p. 540, 2013.

[45] N. Spagnolo, C. Vitelli, M. Bentivegna, D. J. Brod, A. Crespi, F. Flamini, S. Giacomini, G. Milani, R. Ramponi, P. Mataloni, *et al.*, "Experimental validation of photonic boson sampling," *Nature Photonics*, vol. 8, no. 8, p. 615, 2014.

[46] A. Crespi, R. Ramponi, R. Osellame, L. Sansoni, I. Bongioanni, F. Sciarrino, G. Vallone, and P. Mataloni, "Integrated photonic quantum gates for polarization qubits," *Nature Communications*, vol. 2, p. 566, 2011.

[47] M. Hughes, W. Yang, and D. Hewak, "Fabrication and characterization of femtosecond laser written waveguides in chalcogenide glass," *Applied Physics Letters*, vol. 90, no. 13, p. 131113, 2007.

[48] O. Efimov, L. Glebov, K. Richardson, E. Van Stryland, T. Cardinal, S. Park, M. Couzi, and J. Bruneel, "Waveguide writing in chalcogenide glasses by a train of femtosecond laser pulses," *Optical Materials*, vol. 17, no. 3, p. 379, 2001.

[49] B. McMillen, B. Zhang, K. P. Chen, A. Benayas, and D. Jaque, "Ultrafast laser fabrication of low-loss waveguides in chalcogenide glass with 0.65 dB/cm loss," *Optics Letters*, vol. 37, no. 9, p. 1418, 2012.

[50] N. Hô, M. C. Phillips, H. Qiao, P. J. Allen, K. Krishnaswami, B. J. Riley, T. L. Myers, and N. C. Anheier, "Single-mode low-loss chalcogenide glass waveguides for the mid-infrared," *Optics Letters*, vol. 31, no. 12, p. 1860, 2006.

[51] G. Demetriou, J.-P. Bérubé, R. Vallée, Y. Messaddeq, C. R. Petersen, D. Jain, O. Bang, C. Craig, D. W. Hewak, and A. K. Kar, "Refractive index and dispersion control of ultrafast laser inscribed waveguides in gallium lanthanum sulphide for near and mid-infrared applications," *Optics Express*, vol. 24, no. 6, p. 6350, 2016.

[52] A. Zakery and S. Elliott, "Optical properties and applications of chalcogenide glasses: a review," *Journal of Non-Crystalline Solids*, vol. 330, no. 1-3, p. 1, 2003.

[53] G. Demetriou, D. W. Hewak, A. Ravagli, C. Craig, and A. Kar, "Nonlinear refractive index of ultrafast laser inscribed waveguides in gallium lanthanum sulphide," *Applied Optics*, vol. 56, no. 19, p. 5407, 2017.

[54] N. D. Psaila, R. R. Thomson, H. T. Bookey, S. Shen, N. Chiodo, R. Osellame, G. Cerullo, A. Jha, and A. K. Kar, "Supercontinuum generation in an ultrafast laser inscribed chalcogenide glass waveguide," *Optics Express*, vol. 15, no. 24, p. 15776, 2007.

[55] M. A. Hughes, W. Yang, and D. W. Hewak, "Spectral broadening in femtosecond laser written waveguides in chalcogenide glass," *JOSA B*, vol. 26, no. 7, p. 1370, 2009.

[56] J. E. McCarthy, H. T. Bookey, N. D. Psaila, R. R. Thomson, and A. K. Kar, "Mid-infrared spectral broadening in an ultrafast laser inscribed gallium lanthanum sulphide waveguide," *Optics Express*, vol. 20, no. 2, p. 1545, 2012.

[57] M. Wuttig and N. Yamada, "Phase-change materials for rewriteable data storage," *Nature Materials*, vol. 6, no. 11, p. 824, 2007.

[58] S. Raoux, F. Xiong, M. Wuttig, and E. Pop, "Phase change materials and phase change memory," *MRS Bulletin*, vol. 39, no. 8, p. 703, 2014.

[59] T. Gorelik, M. Will, S. Nolte, A. Tuennermann, and U. Glatzel, "Transmission electron microscopy studies of femtosecond laser induced modifications in quartz," *Applied Physics A*, vol. 76, no. 3, p. 309, 2003.

[60] A. H. Nejadmalayeri, P. R. Herman, J. Burghoff, M. Will, S. Nolte, and A. Tünnermann, "Inscription of optical waveguides in crystalline silicon by mid-infrared femtosecond laser pulses," *Optics Letters*, vol. 30, no. 9, p. 964, 2005.

[61] F. Dreisow, J. Thomas, J. Burghoff, A. Ancona, M. Heinrich, S. Nolte, and A. Tunnermann, "Efficient frequency doubling in fs-laser written waveguides in PPLN and BBO," *SPIE 425 Photonics West/LASE*, 2008.

[62] L. Gui, B. Xu, and T. C. Chong, "Microstructure in lithium niobate by use of focused femtosecond laser pulses," *IEEE Photonics Technology Letters*, vol. 16, no. 5, p. 1337, 2004.

[63] R. Osellame, M. Lobino, N. Chiodo, M. Marangoni, G. Cerullo, R. Ramponi, H. T. Bookey, R. R. Thomson, N. D. Psaila, and A. K. Kar, "Femtosecond laser writing of waveguides in periodically poled lithium niobate preserving the nonlinear coefficient," *Applied Physics Letters*, vol. 90, no. 24, p. 241107, 2007.

[64] J. Burghoff, C. Grebing, S. Nolte, and A. Tünnermann, "Waveguides in lithium niobate fabricated by focused ultrashort laser pulses," *Applied Surface Science*, vol. 253, no. 19, p. 7899, 2007.

[65] J. Thomas, M. Heinrich, J. Burghoff, S. Nolte, A. Ancona, and A. Tünnermann, "Femtosecond laser-written quasi-phase-matched waveguides in lithium niobate," *Applied Physics Letters*, vol. 91, no. 15, p. 151108, 2007.

[66] R. He, Q. An, Y. Jia, G. R. Castillo-Vega, J. R. V. de Aldana, and F. Chen, "Femtosecond laser micromachining of lithium niobate depressed cladding waveguides," *Optical Materials Express*, vol. 3, no. 9, p. 1378, 2013.

[67] P. Karpinski, V. Shvedov, W. Krolikowski, and C. Hnatovsky, "Laser-writing inside uniaxially birefringent crystals: fine morphology of ultrashort pulse-induced changes in lithium niobate," *Optics Express*, vol. 24, no. 7, p. 7456, 2016.

[68] J. Hadden, B. Sotillo, V. Bharadwaj, S. Rampini, F. Bosia, F. Picollo, M. Sakakura, A. Chiappini, T. T. Fernandez, R. Osellame, *et al.*, "Bulk diamond optical waveguides fabricated by focused femtosecond laser pulses," in *Laser 3D Manufacturing IV*, vol. 10095, p. 100950Q, International Society for Optics and Photonics, 2017.

[69] J. Hadden, V. Bharadwaj, B. Sotillo, S. Rampini, R. Osellame, J. Witmer, H. Jayakumar, T. Fernandez, A. Chiappini, C. Armellini, *et al.*, "Integrated waveguides and deterministically positioned nitrogen vacancy centers in diamond created by femtosecond laser writing," *Optics Letters*, vol. 43, no. 15, p. 3586, 2018.

[70] C. Cheng, C. Romero, F. Chen, *et al.*, "Superficial waveguide splitters fabricated by femtosecond laser writing of $LiTaO_3$ crystal," *Optical Engineering*, vol. 54, no. 6, p. 067113, 2015.

[71] B. McMillen, K. P. Chen, and D. Jaque, "Microstructural imaging of high repetition rate ultrafast laser written $LiTaO_3$ waveguides," *Applied Physics Letters*, vol. 94, no. 8, p. 081106, 2009.

[72] K.-i. Kawamura, M. Hirano, T. Kamiya, and H. Hosono, "Femtosecond-laser-encoded distributed-feedback color center laser in lithium fluoride single crystal," *Journal of Non-crystalline Solids*, vol. 352, no. 23-25, p. 2347, 2006.

[73] F. Chen and J. V. de Aldana, "Optical waveguides in crystalline dielectric materials produced by femtosecond-laser micromachining," *Laser & Photonics Reviews*, vol. 8, no. 2, p. 251, 2014.

[74] J. Burghoff, C. Grebing, S. Nolte, and A. Tünnermann, "Efficient frequency doubling in femtosecond laser-written waveguides in lithium niobate," *Applied Physics Letters*, vol. 89, no. 8, p. 081108, 2006.

[75] N. Dong, F. Chen, and J. Vázquez de Aldana, "Efficient second harmonic generation by birefringent phase matching in femtosecond-laser-inscribed KTP cladding waveguides," *Physica Status Solidi (RRL)–Rapid Research Letters*, vol. 6, no. 7, p. 306, 2012.

[76] S. Zhang, J. Yao, Q. Shi, Y. Liu, W. Liu, Z. Huang, F. Lu, and E. Li, "Fabrication and characterization of periodically poled lithium niobate waveguide using femtosecond laser pulses," *Applied Physics Letters*, vol. 92, no. 23, p. 231106, 2008.

[77] Z. Huang, C. Tu, S. Zhang, Y. Li, F. Lu, Y. Fan, and E. Li, "Femtosecond second-harmonic generation in periodically poled lithium niobate waveguides written by femtosecond laser pulses," *Optics Letters*, vol. 35, no. 6, p. 877, 2010.

[78] Y. Jia, J. R. V. de Aldana, C. Romero, Y. Ren, Q. Lu, and F. Chen, "Femtosecond-laser-inscribed BiB_3O_6 nonlinear cladding waveguide for second-harmonic generation," *Applied Physics Express*, vol. 5, no. 7, p. 072701, 2012.

[79] S. Campbell, R. Thomson, D. Hand, A. Kar, D. Reid, C. Canalias, V. Pasiskevicius, and F. Laurell, "Frequency-doubling in femtosecond laser inscribed periodically-poled potassium titanyl phosphate waveguides," *Optics Express*, vol. 15, no. 25, p. 17146, 2007.

[80] Y. Liao, J. Xu, Y. Cheng, Z. Zhou, F. He, H. Sun, J. Song, X. Wang, Z. Xu, K. Sugioka, *et al.*, "Electro-optic integration of embedded electrodes and waveguides in $LiNbO_3$ using a femtosecond laser," *Optics Letters*, vol. 33, no. 19, p. 2281, 2008.

[81] J. Thomas, M. Heinrich, P. Zeil, V. Hilbert, K. Rademaker, R. Riedel, S. Ringleb, C. Dubs, J.-P. Ruske, S. Nolte, *et al.*, "Laser direct writing: Enabling monolithic and hybrid integrated solutions on the lithium niobate platform," *Physica Status Solidi (a)*, vol. 208, no. 2, p. 276, 2011.

[82] S. Ringleb, K. Rademaker, S. Nolte, and A. Tünnermann, "Monolithically integrated optical frequency converter and amplitude modulator in $LiNbO_3$ fabricated by femtosecond laser pulses," *Applied Physics B*, vol. 102, no. 1, p. 59, 2011.

[83] W. Horn, S. Kroesen, J. Herrmann, J. Imbrock, and C. Denz, "Electro-optical tunable waveguide Bragg gratings in lithium niobate induced by femtosecond laser writing," *Optics Express*, vol. 20, no. 24, p. 26922, 2012.

[84] Y. Sikorski, A. Said, P. Bado, R. Maynard, C. Florea, and K. Winick, "Optical waveguide amplifier in Nd-doped glass written with near-Ir femtosecond laser pulses," *Electronics Letters*, vol. 36, no. 3, p. 226, 2000.

[85] S. Taccheo, G. Della Valle, R. Osellame, G. Cerullo, N. Chiodo, P. Laporta, O. Svelto, A. Killi, U. Morgner, M. Lederer, *et al.*, "Er:Yb-doped waveguide laser fabricated by femtosecond laser pulses," *Optics Letters*, vol. 29, no. 22, p. 2626, 2004.

[86] R. Osellame, N. Chiodo, G. Della Valle, G. Cerullo, R. Ramponi, P. Laporta, A. Killi, U. Morgner, and O. Svelto, "Waveguide lasers in the C-band fabricated by laser inscription with a compact femtosecond oscillator," *IEEE Journal of Selected Topics in Quantum Electronics*, vol. 12, no. 2, p. 277, 2006.

[87] G. Della Valle, R. Osellame, N. Chiodo, S. Taccheo, G. Cerullo, P. Laporta, A. Killi, U. Morgner, M. Lederer, and D. Kopf, "C-band waveguide amplifier produced by femtosecond laser writing," *Optics Express*, vol. 13, no. 16, p. 5976, 2005.

[88] N. Psaila, R. Thomson, H. Bookey, N. Chiodo, S. Shen, R. Osellame, G. Cerullo, A. Jha, and A. Kar, "Er:Yb-doped oxyfluoride silicate glass waveguide laser fabricated using ultrafast laser inscription," *IEEE Photonics Technology Letters*, vol. 20, no. 2, p. 126, 2008.

[89] Y. Tan, F. Chen, J. Vázquez de Aldana, G. Torchia, A. Benayas, and D. Jaque, "Continuous wave laser generation at 1064 nm in femtosecond laser inscribed Nd:YVO_4 channel waveguides," *Applied Physics Letters*, vol. 97, no. 3, p. 031119, 2010.

[90] G. Della Valle, R. Osellame, G. Galzerano, N. Chiodo, G. Cerullo, P. Laporta, O. Svelto, U. Morgner, A. Rozhin, V. Scardaci, *et al.*, "Passive mode locking by carbon nanotubes in a femtosecond laser written waveguide laser," *Applied Physics Letters*, vol. 89, no. 23, p. 231115, 2006.

[91] N. Dong, J. Martínez de Mendivil, E. Cantelar, G. Lifante, J. Vazquez de Aldana, G. A. Torchia, F. Chen, and D. Jaque, "Self-frequency-doubling of ultrafast laser inscribed neodymium doped yttrium aluminum borate waveguides," *Applied Physics Letters*, vol. 98, no. 18, p. 181103, 2011.

[92] Y. Ren, F. Chen, and J. R. V. de Aldana, "Near-infrared lasers and self-frequency-doubling in Nd:YCOB cladding waveguides," *Optics Express*, vol. 21, no. 9, p. 11562, 2013.

[93] Y. Ren, G. Brown, A. Ródenas, S. Beecher, F. Chen, and A. K. Kar, "Mid-infrared waveguide lasers in rare-earth-doped YAG," *Optics Letters*, vol. 37, no. 16, p. 3339, 2012.

[94] M. Ams, P. Dekker, G. D. Marshall, and M. J. Withford, "Monolithic 100 mW Yb waveguide laser fabricated using the femtosecond-laser direct-write technique," *Optics Letters*, vol. 34, no. 3, p. 247, 2009.

[95] G. Torchia, A. Rodenas, A. Benayas, E. Cantelar, L. Roso, and D. Jaque, "Highly efficient laser action in femtosecond-written Nd:yttrium aluminum garnet ceramic waveguides," *Applied Physics Letters*, vol. 92, no. 11, p. 111103, 2008.

[96] T. Calmano, J. Siebenmorgen, O. Hellmig, K. Petermann, and G. Huber, "Nd:YAG waveguide laser with 1.3 W output power, fabricated by direct femtosecond laser writing," *Applied Physics B*, vol. 100, no. 1, p. 131, 2010.

[97] J. Siebenmorgen, T. Calmano, K. Petermann, and G. Huber, "Highly efficient Yb:YAG channel waveguide laser written with a femtosecond-laser," *Optics Express*, vol. 18, no. 15, p. 16035, 2010.

[98] G. Della Valle, S. Taccheo, R. Osellame, A. Festa, G. Cerullo, and P. Laporta, "1.5 μm single longitudinal mode waveguide laser fabricated by femtosecond laser writing," *Optics Express*, vol. 15, no. 6, p. 3190, 2007.

[99] J. del Hoyo, P. Moreno-Zárate, G. Escalante, J. A. Vallés, P. Fernández, and J. Solís, "High-efficiency waveguide optical amplifiers and lasers via fs-laser induced local modification of the glass composition," *Journal of Lightwave Technology*, vol. 35, no. 14, p. 2955, 2017.

[100] C. Grivas, C. Corbari, G. Brambilla, and P. G. Lagoudakis, "Tunable, continuous-wave Ti:Sapphire channel waveguide lasers written by femtosecond and picosecond laser pulses," *Optics Letters*, vol. 37, no. 22, p. 4630, 2012.

[101] A. Okhrimchuk, A. Shestakov, I. Khrushchev, and J. Mitchell, "Depressed cladding, buried waveguide laser formed in a YAG:Nd^{3+} crystal by femtosecond laser writing," *Optics Letters*, vol. 30, no. 17, p. 2248, 2005.

[102] A. Benayas, W. Silva, A. Ródenas, C. Jacinto, J. V. de Aldana, F. Chen, Y. Tan, R. Thomsom, N. Psaila, D. Reid, *et al.*, "Ultrafast laser writing of optical waveguides in ceramic Yb:YAG: a study of thermal and non-thermal regimes," *Applied Physics A*, vol. 104, no. 1, p. 301, 2011.

[103] A. Benayas, W. Silva, C. Jacinto, E. Cantelar, J. Lamela, F. Jaque, J. V. de Aldana, G. Torchia, L. Roso, A. Kaminskii, *et al.*, "Thermally resistant waveguides fabricated in Nd:YAG ceramics by crossing femtosecond damage filaments," *Optics Letters*, vol. 35, no. 3, p. 330, 2010.

[104] H. Liu, Y. Jia, J. R. V. de Aldana, D. Jaque, and F. Chen, "Femtosecond laser inscribed cladding waveguides in Nd:YAG ceramics: Fabrication, fluorescence imaging and laser performance," *Optics Express*, vol. 20, no. 17, p. 18620, 2012.

[105] Y. Tan, A. Rodenas, F. Chen, R. R. Thomson, A. K. Kar, D. Jaque, and Q. Lu, "70% slope efficiency from an ultrafast laser-written Nd:$GdVO_4$ channel waveguide laser," *Optics Express*, vol. 18, no. 24, p. 24994, 2010.

[106] G. Corrielli, A. Seri, M. Mazzera, R. Osellame, and H. de Riedmatten, "Integrated optical memory based on laser-written waveguides," *Physical Review Applied*, vol. 5, no. 5, p. 054013, 2016.

[107] T. Shih, R. R. Gattass, C. R. Mendonca, and E. Mazur, "Faraday rotation in femtosecond laser micromachined waveguides," *Optics Express*, vol. 15, no. 9, p. 5809, 2007.

[108] S. Sowa, W. Watanabe, T. Tamaki, J. Nishii, and K. Itoh, "Symmetric waveguides in poly (methyl methacrylate) fabricated by femtosecond laser pulses," *Optics Express*, vol. 14, no. 1, p. 291, 2006.

[109] B. Sotillo, V. Bharadwaj, J. Hadden, M. Sakakura, A. Chiappini, T. T. Fernandez, S. Longhi, O. Jedrkiewicz, Y. Shimotsuma, L. Criante, *et al.*, "Diamond photonics platform enabled by femtosecond laser writing," *Scientific Reports*, vol. 6, p. 35566, 2016.

[110] A. W. Schell, J. Kaschke, J. Fischer, R. Henze, J. Wolters, M. Wegener, and O. Benson, "Three-dimensional quantum photonic elements based on single nitrogen vacancy-centres in laser-written microstructures," *Scientific Reports*, vol. 3, p. 1577, 2013.

[111] R. Schirhagl, K. Chang, M. Loretz, and C. L. Degen, "Nitrogen-vacancy centers in diamond: nanoscale sensors for physics and biology," *Annual Review of Physical Chemistry*, vol. 65, p. 83, 2014.

[112] B. Sotillo, V. Bharadwaj, J. P. Hadden, S. Rampini, A. Chiappini, T. T. Fernandez, C. Armellini, A. Serpengüzel, M. Ferrari, P. E. Barclay, *et al.*, "Visible to infrared diamond photonics enabled by focused femtosecond laser pulses," *Micromachines*, vol. 8, no. 2, p. 60, 2017.

[113] A. Szameit and S. Nolte, "Discrete optics in femtosecond-laser-written photonic structures," *Journal of Physics B: Atomic, Molecular and Optical Physics*, vol. 43, no. 16, p. 163001, 2010.

[114] A. Yariv, "Coupled-mode theory for guided-wave optics," *IEEE Journal of Quantum Electronics*, vol. 9, no. 9, p. 919, 1973.

[115] J. Noh, S. Huang, D. Leykam, Y. D. Chong, K. P. Chen, and M. C. Rechtsman, "Experimental observation of optical Weyl points and Fermi arc-like surface states," *Nature Physics*, vol. 13, no. 6, p. 611, 2017.

[116] S. Mao, F. Quéré, S. Guizard, X. Mao, R. Russo, G. Petite, and P. Martin, "Dynamics of femtosecond laser interactions with dielectrics," *Applied Physics A*, vol. 79, no. 7, p. 1695, 2004.

[117] C. B. Schaffer, A. Brodeur, and E. Mazur, "Laser-induced breakdown and damage in bulk transparent materials induced by tightly focused femtosecond laser pulses," *Measurement Science and Technology*, vol. 12, no. 11, p. 1784, 2001.

[118] S. Sundaram and E. Mazur, "Inducing and probing non-thermal transitions in semiconductors using femtosecond laser pulses," *Nature Materials*, vol. 1, no. 4, p. 217, 2002.

[119] J. W. Chan, T. Huser, S. Risbud, and D. Krol, "Structural changes in fused silica after exposure to focused femtosecond laser pulses," *Optics Letters*, vol. 26, no. 21, p. 1726, 2001.

[120] V. R. Bhardwaj, E. Simova, P. Corkum, D. Rayner, C. Hnatovsky, R. Taylor, B. Schreder, M. Kluge, and J. Zimmer, "Femtosecond laser-induced refractive index modification in multicomponent glasses," *Journal of Applied Physics*, vol. 97, no. 8, p. 083102, 2005.

[121] S. Kanehira, K. Miura, and K. Hirao, "Ion exchange in glass using femtosecond laser irradiation," *Applied Physics Letters*, vol. 93, no. 2, p. 023112, 2008.

[122] T. T. Fernandez, B. Sotillo, J. del Hoyo, J.-A. Valles, R. M. Vazquez, P. Fernandez, and J. Solis, "Dual regimes of ion migration in high repetition rate femtosecond laser inscribed waveguides," *IEEE Photonics Technology Letters*, vol. 27, no. 10, p. 1068, 2015.

[123] S. Richter, M. Heinrich, S. Döring, A. Tünnermann, S. Nolte, and U. Peschel, "Nanogratings in fused silica: Formation, control, and applications," *Journal of Laser Applications*, vol. 24, no. 4, p. 042008, 2012.

[124] S. Richter, C. Miese, S. Döring, F. Zimmermann, M. J. Withford, A. Tünnermann, and S. Nolte, "Laser induced nanogratings beyond fused silica-periodic nanostructures in borosilicate glasses and ule^{TM}," *Optical Materials Express*, vol. 3, no. 8, p. 1161, 2013.

[125] C. Hnatovsky, R. Taylor, E. Simova, V. Bhardwaj, D. Rayner, and P. Corkum, "Polarization-selective etching in femtosecond laser-assisted microfluidic channel fabrication in fused silica," *Optics Letters*, vol. 30, no. 14, p. 1867, 2005.

[126] C. Corbari, A. Champion, M. Gecevičius, M. Beresna, Y. Bellouard, and P. G. Kazansky, "Femtosecond versus picosecond laser machining of nano-gratings and micro-channels in silica glass," *Optics Express*, vol. 21, no. 4, p. 3946, 2013.

[127] Y. Li, K. Itoh, W. Watanabe, K. Yamada, D. Kuroda, J. Nishii, and Y. Jiang, "Three-dimensional hole drilling of silica glass from the rear surface with femtosecond laser pulses," *Optics Letters*, vol. 26, no. 23, p. 1912, 2001.

[128] E. Glezer, M. Milosavljevic, L. Huang, R. Finlay, T.-H. Her, J. P. Callan, and E. Mazur, "Three-dimensional optical storage inside transparent materials," *Optics Letters*, vol. 21, no. 24, p. 2023, 1996.

[129] K. Itoh, W. Watanabe, S. Nolte, and C. B. Schaffer, "Ultrafast processes for bulk modification of transparent materials," *MRS Bulletin*, vol. 31, no. 8, p. 620, 2006.

[130] S. M. Eaton, H. Zhang, M. L. Ng, J. Li, W.-J. Chen, S. Ho, and P. R. Herman, "Transition from thermal diffusion to heat accumulation in high repetition rate femtosecond laser writing of buried optical waveguides," *Optics Express*, vol. 16, no. 13, p. 9443, 2008.

[131] J. E. Greivenkamp, *Field guide to geometrical optics*, vol. 1. SPIE Press Bellingham, WA, 2004.

[132] A. Marcinkevičius, V. Mizeikis, S. Juodkazis, S. Matsuo, and H. Misawa, "Effect of refractive index-mismatch on laser microfabrication in silica glass," *Applied Physics A*, vol. 76, no. 2, p. 257, 2003.

[133] P. Salter, M. Baum, I. Alexeev, M. Schmidt, and M. Booth, "Exploring the depth range for three-dimensional laser machining with aberration correction," *Optics Express*, vol. 22, no. 15, p. 17644, 2014.

[134] Y. Hayasaki, T. Sugimoto, A. Takita, and N. Nishida, "Variable holographic femtosecond laser processing by use of a spatial light modulator," *Applied Physics Letters*, vol. 87, no. 3, p. 031101, 2005.

[135] R. W. Boyd, *Nonlinear optics*. Elsevier, 2003.

[136] K. Okamoto, *Fundamentals of optical waveguides*. Academic Press, 2006.

[137] A. W. Snyder and J. Love, *Optical waveguide theory*. Springer Science & Business Media, 2012.

[138] S. Eaton, *Contrasts in Thermal Diffusion and Heat Accumulation Effects in the Fabrication of Waveguides in Glasses using Variable Repetition Rate Femtosecond Laser*. PhD thesis, University of Toronto, 2008.

[139] M. R. Vázquez, B. Sotillo, S. Rampini, V. Bharadwaj, B. Gholipour, P. Fernández, R. Ramponi, C. Soci, and S. M. Eaton, "Femtosecond laser inscription of nonlinear photonic circuits in gallium lanthanum sulphide glass," *Journal of Physics Photonics*, vol. 1, p. 015006, 2018.

[140] J. Requejo-Isidro, A. Mairaj, V. Pruneri, D. Hewak, M. Netti, and J. Baumberg, "Self refractive non-linearities in chalcogenide based glasses," *Journal of non-crystalline solids*, vol. 317, no. 3, p. 241, 2003.

[141] M. E. Thomas and W. J. Tropf, "Optical properties of diamond," *Johns Hopkins APL Technical Digest*, vol. 14, p. 16, 1993.

[142] M. Barnoski, *Fundamentals of optical fiber communications*. Elsevier, 2012.

[143] R. Trebino, *Frequency-resolved optical gating: the measurement of ultrashort laser pulses*. Springer Science & Business Media, 2012.

[144] K. Wu, J. G. De Abajo, C. Soci, P. P. Shum, and N. I. Zheludev, "An optical fiber network oracle for NP-complete problems," *Light: Science & Applications*, vol. 3, no. 2, p. e147, 2014.

[145] T. Meany, S. Gross, N. Jovanovic, A. Arriola, M. Steel, and M. J. Withford, "Towards low-loss lightwave circuits for non-classical optics at 800 and 1,550 nm," *Applied Physics A*, vol. 114, no. 1, p. 113, 2014.

[146] T. Fernandez, M. Sakakura, S. Eaton, B. Sotillo, J. Siegel, J. Solis, Y. Shimotsuma, and K. Miura, "Bespoke photonic devices using ultrafast laser driven ion migration in glasses," *Progress in Materials Science*, vol. 94, p. 68, 2018.

[147] W.-J. Chen, S. M. Eaton, H. Zhang, and P. R. Herman, "Broadband directional couplers fabricated in bulk glass with high repetition rate femtosecond laser pulses," *Optics Express*, vol. 16, no. 15, p. 11470, 2008.

[148] L. Fortnow, *The golden ticket: P, NP, and the search for the impossible*. Princeton University Press Princeton, 2013.

[149] P. E. Dunne, "An annotated list of selected NP-complete problems," *COMP202, Dept. of Computer Science, University of Liverpool*, 2008.

[150] F. Harary and I. C. Ross, "A procedure for clique detection using the group matrix," *Sociometry*, vol. 20, no. 3, p. 205, 1957.

[151] S. Dolev and H. Fitoussi, "Masking traveling beams: Optical solutions for NP-complete problems, trading space for time," *Theoretical Computer Science*, vol. 411, no. 6, p. 837, 2010.

[152] S. Aaronson, "Guest column: NP-complete problems and physical reality," *ACM Sigact News*, vol. 36, no. 1, p. 30, 2005.

[153] D. T. Chiu, E. Pezzoli, H. Wu, A. D. Stroock, and G. M. Whitesides, "Using three-dimensional microfluidic networks for solving computationally hard problems," *Proceedings of the National Academy of Sciences*, vol. 98, no. 6, p. 2961, 2001.

[154] C. Guyeux, N. M.-L. Côté, J. M. Bahi, and W. Bienia, "Is protein folding problem really a NP-complete one? first investigations," *Journal of Bioinformatics and Computational Biology*, vol. 12, no. 01, p. 1350017, 2014.

[155] K. A. Dill, S. B. Ozkan, M. S. Shell, and T. R. Weikl, "The protein folding problem," *Annual Review of Biophysics*, vol. 37, p. 289, 2008.

[156] A. M. Childs, D. Gosset, and Z. Webb, "Universal computation by multiparticle quantum walk," *Science*, vol. 339, no. 6121, p. 791, 2013.

[157] J. L. O'brien, "Optical quantum computing," *Science*, vol. 318, no. 5856, p. 1567, 2007.

[158] J. B. Spring, B. J. Metcalf, P. C. Humphreys, W. S. Kolthammer, X.-M. Jin, M. Barbieri, A. Datta, N. Thomas-Peter, N. K. Langford, D. Kundys, *et al.*, "Boson sampling on a photonic chip," *Science*, vol. 339, no. 6121, p. 798, 2013.

[159] G. D. Marshall, A. Politi, J. C. Matthews, P. Dekker, M. Ams, M. J. Withford, and J. L. O'Brien, "Laser written waveguide photonic quantum circuits," *Optics Express*, vol. 17, no. 15, p. 12546, 2009.

[160] Q. Liu, L. Wang, A. G. Frutos, A. E. Condon, R. M. Corn, and L. M. Smith, "DNA computing on surfaces," *Nature*, vol. 403, no. 6766, p. 175, 2000.

[161] K.-W. Huang, J.-L. Chen, C.-S. Yang, and C.-W. Tsai, "A memetic particle swarm optimization algorithm for solving the DNA fragment assembly problem," *Neural Computing and Applications*, vol. 26, no. 3, p. 495, 2015.

[162] T. Haist and W. Osten, "An optical solution for the traveling salesman problem," *Optics Express*, vol. 15, no. 16, p. 10473, 2007.

[163] M. Oltean, "Solving the Hamiltonian path problem with a light-based computer," *Natural Computing*, vol. 7, no. 1, p. 57, 2008.

[164] W. Hu, K. Wu, P. P. Shum, N. I. Zheludev, and C. Soci, "All-optical implementation of the ant colony optimization algorithm," *Scientific Reports*, vol. 6, p. 26283, 2016.

[165] K. Wu, C. Soci, P. P. Shum, and N. I. Zheludev, "Computing matrix inversion with optical networks," *Optics Express*, vol. 22, no. 1, p. 295, 2014.

[166] B. Gholipour, P. Bastock, C. Craig, K. Khan, D. Hewak, and C. Soci, "Amorphous metal-sulphide microfibers enable photonic synapses for brain-like computing," *Advanced Optical Materials*, vol. 3, no. 5, p. 635, 2015.

[167] P. Frisco, C. Henkel, and S. Tengely, "An algorithm for SAT without an extraction phase," in *International Workshop on DNA-Based Computers*, p. 67, Springer, 2005.

[168] R. Boyd, J. Heebner, N. Lepeshkin, Q.-H. Park, A. Schweinsberg, G. Wicks, A. Baca, J. Fajardo, R. Hancock, M. Lewis, *et al.*, "Nanofabrication of optical structures and devices for photonics and biophotonics," *Journal of Modern Optics*, vol. 50, no. 15-17, p. 2543, 2003.

[169] B. Jalali and S. Fathpour, "Silicon photonics," *Journal of Lightwave Technology*, vol. 24, no. 12, p. 4600, 2006.

[170] A. N. Tait, T. F. Lima, E. Zhou, A. X. Wu, M. A. Nahmias, B. J. Shastri, and P. R. Prucnal, "Neuromorphic photonic networks using silicon photonic weight banks," *Scientific Reports*, vol. 7, no. 1, p. 7430, 2017.

[171] A. E. Willner, S. Khaleghi, M. R. Chitgarha, and O. F. Yilmaz, "All-optical signal processing," *Journal of Lightwave Technology*, vol. 32, no. 4, p. 660, 2014.

[172] A. Himeno, K. Kato, and T. Miya, "Silica-based planar lightwave circuits," *IEEE Journal of Selected Topics in Quantum Electronics*, vol. 4, no. 6, p. 913, 1998.

[173] M. A. Nahmias, B. J. Shastri, A. N. Tait, T. F. de Lima, and P. R. Prucnal, "Neuromorphic photonics," *Optics and Photonics News*, vol. 29, no. 1, p. 34, 2018.

[174] A. Arriola, S. Mukherjee, D. Choudhury, L. Labadie, and R. R. Thomson, "Ultrafast laser inscription of mid-IR directional couplers for stellar interferometry," *Optics Letters*, vol. 39, no. 16, p. 4820, 2014.

[175] T. Gretzinger, S. Gross, M. Ams, A. Arriola, and M. J. Withford, "Ultrafast laser inscription in chalcogenide glass: thermal versus athermal fabrication," *Optical Materials Express*, vol. 5, no. 12, p. 2862, 2015.

[176] Z. Chai, X. Hu, F. Wang, X. Niu, J. Xie, and Q. Gong, "Ultrafast all-optical switching," *Advanced Optical Materials*, vol. 5, no. 7, p. 1600665, 2017.

[177] M. Förtsch, J. U. Fürst, C. Wittmann, D. Strekalov, A. Aiello, M. V. Chekhova, C. Silberhorn, G. Leuchs, and C. Marquardt, "A versatile source of single photons for quantum information processing," *Nature Communications*, vol. 4, p. 1818, 2013.

[178] S. M. Eaton, W. Chen, L. Zhang, H. Zhang, R. Iyer, J. Aitchison, and P. Herman, "Telecom-band directional coupler written with femtosecond fiber laser," *IEEE Photonics Technology Letters*, vol. 18, no. 20, p. 2174, 2006.

[179] G. Demetriou *et al.*, *Ultrafast nonlinear optics of bulk and two-dimensional materials for infrared applications*. PhD thesis, Heriot-Watt University, 2016.

[180] I. Batarseh and A. Harb, "Review of switching concepts and power semiconductor devices," in *Power Electronics*, p. 25, Springer, 2018.

[181] A. Zakery and S. R. Elliott, *Optical nonlinearities in chalcogenide glasses and their applications*, vol. 135. Springer, 2007.

[182] K. Tanaka, "Optical nonlinearity in photonic glasses," in *Springer Handbook of Electronic and Photonic Materials*, p. 1, Springer, 2017.

[183] G. Stegeman, E. Wright, N. Finlayson, R. Zanoni, and C. Seaton, "Third order nonlinear integrated optics," *Journal of Lightwave Technology*, vol. 6, no. 6, p. 953, 1988.

[184] V. Mizrahi, K. DeLong, G. I. Stegeman, M. A. Saifi, and M. Andrejco, "Two-photon absorption as a limitation to all-optical switching," *Optics Letters*, vol. 14, no. 20, p. 1140, 1989.

[185] N. Korkmaz, İ. Öztürk, and R. Kiliç, "Modeling, simulation, and implementation issues of CPGs for neuromorphic engineering applications," *Computer Applications in Engineering Education*, vol. 26, no. 4, p. 782, 2018.

[186] G. Indiveri and S.-C. Liu, "Memory and information processing in neuromorphic systems," *Proceedings of the IEEE*, vol. 103, no. 8, p. 1379, 2015.

[187] J. E. Laird, C. Lebiere, and P. S. Rosenbloom, "A standard model of the mind: Toward a common computational framework across artificial intelligence, cognitive science, neuroscience, and robotics.," *AI Magazine*, vol. 38, no. 4, 2017.

[188] J. De Fauw, J. R. Ledsam, B. Romera-Paredes, S. Nikolov, N. Tomasev, S. Blackwell, H. Askham, X. Glorot, B. O'Donoghue, D. Visentin, *et al.*, "Clinically applicable deep learning for diagnosis and referral in retinal disease," *Nature Medicine*, vol. 24, no. 9, p. 1342, 2018.

[189] I.-H. Chung, T. N. Sainath, B. Ramabhadran, M. Picheny, J. Gunnels, V. Austel, U. Chauhari, and B. Kingsbury, "Parallel deep neural network training for big data on blue gene/q," *IEEE Transactions on Parallel and Distributed Systems*, vol. 28, no. 6, p. 1703, 2017.

[190] S. K. Esser, A. Andreopoulos, R. Appuswamy, P. Datta, D. Barch, A. Amir, J. Arthur, A. Cassidy, M. Flickner, P. Merolla, *et al.*, "Cognitive computing systems: Algorithms and applications for networks of neurosynaptic cores," in *Neural Networks (IJCNN), The 2013 International Joint Conference on*, p. 1, IEEE, 2013.

[191] C.-S. Poon and K. Zhou, "Neuromorphic silicon neurons and large-scale neural networks: challenges and opportunities," *Frontiers in Neuroscience*, vol. 5, p. 108, 2011.

[192] G. Indiveri, B. Linares-Barranco, R. Legenstein, G. Deligeorgis, and T. Prodromakis, "Integration of nanoscale memristor synapses in neuromorphic computing architectures," *Nanotechnology*, vol. 24, no. 38, p. 384010, 2013.

[193] N. K. Upadhyay, S. Joshi, and J. J. Yang, "Synaptic electronics and neuromorphic computing," *Science China Information Sciences*, vol. 59, no. 6, p. 061404, 2016.

[194] J. J. Yang and Q. Xia, "Organic electronics: battery-like artificial synapses," *Nature Materials*, vol. 16, no. 4, p. 396, 2017.

[195] D. AOCNP, "Watson will see you now: a supercomputer to help clinicians make informed treatment decisions," *Clinical Journal of Oncology Nursing*, vol. 19, no. 1, p. 31, 2015.

[196] J. L. Malin, "Envisioning Watson as a rapid-learning system for oncology," *Journal of Oncology Practice*, vol. 9, no. 3, p. 155, 2013.

[197] S. Ambrogio, P. Narayanan, H. Tsai, R. M. Shelby, I. Boybat, C. Nolfo, S. Sidler, M. Giordano, M. Bodini, N. C. Farinha, *et al.*, "Equivalent-accuracy accelerated neural-network training using analogue memory," *Nature*, vol. 558, no. 7708, p. 60, 2018.

[198] J. E. Kelly III and S. Hamm, *Smart machines: IBM's Watson and the era of cognitive computing*. Columbia University Press, 2013.

[199] Y. Shen, N. C. Harris, S. Skirlo, M. Prabhu, T. Baehr-Jones, M. Hochberg, X. Sun, S. Zhao, H. Larochelle, D. Englund, *et al.*, "Deep learning with coherent nanophotonic circuits," *Nature Photonics*, vol. 11, no. 7, p. 441, 2017.

[200] W. H. Pernice and H. Bhaskaran, "Photonic non-volatile memories using phase change materials," *Applied Physics Letters*, vol. 101, no. 17, p. 171101, 2012.

[201] Y. Shi, X. Liang, B. Yuan, V. Chen, H. Li, F. Hui, Z. Yu, F. Yuan, E. Pop, H.-S. P. Wong, *et al.*, "Electronic synapses made of layered two-dimensional materials," *Nature Electronics*, vol. 1, no. 8, p. 458, 2018.

[202] Y. Zhao and J. Jiang, "Recent progress on neuromorphic synapse electronics: From emerging materials, devices, to neural networks," *Journal of Nanoscience and Nanotechnology*, vol. 18, no. 12, p. 8003, 2018.

[203] C. Chen, K. Kim, Q. Truong, A. Shen, Z. Li, and Y. Chen, "A spiking neuron circuit based on a carbon nanotube transistor," *Nanotechnology*, vol. 23, no. 27, p. 275202, 2012.

[204] D. Kuzum, S. Yu, and H. P. Wong, "Synaptic electronics: materials, devices and applications," *Nanotechnology*, vol. 24, no. 38, p. 382001, 2013.

[205] A. N. Tait, M. A. Nahmias, Y. Tian, B. J. Shastri, and P. R. Prucnal, "Photonic neuromorphic signal processing and computing," in *Nanophotonic Information Physics*, p. 183, Springer, 2014.

[206] D. O. Hebb *et al.*, "The organization of behavior," 1949.

[207] W. Gerstner, A. K. Kreiter, H. Markram, and A. V. Herz, "Neural codes: firing rates and beyond," *Proceedings of the National Academy of Sciences*, vol. 94, no. 24, p. 12740, 1997.

[208] L. Childress, M. G. Dutt, J. Taylor, A. Zibrov, F. Jelezko, J. Wrachtrup, P. Hemmer, and M. Lukin, "Coherent dynamics of coupled electron and nuclear spin qubits in diamond," *Science*, vol. 314, no. 5797, p. 281, 2006.

[209] H. Mamin, M. Kim, M. Sherwood, C. Rettner, K. Ohno, D. Awschalom, and D. Rugar, "Nanoscale nuclear magnetic resonance with a nitrogen-vacancy spin sensor," *Science*, vol. 339, no. 6119, p. 557, 2013.

[210] F. Jelezko, T. Gaebel, I. Popa, A. Gruber, and J. Wrachtrup, "Observation of coherent oscillations in a single electron spin," *Physical Review Letters*, vol. 92, no. 7, p. 076401, 2004.

[211] E. Bernardi, R. Nelz, S. Sonusen, and E. Neu, "Nanoscale sensing using point defects in single-crystal diamond: recent progress on nitrogen vacancy center-based sensors," *Crystals*, vol. 7, no. 5, p. 124, 2017.

[212] P. Olivero, S. Rubanov, P. Reichart, B. C. Gibson, S. T. Huntington, J. Rabeau, A. D. Greentree, J. Salzman, D. Moore, D. N. Jamieson, *et al.*, "Ion-beam-assisted lift-off technique for three-dimensional micromachining of freestanding single-crystal diamond," *Advanced Materials*, vol. 17, no. 20, p. 2427, 2005.

[213] A. Faraon, C. Santori, Z. Huang, V. M. Acosta, and R. G. Beausoleil, "Coupling of nitrogen-vacancy centers to photonic crystal cavities in monocrystalline diamond," *Physical Review Letters*, vol. 109, no. 3, p. 033604, 2012.

[214] P. E. Barclay, K.-M. C. Fu, C. Santori, A. Faraon, and R. G. Beausoleil, "Hybrid nanocavity resonant enhancement of color center emission in diamond," *Physical Review X*, vol. 1, no. 1, p. 011007, 2011.

[215] K.-M. Fu, C. Santori, P. Barclay, I. Aharonovich, S. Prawer, N. Meyer, A. Holm, and R. Beausoleil, "Coupling of nitrogen-vacancy centers in diamond to a GaP waveguide," *Applied Physics Letters*, vol. 93, no. 23, p. 234107, 2008.

[216] B. J. Shields, Q. Unterreithmeier, N. De Leon, H. Park, and M. D. Lukin, "Efficient readout of a single spin state in diamond via spin-to-charge conversion," *Physical Review Letters*, vol. 114, no. 13, p. 136402, 2015.

[217] S. A. Momenzadeh, R. J. Stohr, F. F. de Oliveira, A. Brunner, A. Denisenko, S. Yang, F. Reinhard, and J. Wrachtrup, "Nanoengineered diamond waveguide as a robust bright platform for nanomagnetometry using shallow nitrogen vacancy centers," *Nano Letters*, vol. 15, no. 1, p. 165, 2014.

[218] M. J. Burek, N. P. de Leon, B. J. Shields, B. J. Hausmann, Y. Chu, Q. Quan, A. S. Zibrov, H. Park, M. D. Lukin, and M. Lončar, "Free-standing mechanical and photonic nanostructures in single-crystal diamond," *Nano Letters*, vol. 12, no. 12, p. 6084, 2012.

[219] S. Lagomarsino, P. Olivero, F. Bosia, M. Vannoni, S. Calusi, L. Giuntini, and M. Massi, "Evidence of light guiding in ion-implanted diamond," *Physical Review Letters*, vol. 105, no. 23, p. 233903, 2010.

[220] M. Neff, T. V. Kononenko, S. M. Pimenov, V. Romano, W. Lüthy, and V. Konov, "Femtosecond laser writing of buried graphitic structures in bulk diamond," *Applied Physics A*, vol. 97, no. 3, p. 543, 2009.

[221] A. Courvoisier, M. J. Booth, and P. S. Salter, "Inscription of 3D waveguides in diamond using an ultrafast laser," *Applied Physics Letters*, vol. 109, no. 3, p. 031109, 2016.

[222] J. Orwa, K. Nugent, D. Jamieson, and S. Prawer, "Raman investigation of damage caused by deep ion implantation in diamond," *Physical Review B*, vol. 62, no. 9, p. 5461, 2000.

[223] Y.-C. Chen, P. S. Salter, S. Knauer, L. Weng, A. C. Frangeskou, C. J. Stephen, S. N. Ishmael, P. R. Dolan, S. Johnson, B. L. Green, *et al.*, "Laser writing of coherent colour centres in diamond," *Nature Photonics*, vol. 11, no. 2, p. 77, 2017.

[224] Y.-C. Chen, B. Griffiths, L. Weng, S. Nicley, S. N. Ishmael, Y. Lekhai, S. Johnson, C. J. Stephen, B. L. Green, G. W. Morley, *et al.*, "Laser writing of individual atomic defects in a crystal with near-unity yield," *arXiv preprint arXiv:1807.04028*, 2018.

[225] J. Taylor, P. Cappellaro, L. Childress, L. Jiang, D. Budker, P. Hemmer, A. Yacoby, R. Walsworth, and M. Lukin, "High-sensitivity diamond magnetometer with nanoscale resolution," *Nature Physics*, vol. 4, no. 10, p. 810, 2008.

[226] J. Barry, "Jf barry, mj turner, jm schloss, dr glenn, y. song, md lukin, h. park, and rl walsworth, proc. natl. acad. sci.(usa) 113, 14133 (2016).," *Proc. Natl. Acad. Sci.(USA)*, vol. 113, p. 14133, 2016.

[227] E. H. Chen, H. A. Clevenson, K. A. Johnson, L. M. Pham, D. R. Englund, P. R. Hemmer, and D. A. Braje, "High-sensitivity spin-based electrometry with an ensemble of nitrogen-vacancy centers in diamond," *Physical Review A*, vol. 95, no. 5, p. 053417, 2017.

[228] H. Clevenson, M. E. Trusheim, C. Teale, T. Schröder, D. Braje, and D. Englund, "Broadband magnetometry and temperature sensing with a light-trapping diamond waveguide," *Nature Physics*, vol. 11, no. 5, p. 393, 2015.

[229] J. Burghoff, S. Nolte, and A. Tünnermann, "Origins of waveguiding in femtosecond laser-structured $LiNbO_3$," *Applied Physics A*, vol. 89, no. 1, p. 127, 2007.

[230] B. Sotillo, A. Chiappini, V. Bharadwaj, J. Hadden, F. Bosia, P. Olivero, M. Ferrari, R. Ramponi, P. Barclay, and S. Eaton, "Polarized micro-Raman studies of femtosecond laser written stress-induced optical waveguides in diamond," *Applied Physics Letters*, vol. 112, no. 3, p. 031109, 2018.